Universitat Autònoma de Barcelona

Search for very-high-energy emission from pulsars and tests of Lorentz invariance using the MAGIC telescopes

SIDIKA MERVE COLAK

Search for very-high-energy emission from pulsars and tests of Lorentz invariance using the MAGIC telescopes

AUTHOR:
SIDIKA MERVE COLAK
INSTITUT DE FÍSICA D'ALTES ENERGIES (IFAE)

Director:
Manel MARTINEZ

Director:
Abelardo MORALEJO

TUTOR:
ENRIQUE FERNANDEZ

A thesis submitted in fulfillment of the requirements
for the degree of Doctor of Philosophy

in the

Department de Física
Universitat Autònoma de Barcelona

Declaration of Authorship

I herewith declare that I have produced this thesis without the prohibited assistance of third parties and without making use of aids other than those specified; notions taken over directly or indirectly from other sources have been identified as such. This paper has not previously been presented in identical or similar form to any other Spanish or foreign examination board.

The thesis work was conducted from May 2016 to September 2021 under the supervision of Manel Martinez and Abelardo Moralejo at Barcelona.

""There is no use trying," said Alice; "one can't believe impossible things."

"I dare say you haven't had much practice," said the Queen. "When I was your age, I always did it for half an hour a day. Why, sometimes I've believed as many as six impossible things before breakfast." "

Lewis Carroll, Alice in Wonderland

"My eureka moment was in the dead of night, the early hours of the morning, on a cold, cold night, and my feet were so cold, they were aching. But when the result poured out of the charts, you just forget all that. You realize instantly how significant this is—what it is you've really landed on—and it's great! "

Jocelyn Bell-Burnell, on the discovery of the first pulsar

Acknowledgements

Firstly, I would like to thank my supervisors. Manel Martinez, not only for helping, encouraging, and teaching me so many things in the field but also for supporting any bureaucratic obstacles that I faced during my Ph.D. period. Abelardo Moralejo, for the detailed checks of the manuscript, discussions, and corrections, as well as the expert support for the high-level analysis.

Besides my supervisors, I would like to thank my thesis committee: Julien Bolmont, Emma Oña Wilhelmi, Javier Rico, Jose Manuel Carmona, Monica Vazquez, and Lluis Font, for accepting to be a part of my committee and for their constructive comments, suggestions, and corrections, as well as their hard questions, which has widened my perspective on the field.

A special thanks to Oscar Blanch for the guidance since the beginning of my Ph.D. period and support for various topics in this thesis. I would like to sincerely thank IFAE/MAGIC Group to the Ph.D. students and Postdocs that helped me learn the basics of the MAGIC Analysis (especially to Quim Palacio for his patience with my endless questions). Additionally, I would like to thank the current director of IFAE, Ramon Miquel, for being helpful whenever I faced a bureaucratic obstacle.

I would like to thank Markus Gaug for his kind helps (even during his holiday periods) on the LIDAR and Crab Pulsar LIV analysis and for letting me run his codes for this thesis. A special thanks go to Dijana Dominis for inviting me to Rijeka University for working with the gamma-ray group. To Tomislav Terzic and Marina Manganaro for their contributions to LIV Analysis and 3C66A analysis.

The MAGIC Collaboration is acknowledged for allowing the use of proprietary observational data. The Crab Pulsar LIV analysis and the 3C66A MAGIC results presented in this thesis have not undergone the internal review procedure of MAGIC publications yet. A huge thanks to the MAGIC Collaboration members for teaching me so many things and having fun during the meetings and observations. Thanks to the Barcelona Raman LIDAR group that I had the chance to work for CTA.

I am pleased to thank the Spanish Ministry of Economy, Industry, and Competitiveness (MINECO) for the scholarship support with Severo Ochoa. And to the Scientific and Technological Research Council of Turkey (TUBITAK) for the National Graduate and the Undergraduate Scholarships, which supported my early academic career.

Last but not least, I would like to thank my father for showing his support and caring even though living far from each other. Thanks to my friends and family for their support, which helped me finish this thesis and survive mentally while being exposed to the pandemic crisis.

Contents

Declaration of Authorship iii

Acknowledgements vii

Summary 1

Resumen 1

Resumen 3

Introduction 3

1 Introduction to Pulsars 5
- 1.1 Origin of Neutron Stars . . . 5
- 1.2 Discovery of Pulsars . . . 7
- 1.3 General Properties of Neutron Stars . . . 8
- 1.4 Pulsar Systems . . . 11
- 1.5 VHE Emission Mechanisms of Pulsars . . . 16

2 Lorentz Invariance Violation with Pulsars 21
- 2.1 Fundamental Physics Studies with Pulsars . . . 21
- 2.2 Lorentz Invariance Violation . . . 23
  - 2.2.1 Time of Flight Studies . . . 24

3 Introduction to IACTs and the MAGIC Telescopes 29
- 3.1 Gamma-ray Astronomy . . . 29
- 3.2 Astrophysical Gamma-ray Detection Techniques . . . 30
  - 3.2.1 Satellites . . . 30
  - 3.2.2 Ground-based systems . . . 31
- 3.3 Imaging Atmospheric Cherenkov Telescopes . . . 32
- 3.4 The MAGIC Telescopes . . . 34
  - 3.4.1 Technical Description . . . 35
  - 3.4.2 MAGIC Data Analysis Chain . . . 40
    - Low-level Process . . . 40
    - Medium-level Process . . . 41
    - High-level Process . . . 45
- 3.5 The Future of IACTs: the Cherenkov Telescope Array . . . 47

4 LIDAR Systems for IACTs 49
- 4.1 Atmospheric effects . . . 49
- 4.2 LIDAR Technique . . . 51
- 4.3 The MAGIC LIDAR . . . 52
- 4.4 The Barcelona Raman LIDAR . . . 54
  - 4.4.1 Polychromator Light Leakage Tests . . . 55

4.4.2 First commissioning results 63

5 PSR J0218+4232 Observations with the MAGIC Telescopes 65
5.1 The Target Selection 65
5.2 The Millisecond Pulsar PSRJ0218+4232 67
5.3 MAGIC Observations 2018-2019 67
5.4 Data Selection 68
5.5 Data Reduction 69
5.6 The Crab Nebula Sanity Check 70
5.7 Background Subtraction 71
5.8 Results 74
5.9 The Blazar 3C66A 78
5.9.1 Data Selection 79
5.9.2 Data Reduction 80
Off-Axis Analysis 80
5.9.3 Results 81

6 The Crab Pulsar with the MAGIC Telescopes 85
6.1 The Crab Pulsar studies with the MAGIC Telescopes 85
6.2 The Magic Observations in Stereoscopic Mode 87
6.2.1 2009-2014 87
Correction of the Energy Miscalibration 87
6.2.2 2014-2019 88
6.3 Data Selection for 2014-2019 data 89
6.4 Data Reduction for the 2014-2019 data 89
6.5 The Crab Nebula Sanity Checks 89
6.6 Cut Optimization 91
6.7 Results 92

7 Lorentz Invariance Violation Limits with the Crab Pulsar 95
7.1 What to Expect From Pulsars for the LIV studies 95
7.2 Previous Limits on LIV with Crab Pulsar with the MAGIC Telescopes . 98
7.2.1 The Peak Comparison Method 98
7.2.2 Maximum Likelihood Method 100
7.3 Limits on LIV with 2009-2019 Crab Pulsar MAGIC Observations 106

8 Conclusions 111

Bibliography 113

List of Figures

1.1 The Orion Nebula (Credit:NASA and STScI) 5
1.2 The Hertzsprung–Russell (H-R) diagram for stellar evolution (Credit Chandra X-ray Observatory) 6
1.3 The lifespan of the stars. 7
1.4 Jocelyn Bell and discovery of the first pulsar (Credit Cavendish Laboratory) 8
1.5 Gamma-ray pulsars detected by Fermi-LAT (Credit: Fermi-LAT/GSFC) 8
1.6 Schematic structure of a neutron star (A. Watts et al., 2015) 9
1.7 Neutron Star magnetosphere (Goldreich and Julian, 1969) 10
1.8 Sketch of current-sheet model (Cerutti and Beloborodov, 2017) 11
1.9 Diagram of neutron star populations (Alice K. Harding, 2013) 12
1.10 Binary pulsar evolution (Lorimer, 2005) 13
1.11 Schematic of the star disk interaction (Matt and Pudritz, 2005) 14
1.12 Recycled evolution scenario of PSR B1913+16 (Srinivasan, 2010) 14
1.13 Evolution scenario of pulsars (adapted from (Ziólkowski, 1997)) 15
1.14 Possible gamma-ray emission mechanisms for the pulsars (Oya, 2010) 16
1.15 Locations of the VHE pulsar emission models (Alice K. Harding, 2021) 18
1.16 A sketch of Pulsar Wind Nebula and the non-thermal nebula interaction (Aharonian, Bogovalov, and Khangulyan, 2012a) 20
1.17 Illistrations of gamma-ray emissions from pulsar systems (Mirabel, 2012) 20

2.1 Pulsar map fragment of Golden Record (Credit: NASA/JPL) 21
2.2 Neutron Star mass-radius relations (A. L. Watts, 2019) 22
2.3 Gravitational bending effect observation in PSR J0030 +0451 (Credit: NASA) 22
2.4 Gravitational Wave and Light detection from GW170817 (Credit:LIGO, Georgia Tech) 23
2.5 Astrophysical Tests for MDR 24
2.6 Recent Contraints on LIV for linear case (Martıénez-Huerta, Lang, and de Souza, 2020) 25
2.7 Recent Contraints on LIV for quadratic case (Martıénez-Huerta, Lang, and de Souza, 2020) 26
2.8 Illustration of time delay due to MDR 26
2.9 An example of Pulsar phase folding (Deshpande and Rankin, 1999) . . 27

3.1 The electromagnetic spectrum and the detection techniques (Longair, 1992) 30
3.2 The sketch of the Fermi-LAT detector (Credit: Fermi-LAT) 31
3.3 Extensive Air Showers in the atmosphere 32
3.4 Sketch of IACTs, (Credit Ruben Lopez(2015)). 33
3.5 Monte Carlo Simulations for electromagnetic and hadronic shower (Credit: Johannes Knapp) 33

3.6 Site of the MAGIC Telescopes 34
3.7 The sensitivity of the MAGIC Telescopes (Aleksić et al., 2016) 35
3.8 Cameras of the MAGIC Telescopes and the trigger areas (adapted from (Aleksic, 2015) (Dazzi et al., 2021) (Gaug, 2006)) 37
3.9 The working principle of the IACTs (Dazzi et al., 2021) 38
3.10 The context of the stereoscopic trigger systems of the MAGIC telescopes (Dazzi et al., 2021) 39
3.11 Simulated signal produced by a 31.8 GeV gamma-ray shower in one of the MAGIC cameras (Dazzi et al., 2015) 39
3.12 Recorded events and the images after the cleaning by MARS (Aleksic, 2015) 41
3.13 Illustration of the Hillas parametrization (Aleksic, 2015) 42
3.14 MAGIC Analysis Chain (adapted from (Zanin et al., 2013)) 44
3.15 An example of *Theta*^{2} histogram created with the program, Odie . . . 45
3.16 An example of an SED of Crab Nebula created with the program Flute 46
3.17 An example of skymap created with the program Caspar 47
3.18 Artistic rendering of CTA observatory (Credit: Gabriel Pérez Diaz, IAC / Marc-André Besel, CTAO) 48
3.19 CTAO-N and CTAO-S sensitivity compared to the other instruments (Credit:CTA-Observatory) 48

4.1 Typically observed spectrum of Cherenkov light (Doering et al., 2001) . 50
4.2 Direct transmission of light from space (here 100 km) altitude along a vertical path to an altitude of 2.2 km, as calculated with MODTRAN. The impact of the most important absorbers and scatterers is shown. Adapted from (Bernlöhr, 2000) 50
4.3 Energy diagram of Rayleigh, Stokes Raman and Anti-Stokes Raman scatterings (Wróbel, 2016) 51
4.4 Overview of lidar backscatter signals for a laser wavelength of 532 nm (Behrendt et al., 2002) 53
4.5 The MAGIC LIDAR (Fruck et al., 2014) 53
4.6 Illustration explaining the data analysis algorithm (Fruck et al., 2014) . 54
4.7 The Barcelona Raman LIDAR (Gaug et al., 2019) 54
4.8 Schema of the Barcelona Raman LIDAR 55
4.9 The Polychromator of the Barcelona Raman LIDAR (Gaug et al., 2019) 57
4.10 The return power of the Barcelona Raman LIDAR was estimated by link-budget simulation (Eizmendi Valles, 2011) 58
4.11 Illustration of the setup used for the light leakage tests of the polychromator (Gaug et al., 2019) 59
4.12 Photos of the setup used for the light leakage tests of the polychromator 59
4.13 Spectrum of the Xenon Lamp used for the light leakage tests Credit: Oriol Calpe 60
4.14 Scan for each output of the polychromator 61
4.15 Light leakage tests for the 387 nm and 607 nm Raman channels of polychromator. 62
4.16 First commissioning Results (Ballester et al., 2019) 63
4.17 First commissioning Results2 (Ballester et al., 2019) 64

5.1 Magnetic field strength at the light cylinder radius vs. characteristic age of the millisecond pulsar candidates 67

5.2 Pulse profiles of PSR J0218+4232 in radio, X-rays, and gamma-rays studied in (Kuiper et al., 2000) . . . 68
5.3 Pulsed emission search from J0218 by MAGIC-I telescope (Anderhub et al., 2010) . . . 69
5.4 The minimum energy threshold estimation for J0218 analysis . . . 70
5.5 Sanity check of J0218 analysis with the Crab Nebula . . . 71
5.6 Fermi-LAT phaseogram created using 11.5 years of data (Acciari et al., 2021) . . . 72
5.7 MAGIC camera FoV configuration for the J0218 and 3C66a/B observations . . . 73
5.8 *Theta*^{2} distribution of the events from the PSR J0218+4232 . . . 73
5.9 Search for VHE pulsations of PSRJ0218+4232 by using MAGIC analysis 74
5.10 VHE pulsations searched for smaller energy binning samples using the PSR J0218+4232 analysis . . . 75
5.11 Spectral energy distribution of PSRJ0218+4232 . . . 76
5.12 MAGIC relative flux map of the region around PSR J0218+4232 . . . 77
5.13 Angular distribution of the events for PSR J0218+4232 without any phase cut . . . 77
5.14 Schematic representation of the AGN types (Beckmann and Shrader, 2012) . . . 78
5.15 Skymaps of PSR J0218+4232 and 3C66A ((Kuiper et al., 2000) (Abdo et al., 2011)) . . . 79
5.16 Broadband spectral energy distribution of 3C 66A during the 2008 October multi-wavelength campaign (Abdo et al., 2011) . . . 79
5.17 The configuration of PSRJ0218+4232 (purple star) observations by MAGIC in Wobble mode. . . . 80
5.18 Sanity check of 3C66a/B analysis with the Crab Nebula . . . 81
5.19 Angular distribution of the events for 3C66A for the flare phase. . . . 82
5.20 The skymap of the 3C66A region for flare (upper plot) and non-flare (lowe plot) period. . . . 83
5.21 Forward folded and redshift corrected SED results of 3C66A . . . 84

6.1 The Crab Pulsar phaseograms between 100-400 GeV and above 400 GeV (Ansoldi et al., 2016) . . . 86
6.2 Phase-folded spectra of the Crab Pulsar (Ansoldi et al., 2016) . . . 87
6.3 The energy reconstruction algorithm bug fix for 2014-2019 data sample for the Crab Pulsar . . . 88
6.4 The Crab Nebula spectrum of each low-zenith subsamples . . . 90
6.5 The Crab Nebula spectrum of each medium-zenith subsamples . . . 91
6.6 The Crab Nebula spectrum of each high-zenith subsamples . . . 91
6.7 The spectra of the Crab Nebula and the Crab Pulsar P1 and P2 . . . 93
6.8 The Crab Pulsar phaseogram of data collected 2009-2019 by the MAGIC Telescopes . . . 94

7.1 Crab Pulsar P2-like pulse shape and energy spectrum simulation . . . 96
7.2 The deformation on the pulse shape by the LIV linear case at energy scale, $E_{QG_1} = 2.4 \times 10^{17}$ . . . 97
7.3 The deformation on the pulse shape by the LIV quadratic case at energy scale, $E_{QG_2} = 6.1 \times 10^{10}$ . . . 97
7.4 P-$\dot{P}$ diagram of pulsars extracted from the ATNF catalog ((Manchester et al., 2005) . . . 98

7.5 Peak Comparison method for the Crab Pulsar (M. L. Ahnen et al., 2017) 100
7.6 Crab Pulsar peak positions and peak widths reported in (Aleksić et al., 2012) . . . 102
7.7 Test Statistics for the linear and quadratic cases (M. L. Ahnen et al., 2017) . . . 104
7.8 Phaseogram of the Crab Pulsar used for LIV analysis . . . 107
7.9 Effective Area of this study . . . 107
7.10 Background spectral distribution . . . 108
7.11 Test statistics results for the linear case in this work . . . 108
7.12 Test statistics results for the quadratic case in this work . . . 109

List of Tables

3.1 Table of Gamma-ray energy ranges 29
3.2 Table of upgrade periods of the stereoscopic MAGIC system 34
3.3 Observation Periods of the MAGIC Telescopes 43

4.1 The Barcelona Raman LIDAR parameters 56
4.2 Light Leakage Results in Raman Channels 60

5.1 List of MSP sources visible at the MAGIC site 66
5.2 Data used as background sample for training Random Forest for J0218 Analysis 69
5.3 MAGIC Pulsed emission Signal Test Results 75
5.4 SED Upper Limits of PSR J0218+4232 76
5.5 Table of Forward folded SED points of 3C66A 83
5.6 Table of spectral fit results of 3C66A analysis 84

6.1 The Table of the Crab Pulsar Data Analysed in this work 89
6.2 The data used as background sample for training Random Forest for the Crab Pulsar Analysis 90
6.3 Results of the spectral fit parameters for the power-law function 93
6.4 Forward folded spectral flux results of the Crab Pulsar 94
6.5 Table of excess events from the Crab Pulsar P2 and P1 94

7.1 Table of the averaged values of age, spin period, and distance of the pulsars 97
7.2 Table of obtained fit values from the Peak Comparison Method (M. L. Ahnen et al., 2017) 99
7.3 Obtained 95%CL limits from the Peak Comparison Method (M. L. Ahnen et al., 2017) 100
7.4 Summary of the used Crab Pulsar Data Samples (M. L. Ahnen et al., 2017) 103
7.5 Nuisance Parameters obtained in (M. L. Ahnen et al., 2017) 105
7.6 Summary of the Systematic Uncertainties studied in (M. L. Ahnen et al., 2017) 105
7.7 95% CL limits from the Profile Likelihood Method (M. L. Ahnen et al., 2017) 105
7.8 Summary of the Crab Pulsar Data Samples Used in this work 106
7.9 Nuisance Parameters obtained in this study 109
7.10 Table of recent LIV limits obtained with MLM for time delay studies compared to this study 110

Dedicated to the memory of my
mother
Serpil Çolak

Summary

Since their discovery, pulsars have been an essential laboratory in many different astrophysics and physics branches because they are ultra-dense, fast spinning, and multiwavelength emitting objects. They have widened our understanding of stellar evolution and compact object studies, as well as fundamental physics topics such as General Relativity and the Standard Model.

The emission mechanisms of pulsars are still not fully known. Although the history of pulsar studies in radio bands starts back in the 1960s, very high-energy (VHE) gamma-ray studies of pulsars are relatively newer. Therefore detecting new pulsars and increasing our knowledge on the discovered ones plays a crucial role in pulsar astrophysics. Cherenkov telescopes are excellent systems for studying very high-energy photons coming from the pulsars.

Due to the fact that pulsars are faint sources compared to the other gamma-ray sources such as active galactic nuclei or gamma-ray bursts, data quality is of great importance for the data analysis results, and one of the most considerable effects comes from the atmospheric conditions. Therefore atmospheric scan systems such as Raman LIDARs working with the Cherenkov telescopes are supportive systems for the data analysis.

The primary focus of this study is pulsar studies with the MAGIC telescopes and using the data for Lorentz Invariance Violation (LIV) tests. For this purpose, ten years of Crab Pulsar data has been analyzed and used for the LIV test. Moreover, a VHE emission search of a millisecond pulsar, PSR J0218+4232, has been performed for the first time in the stereoscopic mode of MAGIC telescopes. An intermediate BL Lac source, 3C66A, in the field of view (FoV) of the millisecond pulsar has been analyzed and included in this study. Apart from the astrophysical source analysis, some CTA pathfinder Raman LIDAR tests results and commissioning tests were included in this study, too.

The thesis follows this outline:

Chapter 1 is an introduction to Pulsars. The formation, evolution, and emission mechanisms are explained. Chapter 2 gives an overview of Lorentz Invariance Violation studies with pulsars. Chapter 3 describes the IACT technique, MAGIC Telescopes, and the data analysis. Chapter 4 gives an overview of LIDAR systems used for atmospheric characterization working with Cherenkov Telescopes and includes some tests results of the Barcelona Raman LIDAR, Cherenkov Telescope Array's path. Chapter 5 focuses on searching VHE emission from the millisecond pulsar PSR J0218+4232 and analysis of IBL Lac source 3C66A in the FoV. Chapter 6 focuses on 2009-2020 Crab Pulsar data analysis and the study on the highest emission up to TeV energies. Chapter 7 shows the results of the LIV test performed with the data shown in the previous chapter. Finally, the conclusion remarks, and future aspects will be discussed.

Resumen

Desde su descubrimiento, los púlsares han sido un laboratorio esencial en muchas ramas diferentes de la astrofísica y la física porque son objetos ultra densos, de giro rápido y emisores de múltiples longitudes de onda. Han ampliado nuestra comprensión de la evolución estelar y los estudios de objetos compactos, así como temas de física fundamental como la relatividad general y el modelo estándar.

Los mecanismos de emisión de los púlsares aún no se conocen del todo. Aunque la historia de los estudios de púlsares en bandas de radio se remonta a la década de 1960, los estudios de púlsares con rayos gamma de muy alta energía son relativamente más recientes. Por lo tanto, detectar nuevos púlsares y aumentar nue stro conocimiento sobre los descubiertos juega un papel crucial en la astrofísica de púlsares. Los telescopios Cherenkov son excelentes sistemas para estudiar fotones de muy alta energía provenientes de los púlsares.

Debido al hecho de que los púlsares son fuentes débiles en comparación con otras fuentes de rayos gamma, como los núcleos galácticos activos o las explosiones de rayos gamma, la calidad de los datos es de gran importancia para los resultados del análisis de datos, y uno de los efectos más considerables proviene de la condiciones atmosféricas. Por lo tanto, los sistemas de escaneo atmosférico como los Raman LIDAR que trabajan con los telescopios Cherenkov son sistemas cruciales para el análisis de datos.

El enfoque principal de este estudio son los estudios de púlsar con los telescopios MAGIC y el uso de los datos para las pruebas de Violación de Invariancia de Lorentz (LIV). Para ello, se han analizado y utilizado diez años de datos de Crab Pulsar para la prueba LIV. Además, se ha realizado por primera vez una búsqueda de emisión de VHE de un púlsar de milisegundos, PSR J0218 + 4232, en el modo estereoscópico de los telescopios MAGIC. Se ha analizado e incluido en este estudio una fuente BL Lac intermedia, 3C66A, en el campo de visión del púlsar de milisegundos. Además del análisis de la fuente astrofísica, en este estudio también se incluyeron algunos resultados de las pruebas del CTA Pathfinder Raman LIDAR y las pruebas de puesta en servicio.

La tesis sigue este esquema:

El capítulo 1 es una introducción a los púlsares. Se discuten los mecanismos de formación, evolución y emisión. El Capítulo 2 ofrece una descripción general de los estudios de Violación de In variancia de Lorentz con púlsares. El Capítulo 3 describe la técnica IACT, los telescopios MAGIC y el análisis de datos. El capítulo 4 ofrece una descripción general de los sistemas LIDAR utilizados para la caracterización atmosférica trabajando con los telescopios Cherenkov e incluye algunos resultados de las pruebas del Barcelona Raman LIDAR, "pathfinder" del "Cherenkov Telescope Array". El capítulo 5 se centra en la búsqueda de emisiones de VHE del púlsar de milise gundos PSR J0218 + 4232 y el análisis de la fuente IBL Lac 3C66A en el campo de visión. El Capítulo 6 se centra en el análisis de datos del Crab Pulsar 2009-2020 y el estudio sobre la emisión más alta hasta energías TeV. El Capítulo 7 muestra los resultados de la prueba LIV realizada con los datos mostrados en el capítulo anterior. Finalmente, se discutirán las observaciones finales y los aspectos futuros.

Chapter 1

Introduction to Pulsars

Pulsars are one of the most exotic objects in the universe that emit electromagnetic (EM) waves from radio to very high energy (VHE) gamma-rays. Radio astronomy studies of pulsars started in mid 20th century and were rapidly followed by pulsar discoveries in the visible, X-ray, and gamma-ray bands. Pulsar studies at VHE gamma-ray are the topic of this thesis. This waveband is relatively new and plays an essential role in understanding emission mechanisms and evolution scenarios nowadays.

In this chapter, the origin of the neutron stars and the discovery of the pulsars will be summarized. Their general properties, systems, evolution scenarios, and VHE gamma-ray emission mechanisms will be presented.

1.1 Origin of Neutron Stars

In the universe, molecular clouds like the Orion Nebula (see Figure 1.1) are the places where new stars are formed. These clouds get denser due to the gravitational collapse and form stellar objects like stars and planets. If the object at the center has a mass below 0.08 Mass of sun M_S, they become low mass stars, which are called brown dwarfs. On the other hand, if the mass of the object is higher than 0.08 M_S, they become protostars.

FIGURE 1.1: The Orion Nebula, or M42, is one of the brightest diffuse nebula and closest massive star formation region to Earth. (Credit:NASA and STScI)

Ejnar Hertzsprung and Henry Norris Russell discovered a relation between the surface temperature of the stars, their luminosities, and their masses. They simultaneously created a vital diagram, called the Hertzspung-Russel diagram (see Figure 1.2), for understanding the stellar evolution in the 1910s. As soon as the protostars get denser and start nuclear fusion reactions of H to He in their cores, their surface becomes more luminous, and temperature increases to a characteristic temperature that depends on their mass. They are located at the line called Main Sequence (MS), according to their mass. This line is also known as zero-age of the stars.

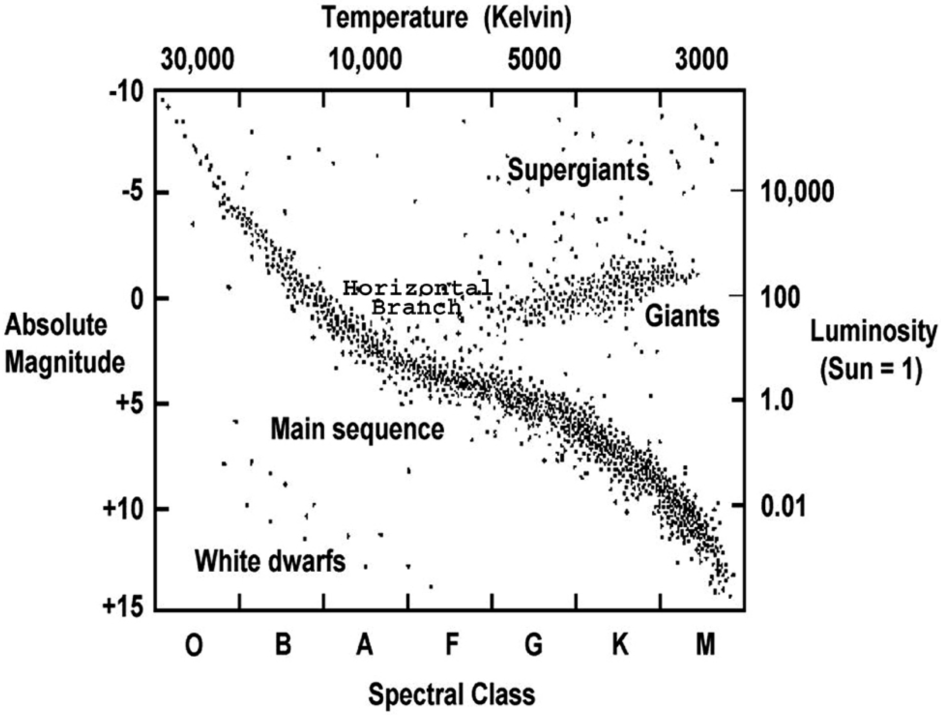

FIGURE 1.2: The Hertzsprung–Russell (H-R) diagram for stellar evolution (Credit Chandra X-ray Observatory). Stars are located at the Main Sequence line according to their mass. Low-mass stars evolve through the Horizontal Branch and the Giant phase while the massive stars evolve through the Supergiant phase (see diagram 1.3). As soon as nuclear fuel finishes, they end up as either white dwarfs located at the lower-left part or black holes and neutron stars, which have high temperature and are place out of the plot.

In the later stages of central nuclear reactions, if the star is massive enough, the core temperature increases to a level that He fusion reactions can start, and H shell burning occurs. Consequently, the radius of the star expands, and this phase is called the Giant phase for low mass stars. On the other hand, for the massive stars, He fusion is followed by C and O fusions, and the star gets into the Supergiant phase. At the end of the Giant and Supergiant phases, the core fusion reactions vanish. As a result, an unbalance between pressure and gravitational forces occurs. The core starts to collapse for the low-mass stars, and they end up as white dwarfs. Chandrasekhar, 1931 proposed that these objects are so dense that their electrons are in a degeneracy state where each electron occupies a different quantum state (according to Pauli exclusion principle); meanwhile, they are at the same energy level.

On the other hand, massive stars experience a different path and undergo an

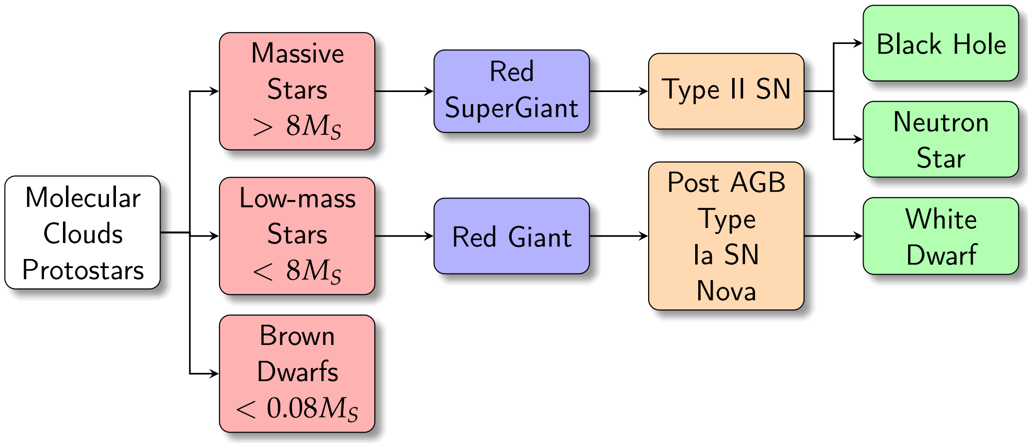

FIGURE 1.3: The lifespan of the stars. In the early stage of the stars, the protostars are formed in the molecular clouds. Afterward, they become either stars and are located at the Main Sequence line when nuclear reactions start in their cores or Brown Dwarfs, which do not have enough mass to trigger the core reactions. When the H burning nuclear reaction stops for the stars, they either move to a giant phase. After the giant phase, massive stars have a Type II Supernova (SN) explosion, and the compact core either becomes a black hole or neutron star surrounded by the supernova remnant. Low mass-stars are more complicated in this stage. If they are isolated stars, they release their material during the Post asymptotic giant branch (AGB) and become white dwarfs surrounded by a planetary nebula. However, if they are in a binary system, the white dwarf accretes material from its companion star and can have Type Ia SN explosion or Nova explosion.

explosion called supernova (SN) explosion; the core collapses even faster and forms a compact object. According to the size of the star, the core can get as dense as creating a matter with neutron degeneracy as calculated by Tolman, Oppenheimer, and Volkoff (Oppenheimer and Volkoff, 1939). They are called neutron stars (Baade and Zwicky, 1934). If the mass of the star is even higher, the collapsed core can become a black hole, first calculated by Schwarzschild (Schwarzschild, 1916).

1.2 Discovery of Pulsars

Neutron stars were firstly theoretically proposed before they were discovered. Although the theoretical discussion started with the neutron degeneracy in the 1930s, there was no significant study on neutron stars until 1968 when Pacini claimed a neutron star existence as the power source at the center of the Crab Nebula (Pacini, 1968). Immediately after this, the unexpected expansion rate of the Crab Nebula was associated with the pulsar (Trimble, 1968).

Shortly after, Jocelyn Bell and Antony Hewish detected the first extraterrestrial repeating pulsations in radio (Hewish et al., 1968) Figure 1.4. Dispersion relation in their radio signals indicated that the source was galactic. After excluding the idea of solar system origin or intelligent life forms, they proposed that the pulsations come from either white dwarfs or neutron stars. Antony Hewish and Martin Ryle were awarded the Nobel Prize in Physics in 1974 for discovering the first pulsar.

Detection of more pulsars followed the first discovery immediately, including the best-known ones such as Crab Pulsar (Staelin and Reifenstein, 1968), Vela Pulsar

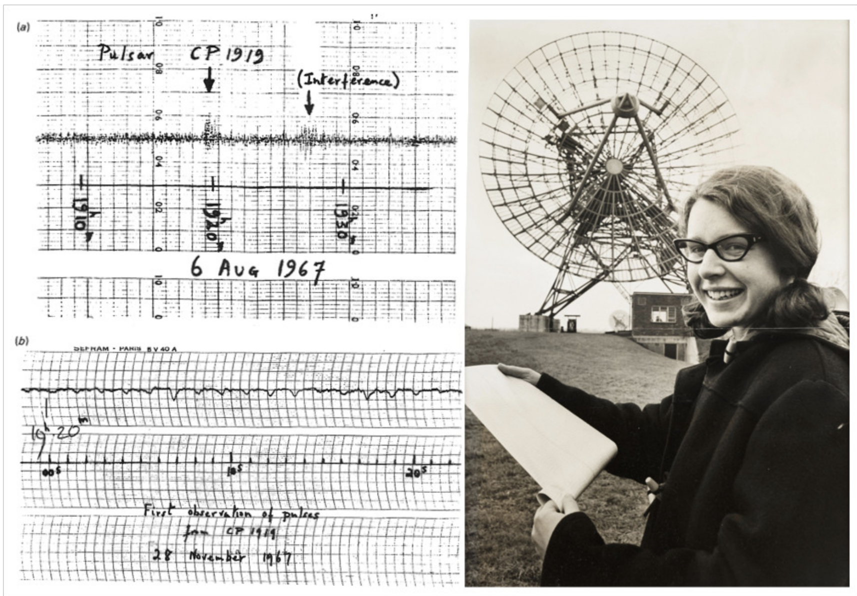

FIGURE 1.4: Jocelyn Bell and discovery of the first pulsar (credit Cavendish Laboratory).

(Large, Vaughan, and Mills, 1968), and Geminga Pulsar (Thompson et al., 1977). Today, almost 2000 pulsars are known, which are observable in various wavebands from radio to VHE (see gamma-ray pulsars map in Figure 1.5).

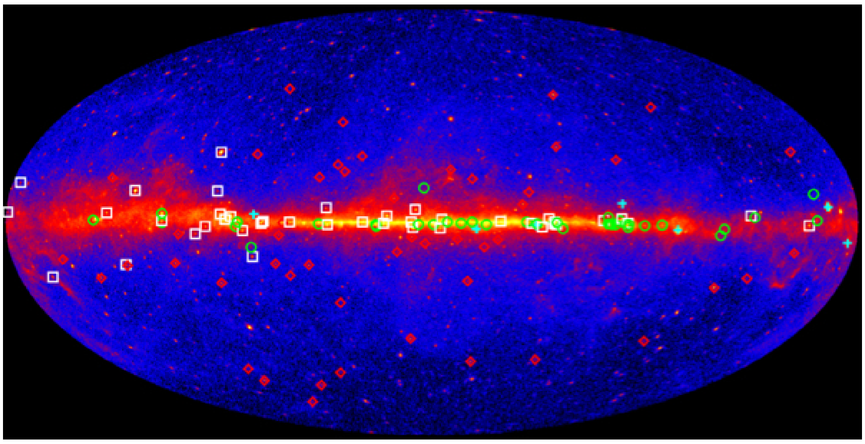

FIGURE 1.5: Gamma-ray pulsars detected by Fermi-LAT: pulsars detected by the Compton Gamma Ray Observatory (CGRO) (plus), young radio-selected (circle), young gamma-selected (square), and millisecond pulsars (MSPs) (diamond). (Credit: Fermi-LAT/GSFC)

1.3 General Properties of Neutron Stars

Neutron stars are highly magnetized and very dense, fast-spinning objects. They are neutron-rich objects in which the majority of the mass is composed of neutrons in the degenerate state. Their radii are around 10km, and their masses vary between 1 to 2 $M_\odot$ (Özel and Freire, 2016).

The interior of the neutron stars is not fully known. Basically they consist of four main layers: outer crust, inner crust, outer core, and inner core (see Figure 1.6).

There is an electron-positron plasma surrounding the neutron star, which fills the magnetosphere. The outer crust layer consists of electrons, ions, and neutron-rich nuclei, while the inner crust layer has more pressure where the neutrons become superfluid. The core is so dense that most of the mass of the neutron star is in here. The composition of the inner core is still unknown.

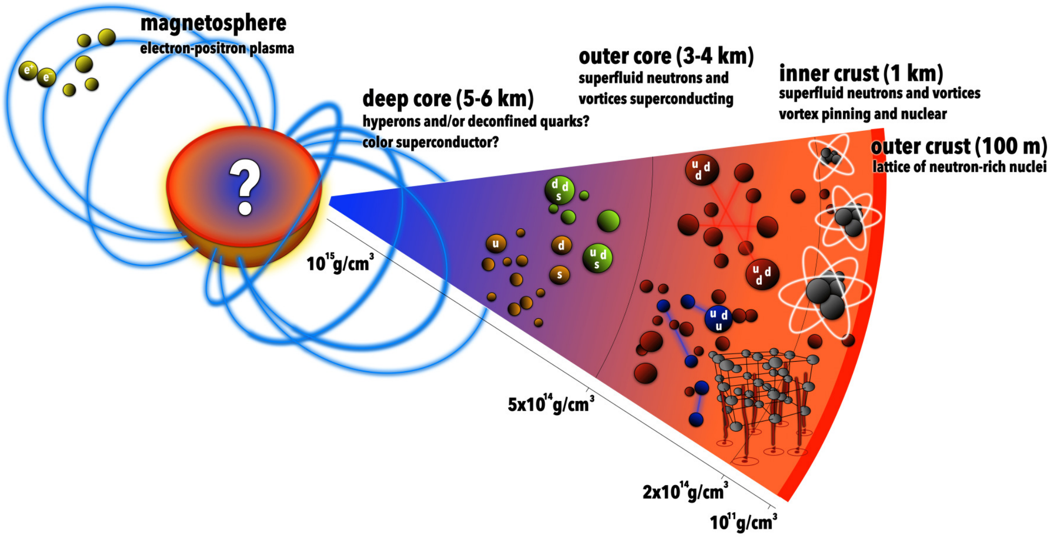

FIGURE 1.6: Schematic structure of a neutron star (A. Watts et al., 2015).The outer layer is a solid ionic crust formed of neutron-rich nuclei and supported by electron degeneracy pressure. Between the inner and outer crust, neutrons begin to leak out of nuclei, and the neutron degeneracy pressure increases. The inner crust is filled with superfluid neutrons. In the core, the densities are so high that nuclei are dissolved. The composition of the deep core is not known; it could be filled with quarks or hyperons.

Neutron stars have strong magnetic fields around 10^{10} G. They are thought of as rotating dipole fields with a magnetosphere. Different global magnetosphere models have been developed to understand the electrodynamics of this region. They are vacuum retarded dipole (VRD) model, force-free (FF) and dissipative models, and kinematic models.

VRD model was introduced before discovering the first pulsar (Deutsch, 1955) and described the electric and magnetic fields in the dipole field of a star rotating in a vacuum. The analytical solution of this model foresees a powerful electric field parallel ($E_{\parallel}$) to the magnetic field close to the surface of the star.

In 1969, Goldreich and Julian argued that a rotating neutron star could not be surrounded by a vacuum (Goldreich and Julian, 1969). Because $E_{\parallel}$ would draw charges from the surface of the neutron star and initiate pair cascades which form a plasma structure filling the magnetosphere (see Figure 1.7). The charge density of this plasma is called Goldreich Julian density, σ_{GJ}. Magnetic field lines co-rotate with the speed of the neutron star. At a radius called light cylinder radius (R_{LC}), the co-rotation speed becomes equal to the speed of light. Hence starting from that radius, the magnetic field lines can not be closed anymore. R_{LC} is calculated with the following equation (Equation 1.1), where c is the speed of light, and P is the spin period of the neutron star.

$$R_{LC} = \frac{cP}{2\pi} \tag{1.1}$$

Their magnetic field strength at the surface and R_{LC} are calculated with the following equations that $\dot{P}$ is the spin period derivative of the pulsar:

$$B_{Surface}(Gauss) > 3.2x10^{19}\sqrt{P\dot{P}} \tag{1.2}$$

$$B_{LC}(Gauss) \approx 2.94 \times 10^{8}\sqrt{\dot{P}P^{-5}} \tag{1.3}$$

Their characteristic ages (τ_C) are calculated with the following equation (see Equation 1.4

$$\tau_C = \frac{P}{2\dot{P}} \tag{1.4}$$

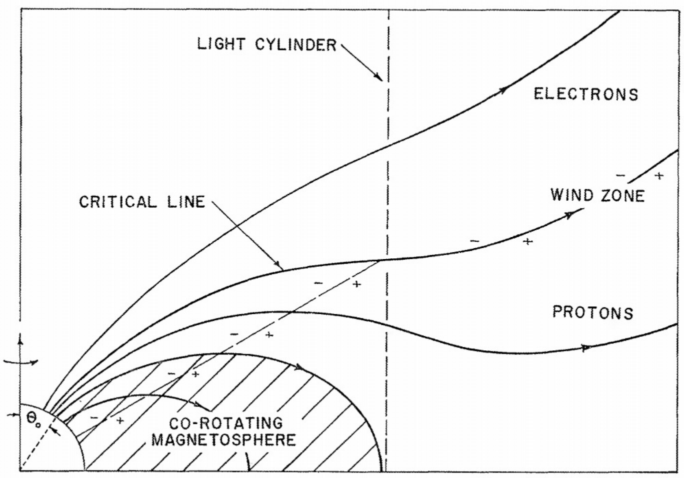

FIGURE 1.7: Neutron Star magnetosphere (Goldreich and Julian, 1969). The magnetosphere co-rotates with the neutron star up to the light cylinder, and beyond, the magnetic field lines are not closed anymore where the charged particles are transferred with the pulsar winds. The potential of the electric field is equal to the interstellar medium at the critical line where the run-away charged particles (electrons and protons) are separated.

Force-free (FF) models solve Maxwell's equations ignoring the plasma pressure and requiring $E_{\parallel}$, where **E.B**=0. This ideal case was turned into the Pulsar equation by Michel, 1973, and it was first solved numerically by Contopoulos, Kazanas, and Fendt, 1999. As a result, the current of the charged particles moves out mainly on a current sheet along the last closed field surface (separatrix) inside the LC and the equatorial plane away from the LC (see Figure 1.8). However, FF models do not represent pulsars perfectly with the **E.B**=0 conditions, so this condition is relaxed with dissipative solutions.

Kinetic models, on the other hand, focus on particle motions and fields by using kinetic plasma simulations. For this purpose, Particle-in-cell (PIC) models have been applied to the pulsars magnetospheres by solving Maxwell's equations and particle equations of motions simultaneously through injecting electron-positron pairs to the magnetosphere. 3D Cartesian (Philippov and Spitkovsky, 2014) or 2D spherical current sheet models (A. Y. Chen and Beloborodov, 2014) are being used.Lately, Kalapotharakos et al., 2018, and Brambilla et al., 2018 showed that FF magnetosphere could be formed at all inclination angles if large enough pairs are injected.

The actual structure of the magnetosphere is still unknown and observational results of the pulsars will help to shed light on understanding this region.

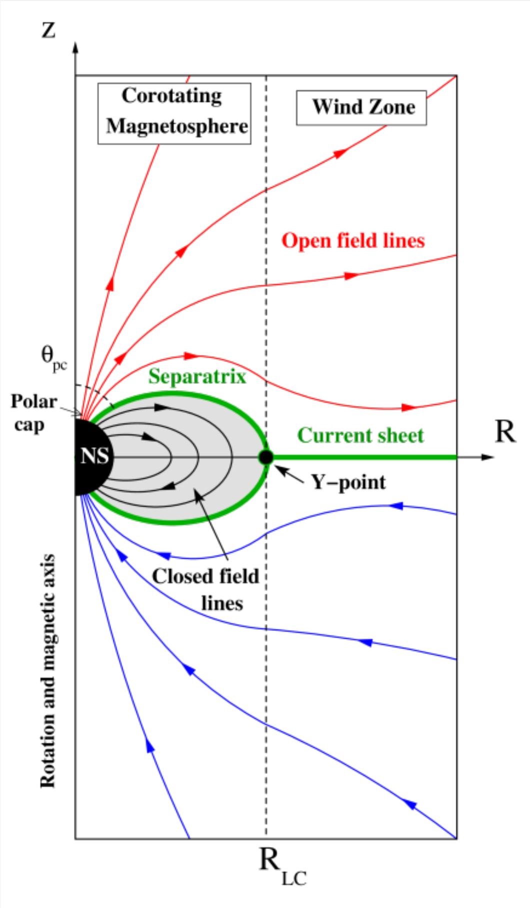

FIGURE 1.8: Sketch of current-sheets (Cerutti and Beloborodov, 2017). Red and blue lines represent the open field lines that extend beyond the light cylinder. VHE emission, according to this theory, occurs in the green current sheet line, which locates between the opposite magnetic fluxes in the wind zone. These current sheets divide the light cylinder into two separatrix current sheets between the last open and the first closed field lines.

1.4 Pulsar Systems

Most of the pulsars are isolated systems either originated from isolated MS massive stars or disrupted binary MS star systems because of the supernova explosions. The high spin periods of the neutron stars originated from the angular momentum they gained due to the core collapse, which slows down in time. This energy release becomes the source of rotation-powered pulsars (RPP) (see Figure 1.9).

On the other hand, the discovery of the first binary pulsar system PSR B1913+16 (Hulse and Taylor, 1975) was an unexpected case due to the supernova impact.

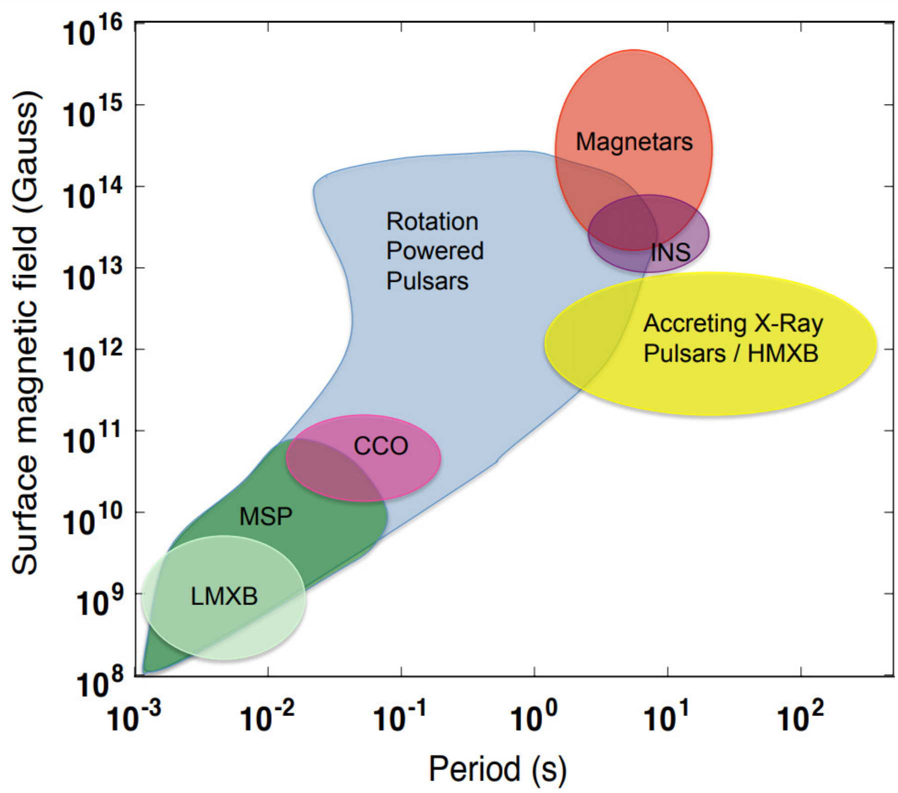

FIGURE 1.9: Diagram of neutron star populations (Alice K. Harding, 2013) showing period of the neutron stars vs. their surface magnetic field strengths. The majority of the neutron stars are Rotation Powered Pulsars (RPP), with subgroups Central compact Objects(CCOs), Millisecond Pulsars (MSPs), Low-Mass X-ray Binaries (LMXB). This group overlaps with a special kind of isolated neutron stars (INS) showing quasi-thermal x-ray emissions, magnetars, and Accreting X-ray Pulsars/High-Mass X-ray Binaries.

There are two main binary systems called X-ray binaries and newly discovered Gamma-ray binaries. In addition to RPPs in the binary systems, there are accretion-powered (APP) and nuclear-powered pulsars (NPP). They are powered by the material accreted onto their surfaces. X-ray binary systems are divided into two subsystems, low-mass X-ray binary systems (LMXB) with companion stars, usually white dwarfs. The other one is high-mass X-ray binary systems (HMXB) with massive companions, white dwarfs, neutron stars, MS stars, black holes. The evolution of the X-ray binaries is explained in Figure 1.10.

If the binary system is an MS star and reaches the red giant phase, a mass transfer geometry called Roche-Lobe overflow (RLOF) can occur. This mass transfer can create a disc around the pulsar(see Figure 1.11), and accretion of material onto the surface can be possible. The pulsar can gain angular momentum and speed up (Bisnovatyi-Kogan and Komberg, 1974). This theory well described that the Hulse-Taylor pulsar has a higher spin period and lower B field than most of the pulsars.

After the discovery of the first isolated millisecond pulsar PSR B1937+21 (Backer et al., 1982), two independent groups claimed simultaneously that the millisecond pulsar speeded up by mass transfer in a binary system (Alpar et al., 1982), (Radhakrishnan and Srinivasan, 1982). The theory predicted the spin period of PSR B1937+21 and PSR B1913+16 precisely (See Figure 1.12). As soon as the first binary millisecond

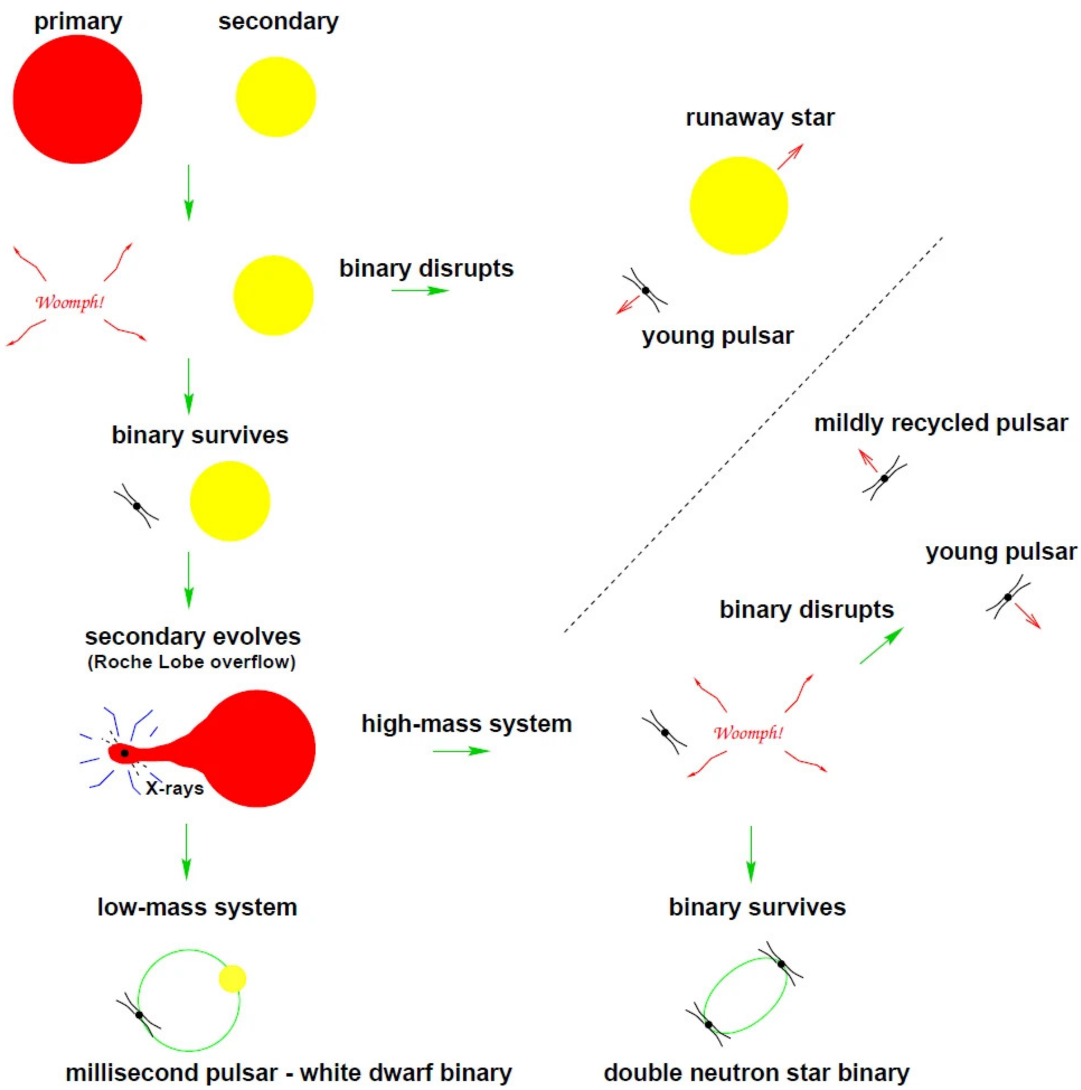

FIGURE 1.10: Binary pulsar evolution (Lorimer, 2005). The sketch explains the binary evolution starting from the left upper part, where two MS stars are binaries. The massive primary star evolves faster than the secondary companion, and the supernova explosion disrupts the binary, which ends up as a run-away star and a young isolated pulsar. Rarely, the binary survives, and the neutron star starts to accrete material from the secondary star via Roche Lobe overflow and shows X-ray emission. Depending on the mass of the secondary star, the binary is called LMXB or HMXB. LMXB systems end up as white dwarf millisecond pulsar binaries. However, HMXB systems go through a supernova explosion of the secondary star and end up as either mildly recycled pulsars or double neutron stars.

pulsar system was discovered, LMXB SAX 1808.4-3658 (Wijnands and van der Klis, 1998), the theory was confirmed.

According to the recycled theory (Srinivasan, 2010), the accretion rates play a crucial role in the final spin period, which is related to the inner edge of the disc. The accretion rate is parametrized by two radiuses, Alfven radius R_A where the ram pressure of the infalling material equals to the magnetic pressure (see Equation 1.5, and co-rotation radius R_C where the angular velocity of the disc and the neutron star

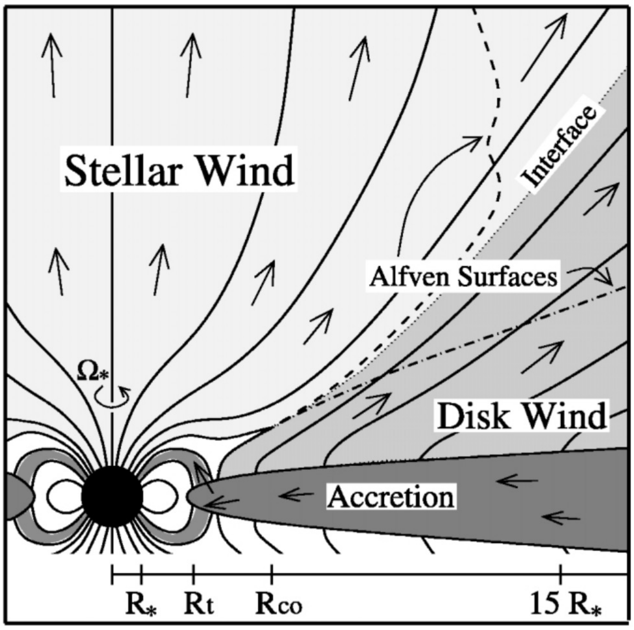

FIGURE 1.11: Schematic of the star disk interaction (Matt and Pudritz, 2005). R_t is the inner edge of the accretion disk, which is connected to the magnetic field. Co-rotation radius, R_{co} and the radius of the star is shown with R_*. Matter, energy, and angular momentum can be transferred to the star with the help of the magnetic field. Matter and the angular momentum flow are shown with the arrows. The location of the Alfven surfaces is shown with the dashed lines. The stellar and disc winds are shown with the dashed-dotted lines.

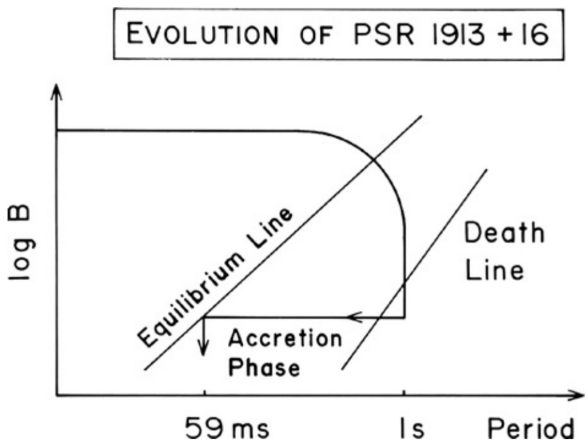

FIGURE 1.12: Recycled evolution scenario of PSR B1913+16 (Srinivasan, 2010). As soon as PSR 1913+16 got older and slower, it dropped below the death line known as the pulsar graveyard that we can not observe pulsations anymore. However, PSR 1913+16 is in a binary system. Some materials were accreted from the companion star, and the pulsar spun up to the equilibrium line. The observed spin period and the calculated value by the recycled theory precisely matches.

are equal (see Equation 1.5).

$$R_A = \left(\frac{B^2 R^{12}}{8GM\dot{M}_a^2} \right)^{\frac{1}{7}} \tag{1.5}$$

$$R_C = \left(\frac{GM}{\Omega^2}\right)^{\frac{1}{3}} \tag{1.6}$$

If $R_A > R_C$, the infalling matter will be expelled. Hence, if $R_A < R_C$, material will be accreted until $R_A = R_C$ that the system is in equilibrium. The minimum spin period (P_{eq}) for this equilibrium is limited by the Eddington limit, which is the highest luminosity of a star for balancing the outward pressure and inward gravitational force. If this limit is exceeded, the outer layers of the star would be blown off. This minimum spin period limits the maximum accretion rate (see Equation 1.7).

$$P_{eq} \propto B^{\frac{6}{7}} \dot{M}^{-\frac{3}{7}} \tag{1.7}$$

LMXBs have lower accretion rates compared to HMXBs. Therefore the final spin period is shorter in the LMXBs, which can be even faster than young pulsars (see Figure 1.13) and becomes MSPs. However, HMXBs can not spin up as much as MSPs, and they become mildly recycled pulsars.

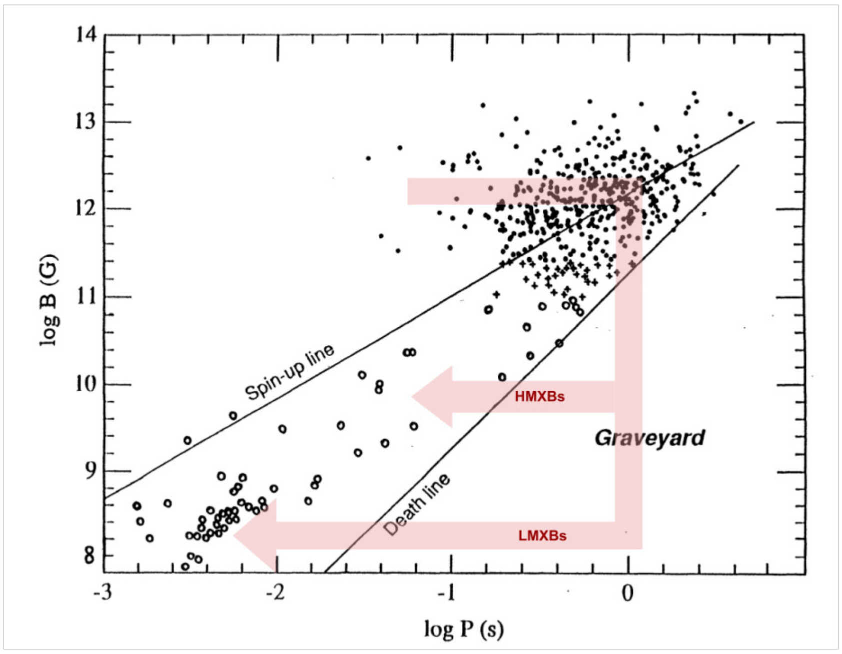

FIGURE 1.13: Evolution scenario of pulsars with log P vs. log B diagram adapted from (Ziólkowski, 1997). The evolution paths of the young pulsars until they become mildly recycled pulsars or MSPs are shown with the red arrows. Young pulsars spin down in time, and their surface magnetic field strength also lowers proportionally. They become middle-aged pulsars and then drop below the death line. When the neutron star is in a binary system, it can accumulate matter from the companion star, and its spin period decreases due to the gained angular momentum. The spin period at which they can reach the maximum is limited to the spin-up line, predicted by the Eddington luminosity limit for accretion rates. For the HMXB systems, the accretion rates are high; therefore, mildly recycled pulsars are formed. However, for the LMXB systems, the pulsar can speed up until it becomes a millisecond pulsar with shorter spin periods and lower magnetic fields.

1.5 VHE Emission Mechanisms of Pulsars

Pulsars emit at almost any wavelength. Basically, they have two main characteristics: thermal emission and non-thermal emission. This section will mainly focus on the VHE gamma-ray emission mechanisms, which is the interest of this thesis.

Thermal emission is due to blackbody (BB) radiation and usually comes from the surface of the neutron star. It could be due to the temperature of the pulsar surface or some hotter regions called hots spots. They are mainly located close to the magnetic poles, and in some cases, accreted material heats their surfaces. The highest frequency reached by the BB radiation component is in the X-ray band. The gamma-ray emission via BB radiation is not possible in the universe because it requires extremely high temperatures that astrophysical objects can not achieve.

Non-thermal emission, on the other hand, is the source of gamma-ray emission from the pulsars. When the particles are accelerated up to relativistic speeds, pulsars can emit gamma-rays up to TeV energies. The emission is modeled with a power-law (PWL) function. Although it is thought that the VHE emission comes from the magnetosphere, the exact physical driving mechanisms are not yet known. The Discovery of the VHE emission from pulsars is challenging magnetosphere models. There are three main mechanisms possibly responsible for the VHE emission from pulsars: Curvature Radiation (CR), Synchrotron Radiation (SR), and Inverse Compton Scattering (ICS) (see Figure 1.14).

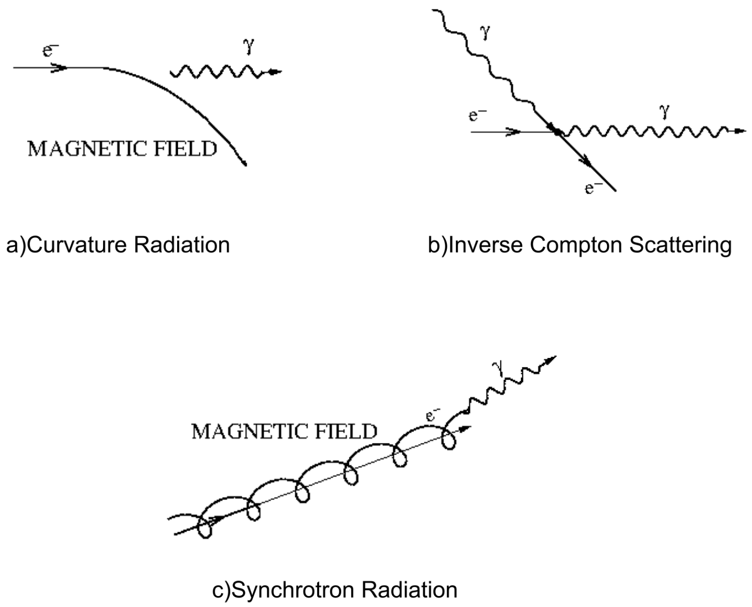

FIGURE 1.14: Possible gamma-ray emission mechanisms for the pulsars. Gamma-ray emission from Synchrotron (c) and Curvature (a) radiations occur when relativistic electrons move in strong magnetic field regions. Curvature radiation produces gamma-rays parallel to the magnetic field while the magnetic field trajectory is curved. Synchrotron radiation, however, produces gamma-rays with an angle to the magnetic field line while electrons are following helicoidal trajectories. Inverse Compton scattering (b) is a process by which a gamma-ray photon gains energy through the interaction with an ultra-relativistic electron. Figures are taken from (Oya, 2010)

All VHE emission models of the pulsars have been reviewed in detail by Alice K. Harding, 2021 recently. There are four main theoretical models that propose different emission locations and different driving mechanisms. The primary purpose of the models is to predict the spectra and phaseogram of the observed pulsars.

- **Polar Cap Models :** Polar cap (PC) models (M. A. Ruderman and Sutherland, 1975) (Baring, 2004) (Daugherty and A. K. Harding, 1982) are one of the oldest models to explain the pulsar emission. According to this model, the emission source is CR from the accelerated particles through the strong and curved magnetic open-field lines close to the polar cap region (see Figure 1.15). This model can explain the coherent radio emission from the pulsars. Besides, the predicted HE gamma-ray emission cut-off from pulsars observed by Fermi-LAT (Abdo et al., 2013) could be explained by the pair production that occurs at the powerful magnetic field, which screens the fields and causes a shortage of gamma-rays. When the VHE emission from the Crab Pulsar was detected by the MAGIC Telescopes (Aliu et al., 2008) and emission above 100 GeV was reported by VERITAS (VERITAS Collaboration et al., 2011) this model was ruled out for explaining the VHE gamma-ray emission from young pulsars.

  Although the CR does not allow the VHE emission of the young pulsars due to the pair production, the Pair-Starved Polar Cap (PSPC) model (Muslimov and Alice K. Harding, 2004b) proposes that the situation could be different for the MSPs. Their surface magnetic field strengths are weaker than the young pulsars, so that the voltage drop may not be enough for creating the electron-positron pairs close to PC. In this way, the field lines will not be screened, and VHE emission could happen at higher altitudes with a larger fraction. With this model, Harding and Kalapotharakos propose that MSPs can emit TeV energetic gamma-rays similar to Vela Pulsar (Djannati-Ataı¨ et al., 2017).

- **Outer Gap Models :** Outer gap (OG) models (Cheng, Ho, and M. Ruderman, 1986)(Hirotani, 2008)(Tang et al., 2008) are the other model as old as the PC. According to this model, there could be null charge surfaces between two charge distinction regions specified in Figure 1.7. Vacuum gaps could be formed in these regions as in the VRD model. After one sign of the charges runs away through the open field line, the particles can not be replaced; thus, the charged particles can be accelerated with $E_{\parallel}$ formed in the gap. The source of the charged particles can not be pair production as in the PC model because the magnetic field strength is lower in the outer layers. Instead, they could be created by two-photon pair production by thermal and non-thermal X-ray photons. The accelerated particles close to the PC hit the neutron star surface and could create hot spots where thermal X-ray radiation is emitted. Some photons could be reflected through the surface of the neutron star, by which the colder non-thermal X-ray photons could be produced. Compton scattering is thought to be the source of the VHE gamma-ray emissions. Lyutikov, 2013 proposed a mechanism called Synchrotron self-Compton (SCS) radiation from the pairs which can produce the Crab spectrum from UV to VHE gamma-rays, which the Inverse Compton Scattering is dominating the VHE.

  The OG model predicts VHE emission from MSPs, too, which requires multipole fields to create enough pair cascades. Two thermal components are expected: a non-thermal downward-going X-ray SR component originated from near-surface pairs and an upward-going high energy gamma-ray synchro curvature component from the outer gap. But this model predicts a large phase shift between X-ray and gamma-ray pulse, which is not consistent with some in-phase MSPs such as PSR B1821-24 and PSR J0218+4232 (Alice K. Harding, 2021).

- **Slot Gap and Annular Gap Models :** The slot Gap model is a narrow set of field lines near the last open field line where $E_{\|}$=0 according to FF solution. Particles can be accelerated slowly without triggering pair production and screening the $E_{\|}$. This acceleration continues to high altitudes (Arons and Scharlemann, 1979), and HE emission can occur during this travel starting from the neutron star surface up to the light cylinder (Muslimov and Alice K. Harding, 2004a) (see Figure 1.15).

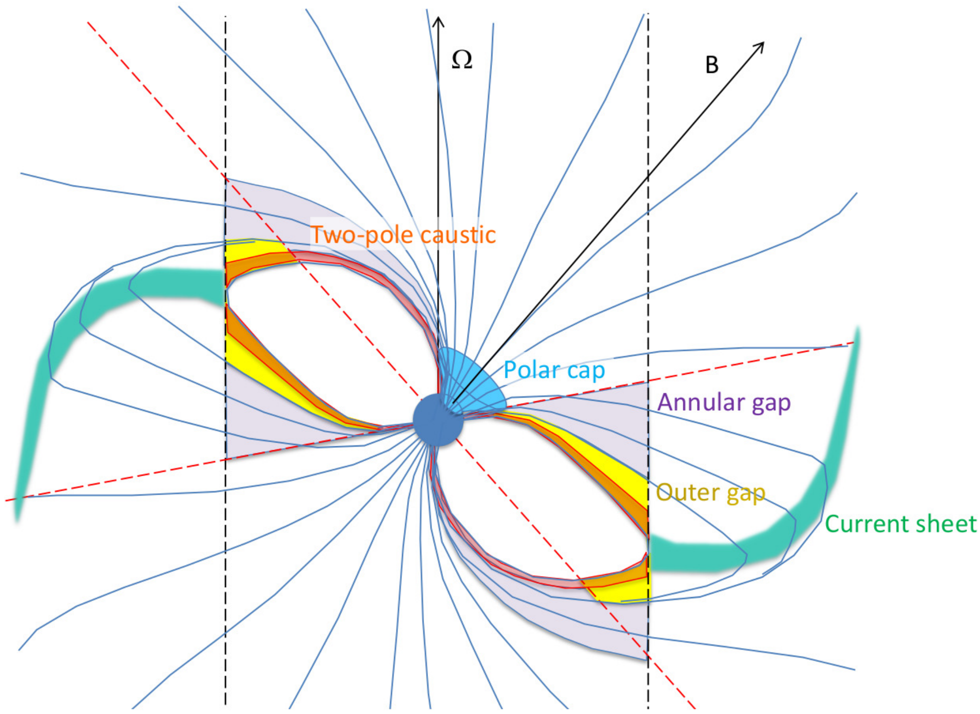

FIGURE 1.15: Locations of the VHE pulsar emission models (Alice K. Harding, 2021). Spin axis (Ω), magnetic axis(B) are shown with black lines, while light cylinder boundaries and projections of the null-charge surface are shown with black and red dashed lines, respectively. The polar cap model (blue) ruled out for the VHE emission because the pair production close to the polar caps would induce a sharp cut-off in the gamma-ray spectrum. It is believed that emission occurs close to the light cylinder, and the possible emission models are the outer gap (yellow), two-pole caustic (red), annular gap (purple), and current sheet (green) models.

Two-Pole Caustic Model (TPC) (Dyks and Rudak, 2003) is predicting caustic patterns from both magnetic fields (see Figure 1.15). These in-phase radiations originated by the canceled out aberration and light travel time delays of radiation due to the curved field. Both the SG and TPC models can predict two separated peaks with phase-shifted from radio peaks similar to Fermi pulsars.

The annular gap (AG) model was first proposed by (G. J. Qiao et al., 2004)(G.-J. Qiao et al., 2007) and further developed by (Du et al., 2011)(Du, G. J. Qiao, and Wang, 2012). It combines the advantages of PC, SG, and OG models. The annular gap model is geometrically similar to the SG model. According to this model, there are two separated PC regions: the core gap close to the magnetic axis and critical lines; and the annular gap region between the critical field lines and the last open field lines. AG assumes a quasi-neutral pair plasma magnetosphere contrary to the charge-separated OG model. Although $E_{\parallel}$ is screened in the core region, the annular gap region is contrary to this, and the acceleration can continue to high altitudes. The caustics of HE light curves are similar to SG and can produce the light curves of short spinning pulsars like young pulsars and MSPs (Du, G. J. Qiao, and D. Chen, 2013).

- **Current Sheet Models :** Pulsed HE emission from current sheets (Kirk, Skjæraasen, and Gallant, 2002) are modeled by striped pulsar wind model (Coroniti, 1990) that particles radiate Doppler-boosted SR, and pulsed emission will be observed whenever current sheets are on the line of sight. According to the dissipative solutions, the emission occurs outside the light cylinder and is limited to 50 R_{LC} by Pétri, 2012. This model can explain the optical polarization of the Crab Pulsar.

  Pulsar emission at GeV energies is assumed as a result of CR (Kalapotharakos, Alice K. Harding, and Kazanas, 2014). SSC can explain the VHE emission from the young pulsars and MSPs. MSPs are expected to have higher energetic pairs due to their low magnetic fields compared to the young pulsars (Alice K. Harding and Kalapotharakos, 2015). Alice K. Harding, 2021 predicts that MSPs like PSR B1821-24 and B1937+21 can have SED peaks at energies near 100 GeV. However, Harding also proposes that Klein-Nishina (KN) effects will suppress the SSC components of MSPs, and they may not be detectable by current VHE telescopes. ICS component, however, is thought of as the driving mechanism of the TeV emission from the Vela Pulsar and Crab Pulsar. ICS component is also predicted to be observed from Crab-like young pulsars and energetic MSPs (Alice K. Harding, 2021).

VHE emission from the pulsars has been challenging for the emission models; therefore, VHE observations and discovery of new pulsars are essential to understand pulsar physics. As well as the young or middle-aged pulsars, the discovery of the first MSP will probably be a key point for the emission models due to their lower magnetic field and higher spin period compared to the young pulsars.

In addition to VHE gamma-ray emission directly from pulsars, they can also cause emission around them. The escaping electron-positrons can create a wind called a pulsar wind nebula (PWN). If the supernova remnant of the pulsar is not entirely disappeared as it gets older, the PWN can interact with the remnant and creates a shock where non-thermal VHE gamma rays can be emitted (see Figure 1.16).

Besides the close environment, the pulsars can also emit VHE gamma-ray by interacting with their companion stars in the binary systems. These are called gamma-ray binaries and can be grouped into three main classes (see Figure 1.17. The Be-star pulsar binaries, in which the gamma-ray emission may occur while the pulsar is orbiting through the disc of the Be-star companion. The microquasars can be formed by either pulsars or black holes, and they accrete material from their companion massive stars. If the accretion reaches exceptionally high levels, the matter can be expelled through the magnetic poles and creates jets, and VHE gamma-ray emission can be observed. Lastly, in some massive companion binary systems, while the pulsar is orbiting behind the companion star according to our FoV, the photons from the pulsar can interact with the massive star UV and gamma-ray can be produced from photon-photon scattering.

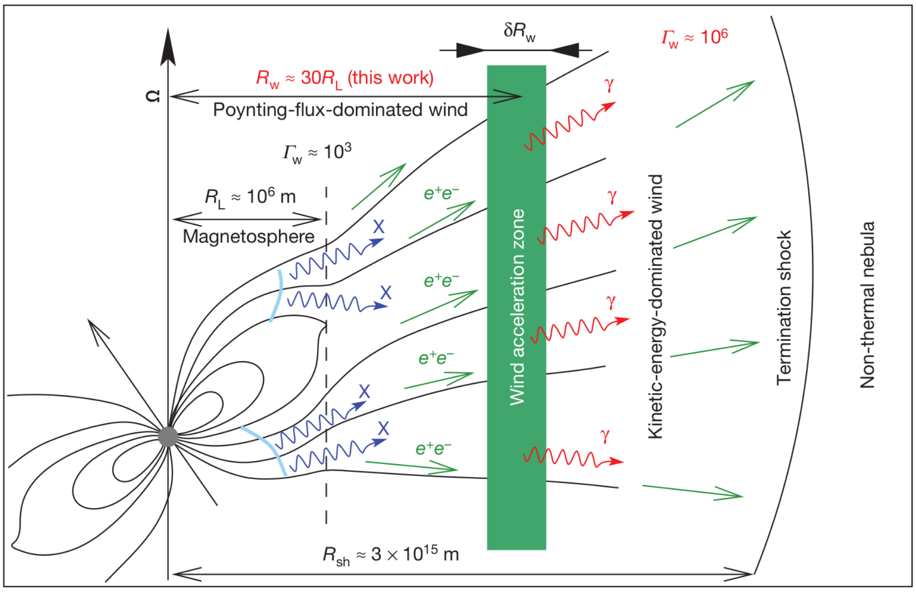

FIGURE 1.16: A sketch of Pulsar Wind Nebula and the non-thermal nebula interaction of Crab Nebula and the Crab Pulsar (Aharonian, Bogovalov, and Khangulyan, 2012a). VHE gamma-ray emission is produced with this interaction, and as a result, the Crab Nebula is observed up to hundreds of TeVs.

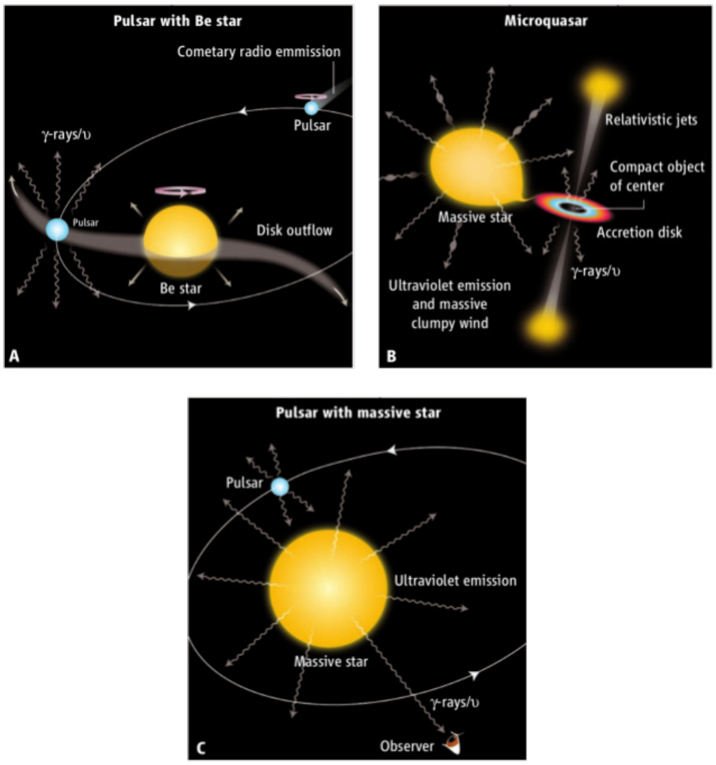

FIGURE 1.17: Illustrations of Pulsar Be-star binary systems, microquasars and pulsar massive star systems which can produce gamma-ray emissions (Mirabel, 2012).

Chapter 2

Lorentz Invariance Violation with Pulsars

Pulsars are the densest and fastest-spinning astrophysical sources in the universe that are directly observable. Their inner core is so dense that it is impossible to create similar conditions in our laboratories. Moreover, each pulsar has characteristic sharp periodical timing features that make them unique clocks in the universe. Those features have been already used for either testing fundamental physics theories or using them as GPS tools in the universe like Voyager (see Figure 2.1).

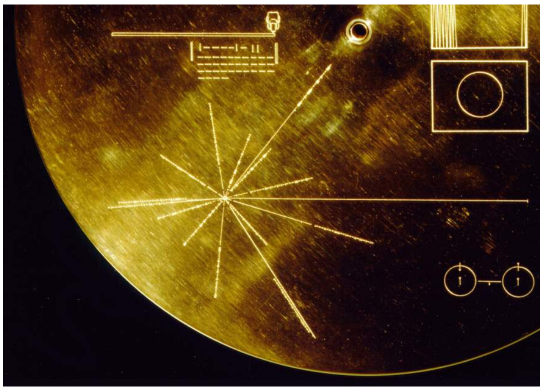

FIGURE 2.1: Pulsar map fragment of Golden Record, shipped with Voyager spacecraft in 1977 (Credit: NASA/JPL). The location of the Earth was shown in this map by using 15 known luminous pulsars whose spin periods were coded as binary bases.

Some of the Quantum Gravity (QG) theories predict Lorentz Invariance Violation (LIV), which could create a difference in the speed of light in the vacuum. VHE gamma-ray emitter pulsars are one of the sources for testing these theories.

In this chapter, a general view of the pulsar studies for fundamental physics will be reviewed. Afterward, LIV will be explained, and the Time-of-Flight(ToF) studies with pulsars will be revealed. Lastly, LIV limits obtained with the ToF studies will be presented.

2.1 Fundamental Physics Studies with Pulsars

Pulsars' inner core densities are so high that they can reach nuclear densities, which makes them good targets for Standard Model (SM) studies such as Quantum Chromodynamics(QCD) (Özel et al., 2010). Different mass-radius relations (see Figure 2.2) can produce distinct conditions for the inner core of the pulsars, which can be used for studying elementary particles. For instance, the existence of exotic stars such as quark stars or strange stars (Weber, Negreiros, and Rosenfield, 2007). For a detailed review, see (Özel and Freire, 2016).

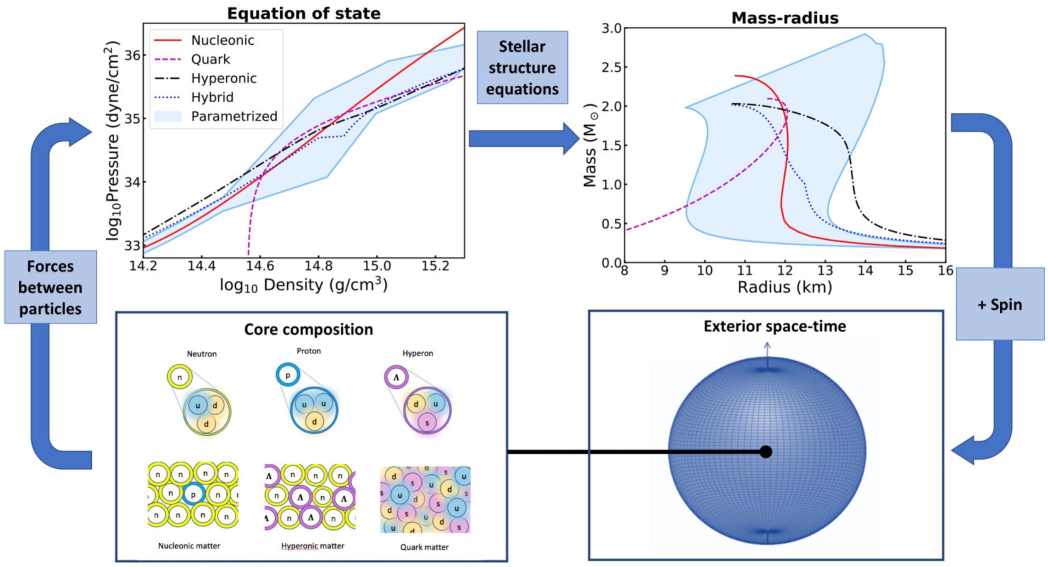

FIGURE 2.2: Neutron Star mass-radius relations predicted with the core composition models are shown (A. L. Watts, 2019).

Neutron Stars are also good targets for General Relativity studies. Hulse and Taylor were awarded the Nobel prize for discovering the first double-pulsar binary, which was predicted to play a key role in gravitational wave detection studies. Indeed, the LIGO and the VIRGO experiments have already detected (Abbott et al., 2017) gravitational waves from neutron star mergers (see Figure 2.4).

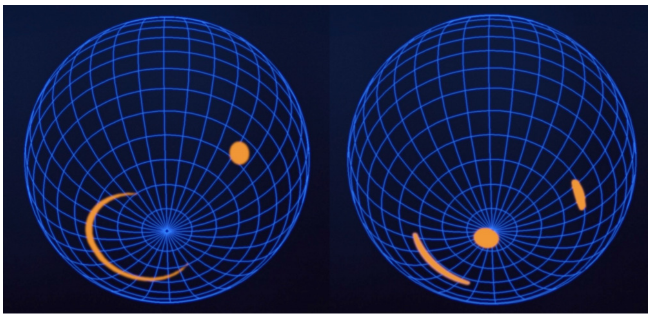

FIGURE 2.3: Gravitational bending effect observation in PSR J0030+0451 by two independent groups: Riley et al., 2019 (left panel), and Miller et al., 2019 (right panel). The NICER results show that the emission observed from the source is originated from one hot spot affected by the gravitational bending. It was still observable even though it was on the backside of the pulsar. (Credit: NASA)

Apart from the pulsar binary mergers, the surfaces of the pulsars are also testing targets for gravitational bending observations (see Figure 2.3).

One of the other fundamental physics studies that pulsars are used is Standard Model Extension (SME), in which SM, GR, and breaking of Lorentz symmetry are being studied.

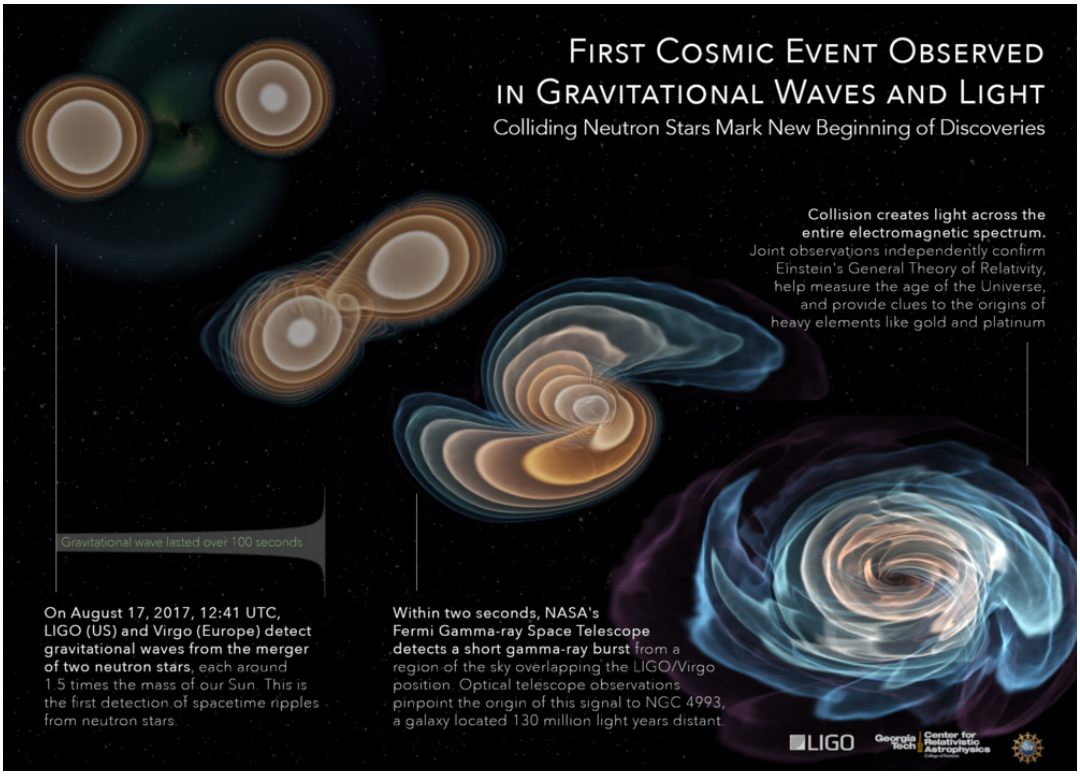

FIGURE 2.4: Gravitational Wave and Light detection from GW170817 (Credit:LIGO, Georgia Tech)

2.2 Lorentz Invariance Violation

Quantum Gravity models (Rovelli, 2004) focus on two central theories nowadays: string theory which tries to explain it from the particle-physics perspective, and Loop Quantum Gravity (LQG), from the GR perspective. The latter one predicts microscopic granular structure and probabilistic dynamics of space-time which can cause foam-like structures at the Planck length (1.62×10^{-35} m). Most of these scenarios predict spontaneous breaking of Lorentz Invariance (LI) (for details, see (Kostelecký and Samuel, 1989) (Gambini and Pullin, 1999) (Douglas and Nekrasov, 2001) (Burgess et al., 2002) (Magueijo and Smolin, 2002) (Hamed et al., 2004) (Horava, 2009)). LIV effects can be observed as vacuum birefringence and dispersion relation for the photons (Kostelecký and Samuel, 1989).

According to vacuum birefringence, the speed of photons in the vacuum depends on their polarization. Recently, some evidence on the vacuum birefringence has been found by the optical light observations of the pulsar RX J1856.5-3754 Mignani et al., 2017.

For this thesis, we will focus on the dispersion relation. LIV can cause energy-dependent dispersion relations of photons in the vacuum, which is predicted to observe these effects at energies at the order of the Planck scale (1.22×10^{19} GeV).

Amelino-Camelia and Smolin, 2009, proposed that the effects of LIV can be potentially measurable for photons of different energies that originated from distant sources, such as astrophysical objects.

The modified dispersion relation (MDR) is formulated as follows ((Amelino-Camelia and Smolin, 2009), Equation 2):

$$m^2 = E^2 - p^2c^2 + \Delta_{QG}(E, p^2; M_{QG}) \tag{2.1}$$

m denotes mass while E and p denote energy and momentum. M_{QG} is the scale of quantum-gravity effects that is expected to be in the order of Planck energy scale. δ_{qg} is the additive term caused by the dispersion. For this thesis we will focus on the photon sector, namely m=0 case. MDR effects in photon sector can be observed in the different forms from the astrophysical sources (see Figure 2.5).

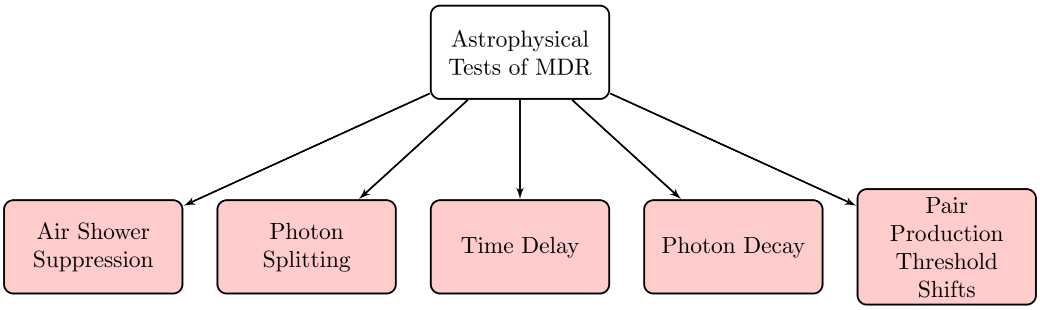

FIGURE 2.5: Current astrophysical tests for Modified Dispersion Relation.

Latest limits derived from the MDR studies in photon sector are shown in Figure 2.6 for the linear and Figure 2.7 for the quadratic cases.

2.2.1 Time of Flight Studies

Time of Flight(ToF) studies focuses on observing the time delays caused by LIV from astrophysical sources. The farthest the astrophysical source, the longer the ToF duration of the photon. As a result, the ToA difference will be more significant. For this purpose, ground-based gamma-ray telescopes are being used. The basic idea of the ToF measurements is comparing the Time of Arrival (ToA) of photons with different energies (see Figure 2.8).

Vasileiou et al., 2013 formalized the MDR for the photons as follows:

$$E^2 \simeq p^2c^2[1 - \sum_{n=1}^{\infty} \zeta_n (\frac{E}{E_{QG_n}})^n] \tag{2.2}$$

where E_{QG_n} represents the energy scale of LIV for the n-th term. ζ_n can be +1 or -1 which corresponds to the subluminal or superluminal scenarios, respectively.

The group velocity of the photons (v_γ) becomes (MAGIC Collaboration et al., 2017):

$$v_\gamma = \frac{\partial E}{\partial p} \approx c[1 - \sum_{n=1}^{\infty} \zeta_n \frac{n+1}{2} (\frac{E}{E_{QG_n}})^n] \tag{2.3}$$

ToF studies focus only on n=1, linear, and n=2 quadratic cases due to the sensitivity of the current ground-based gamma-ray telescopes. The total flight time becomes:

$$t = \frac{\Delta l}{c}[1 + \zeta_1 \frac{E}{E_{QG_1}} + \zeta_2 \frac{3}{2}(\frac{E}{E_{QG_2}})^2] \tag{2.4}$$

Where Δl is the distance. The difference between ToA of photons with different energies can be expressed with Δt:

$$\Delta t_{QG} = \frac{d}{c}\frac{E_h - E_l}{E_{QG_1}} + \frac{d}{c}\frac{3}{2}\frac{E_h^2 - E_l^2}{E_{QG_1^2}} \tag{2.5}$$

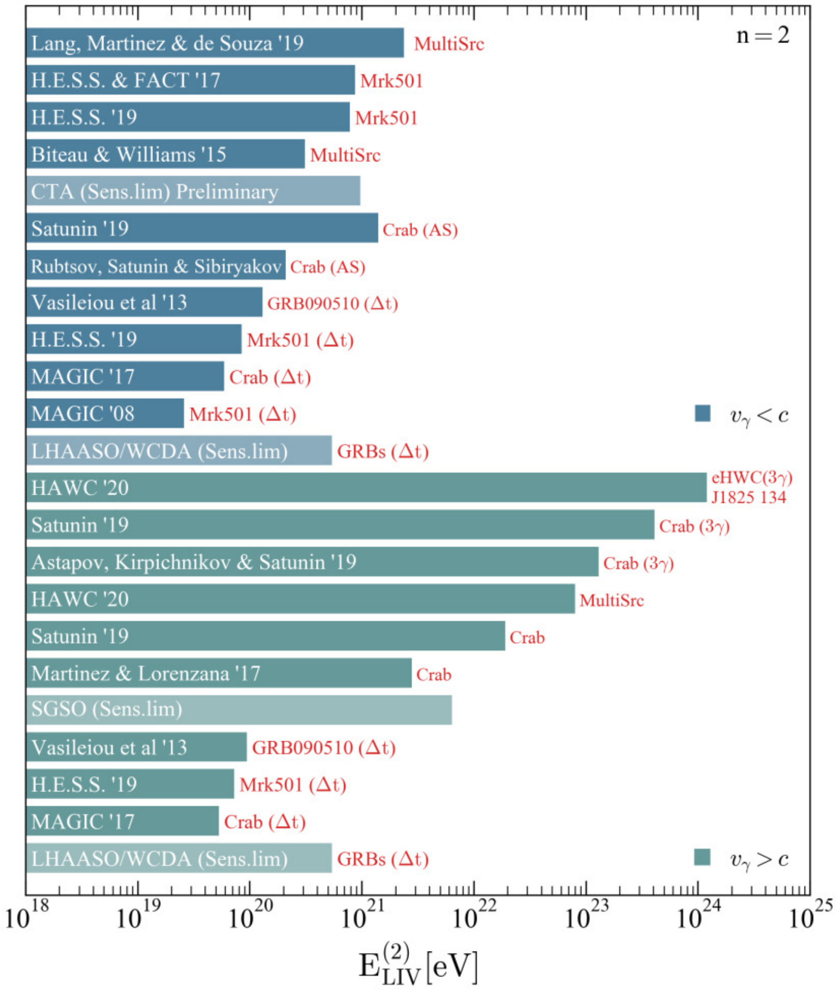

FIGURE 2.6: Recent constraints on the linear case derived from different LIV tests(photon decay, energy-dependent time delay, photon splitting and pair-production threshold shifts). Blue/green show the subluminal/superluminal cases respectively.(Martıénez-Huerta, Lang, and de Souza, 2020)

where E_h and E_l correspond to high and low energetic photons respectively.

The observed difference of the ToA (Δt_{obs}) can be caused by QG effects (Δt_{QG}), cosmological effects for the extragalactic sources ($(1+z)\Delta t_{int}$) and some other effects.

$$\Delta t_{obs} = \Delta t_{QG} + (1+z)\Delta t_{int} + \Delta t_{others} \tag{2.6}$$

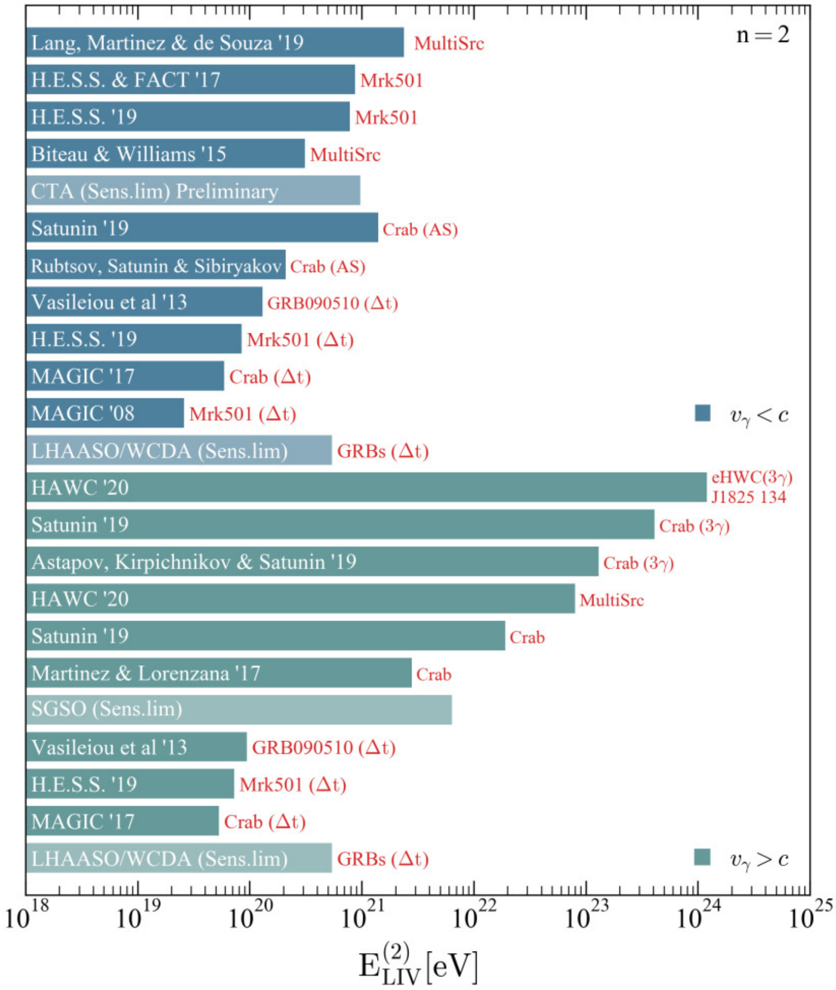

FIGURE 2.7: Recent constraints on the quadratic case derived from different LIV tests(photon decay, energy-dependent time delay, photon splitting and pair-production threshold shifts). Blue/green show the subluminal/superluminal cases respectively.(Martıénez-Huerta, Lang, and de Souza, 2020)

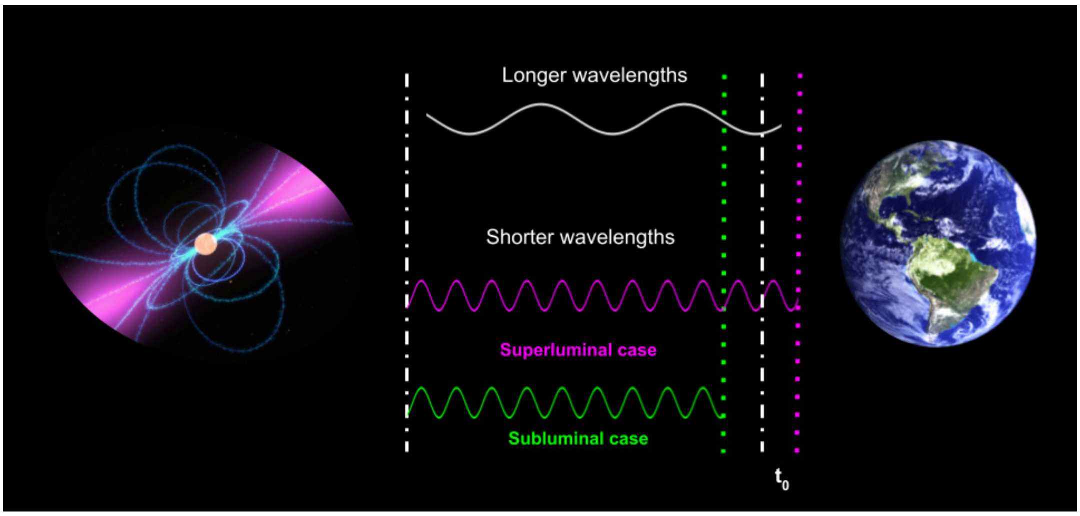

FIGURE 2.8: Illustration of ToA difference observed from the Earth between the longer and the shorter wavelenghts coming from a pulsar due to exposure of the space-time foam like feature in Plank scale.

Pulsar Timing Corrections

Pulsars are galactic sources that are not affected by the cosmological redshift effect that originated from the expansion of the universe. Other physical effects that cause time delays for the pulsar ToA are the following:

$$\Delta t_{others} = \Delta_C + \Delta_E + \Delta_R + \Delta_S + \Delta_{VP} + \Delta_B \tag{2.7}$$

where Δ_C contains various clock corrections of the local observatory clocks. Δ_E represents the Solar system Einstein delay casued by the gravitational potential of the Earth and the Earth's motion. Δ_R is the Solar system Roemer delay which is the ToA difference between the observatory and the solar system barycenter (SSB). Δ_S is the Solar system Shapiro delay caused by the Sun's gravitational potential. Δ_{VP} describes the excess vacuum propagation delay due to secular motion of the pulsar and Shklovskii effect. Finally, Δ_B expresses the time differences caused by the orbital motion of the pulsar in case it is in a binary system. All these timing corrections can be automatically applied by the TEMPO2 package (Hobbs, Edwards, and Manchester, 2006).

After these ToA corrections, the pulsar lightcurves are folded (see Figure 2.9) according to their spin period, and the characteristic light curves are obtained, which will be called phaseograms.

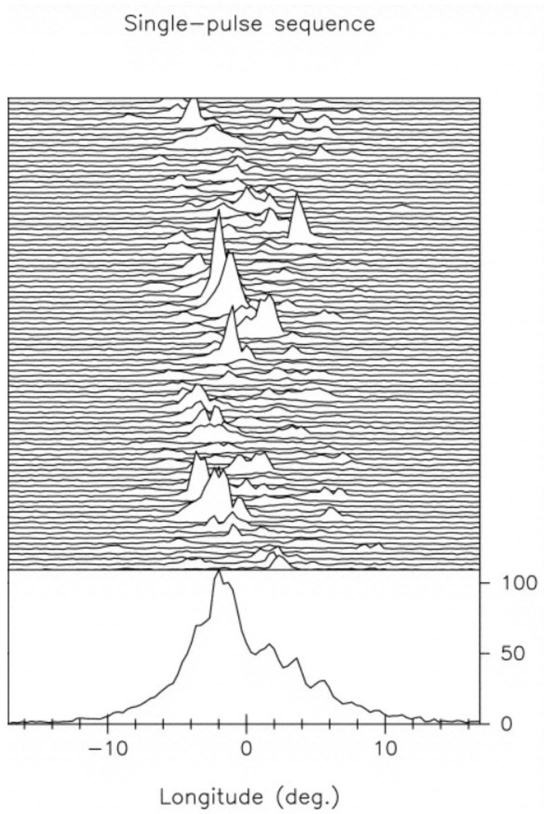

FIGURE 2.9: An example of single pulse folding according to the spin period of the pulsar. (Deshpande and Rankin, 1999)

Time of Flight Methods and the Maximum Likelihood Method

There are various methods for measuring the differences of ToA for the pulsars. The most common and the basic one is the peak comparison method (see Chapter 7), which aims to observe a phase shift for the peak at the pulsar phaseogram due to the energy dispersion. This method is quite simple to apply, but the sensitivity of the analysis is low.

Other widely used unbinned methods are the PairView (Vasileiou et al., 2013), maximization of sharpness , and maximum likelihood methods (Martıénez and Errando, 2009). For this thesis, we are going to focus on the Maximum Likelihood Method (MLM) that will be explained in more detail in Chapter 7.

Time of Flight target sources for Maximum Likelihood Method and the derived limits

ToF studies are performed with gamma-ray experiments, including the satellite Fermi-LAT and the ground based Cherenkov Telescopes: MAGIC, H.E.S.S, and VERITAS. Here are the astrophysical targets used for the ToF LIV tests:

- **Active Galactic Nuclei (AGN):** AGNs are far away sources. They have quiescence and flare periods which may last from days to weeks. They can emit VHE gamma-rays up to hundreds of TeV. Their flux levels increase more than one order of magnitude during the flare period.

- **Gamma-Ray Burst (GRBs):** GRB sources are extragalactic sources as AGNs. Similar to the AGN flares, GRB bursts can reach tens of TeVs with a significant magnitude change in their flux levels. Their bursts are shorter, which may vary from seconds to minutes.

- **Pulsars:** Pulsars are the closest objects compared to the AGNs and GRBs, which makes them disadvantageous due to the shorter time-of-flight duration. However, their predictable flux changes due to pulsations and sharp timing features make them a steady source for these kind of studies. The sensitivity of the tests increases with the amount of data, which makes them advantageous compared to the unpredictable flare and burst periods of AGNs and GRBs.

Chapter 3

Introduction to IACTs and the MAGIC Telescopes

Gamma-ray astronomy is the study of the universe through the most energetic electromagnetic messengers. This field is relatively new compared to the other branches of astronomy as radio or optical. Different detection techniques such as balloon or rocket experiments were used to observe gamma-rays in the past. Nowadays, satellites and ground-based telescopes are developing more and more and providing us with stunning information about cosmic gamma-rays. The data used for this thesis were collected by the MAGIC Telescopes, one of these ground-based gamma-ray facilities.

In this chapter, firstly, gamma-ray detection techniques and the principles of ground-based Imaging Atmospheric Cherenkov Telescopes (IACTs) will be explained. Afterward, the properties of the MAGIC Telescopes and analysis chain will be discussed. Finally, the next-generation IACT array,the Cherenkov Telescope Array (CTA), will be introduced.

3.1 Gamma-ray Astronomy

Gamma-rays are the most energetic photons of the electromagnetic spectrum. The definition of the gamma-ray photons in this thesis will be grouped as in Table 3.1.

Low Energy (LE)	0.1 MeV - 10 MeV
High Energy (HE)	10 MeV - 10 GeV
Very High Energy (VHE)	10 GeV - 10 TeV
Ultra High Energy (UHE)	10 TeV - 10 PeV
Extremely High Energy (EHE)	10 PeV - no limit

TABLE 3.1: Table of Gamma-ray energy ranges defined for this thesis

The astrophysical gamma-ray sources can be either within our galaxy (galactic sources) or out of our galaxy (extragalactic sources). One of the typical galactic gamma-ray sources is pulsars. As explained in Chapter 1, pulsars can emit HE and VHE gamma-ray photons due to the accelerated ultra-relativistic particles in their magnetosphere. Additionally, gamma-rays can also be produced in supernova remnants or via Pulsar Wind Nebula (PWNe), which accelerate particles to relativistic speeds through shock waves. Two of the most well-known gamma-ray sources are the Crab Pulsar and the Crab Nebula. Gamma-rays are also observed from some gamma-ray binary systems interacting with their companion star.

Additionally, some of the extremely powerful extragalactic astrophysical sources can generate gamma-rays, too. AGNs are one of the extragalactic gamma-ray sources that galaxies with Supermassive Black Holes in their centers, that can accelerate particles to ultra-relativistic speeds through their jets (see Figure 5.14). The other most common extragalactic sources are GRBs, which are the powerful mergers of compact objects in binary systems like black holes or pulsars.

3.2 Astrophysical Gamma-ray Detection Techniques

The atmosphere is not transparent to all wavelengths. Although the radio and visible bands are transparent for the ground-based observations, it is opaque for the HE like gamma-rays (see Figure 3.1). Gamma-rays can travel in the atmosphere without interacting down to 40km altitude from the sea level (for more details on the atmospheric structure, see the Chapter 4)

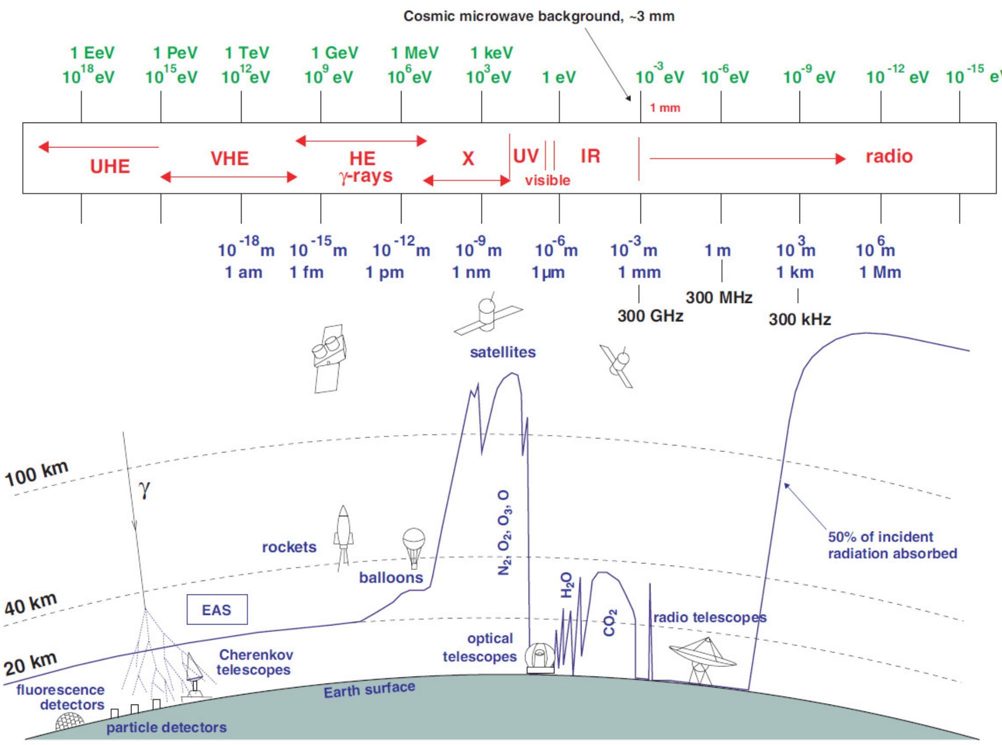

FIGURE 3.1: The electromagnetic spectrum and the transparency of the atmosphere for the photons and the corresponding detection techniques.(Adapted from (Longair, 1992), Credit: Abelardo Moralejo

Nowadays, two main groups of systems are used to detect gamma-rays: satellites and ground-based systems.

3.2.1 Satellites

Some of the well-known early-stage gamma-ray satellites were Explorer XI (Kraushaar et al., 1965), CosB (Bignami et al., 1975), and SAS-2 (Thompson et al., 1974). These were followed by the next-generation satellites, EGRET (30 MeV - 30 GeV) (Fichtel et al., 1993) (1991-2000); and Fermi-LAT (20 MeV - 300 GeV) (Atwood et al., 2009) (active since 2008). Although the structures of EGRET and Fermi-LAT are not identical, their working principle is similar. They focus on determining the arrival direction and energy of the events by a detector on the satellite using the pair production of the gamma-ray (see Figure 3.2).

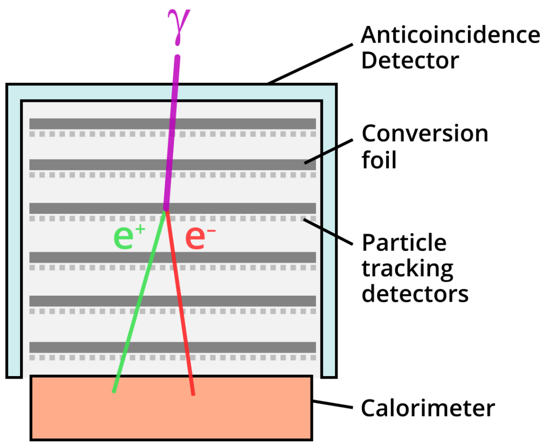

FIGURE 3.2: The sketch of the Fermi-LAT detector (Credit: Fermi-LAT). After a HE gamma-ray enters the detector, electron-positron pair production occurs with the help of conversion foils. Those particles are tracked through the particle detectors; this way, the location of the source can be estimated. Finally, the particles reach the calorimeter, where the energy of the gamma-ray source can be determined.

3.2.2 Ground-based systems

Ground-based systems cannot directly detect gamma-rays like satellites due to the opacity of the atmosphere. With the discovery of cosmic-rays (Hess, 1912), balloon and rocket experiments started in the 1910s to understand their nature. It was a discussion whether the cosmic-rays are photonic originated (Millikan and Cameron, 1928) or positively charged particles as claimed by Compton (E. Lorenz and Wagner, 2012).

Today, it is known that the Earth is bombarded by both the charged particles and the photons of cosmic origin, called gamma-rays and cosmic-rays, respectively. Although both the cosmic and gamma-rays come from astrophysical sources, we can only determine the gamma-ray sources. At the same time, the origin information is lost for the cosmic-rays because of the magnetic fields deflecting the charged particles and randomizing their direction. When the gamma-rays and the cosmic-rays enter the atmosphere, they trigger interaction and production of many particles and create a cascade, called Extensive Air Shower (EAS) (Auger et al., 1939). The photon and charged particle-originated showers have different characteristics and are called electromagnetic and hadronic showers (see Figure 3.3), respectively.

Meanwhile, Cherenkov radiation (Čerenkov, 1937) was discovered, characteristic ultraviolet radiation produced while relativistic cosmic particles are traveling through a medium such as the atmosphere, water, and ice. It was also discovered that Cherenkov radiation can be formed by EAS where the charged particles travel at ultra-relativistic speeds (Blackett, 1948). In light of this information, there are two main types of ground-based detection systems today. Detecting the charged

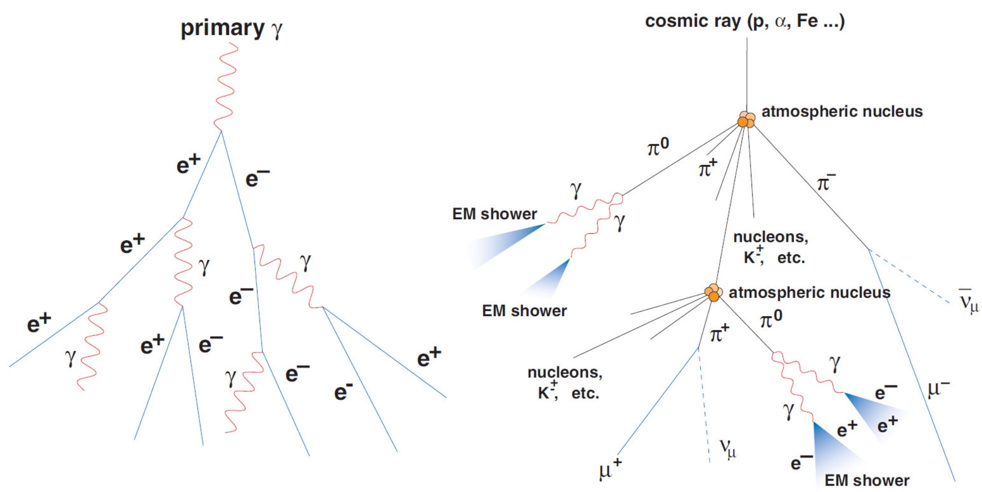

FIGURE 3.3: Extensive Air Showers in the atmosphere. Electromagnetic shower generated primary gamma-ray can be seen on the left, a cascade of electron-positron and photons. A hadronic shower is shown on the right, which is originated by a hadronic particle (proton or nucleus), a cascade of many secondary particles.

particles produced during the EAS cascades (tail-catcher detectors) and mirrored telescope systems focusing on detecting the Cherenkov light produced during the electromagnetic and hadronic EAS showers (IACTs). We will focus on the IACTs for this thesis.

3.3 Imaging Atmospheric Cherenkov Telescopes

IACTs have arrived at this day with significant improvements and developments. Although the experiments started well before 1990s, the first-generation systems did not succeed in detecting gamma-rays until that date because of several issues (E. Lorenz and Wagner, 2012). Firstly, only 10^{-4} fraction of the total EAS shower is converted into Cherenkov photons, and atmospheric scatterings cause even more loss. Additionally, the first-generation systems were not able to discriminate the gamma-rays compared to the hadronic background. Lastly, the photodetectors were not sufficient enough for detecting weak Cherenkov lights. Afterward, some of the problems were solved for the second-generation systems such as Whipple and HEGRA by using a pixelized camera, which helped distinguish gammas and hadrons more successfully.

Third-generation systems are the current IACT systems: the MAGIC Telescopes, H.E.S.S, and Veritas. They are defined as IACT systems (see Figure 3.4) that can detect <1% flux of the Crab Nebula in 50h with 5 σ. They use Photo Multiplier Tubes (PMTs), which help to detect fast Cherenkov flashes. Some of them have parabolic mirrors to pixelate the images on the camera by which the reflected Cherenkov light can be parametrized to understand the physical properties of the shower (Hillas, 1985) (see Figure 3.13).

Calibration of the ground-based detectors is more challenging in contrast to the HE particle detectors that are calibrated via test beams with known energy, direction, and timing. Various methods are used for the calibration, such as F-factor for the camera, muon rings for absolute calibration, the standard candle for higher-level

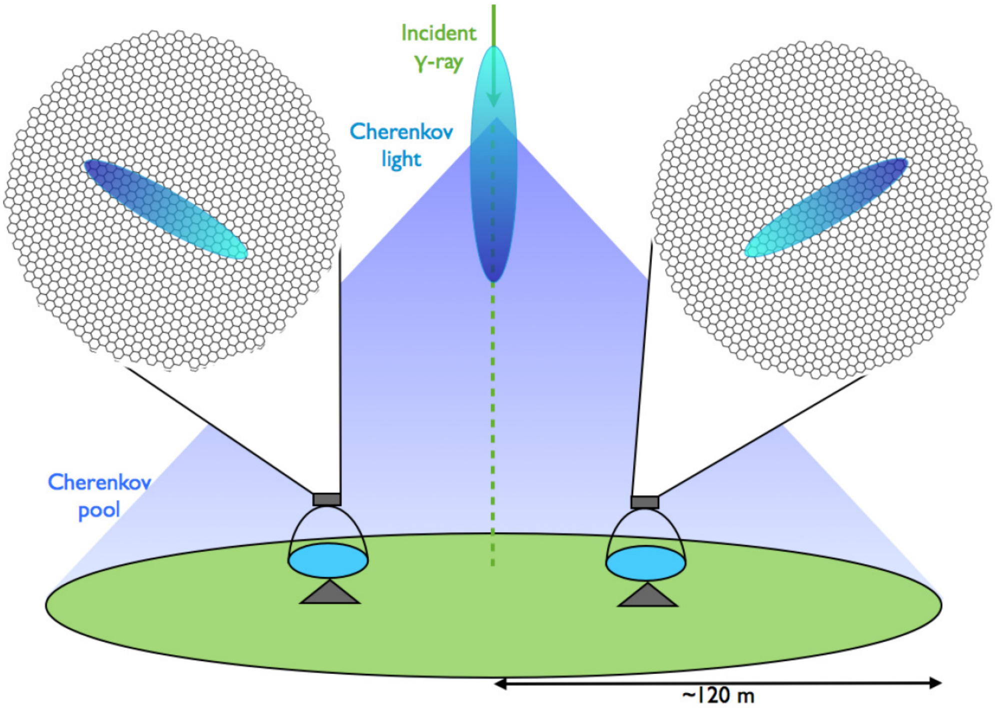

FIGURE 3.4: Sketch of IACTs, (Credit Ruben Lopez(2015)).

(Sanity) checks. In addition to the calibration, Monte Carlo simulations are needed for distinguishing the electromagnetic and hadronic showers (see Figure 3.5).

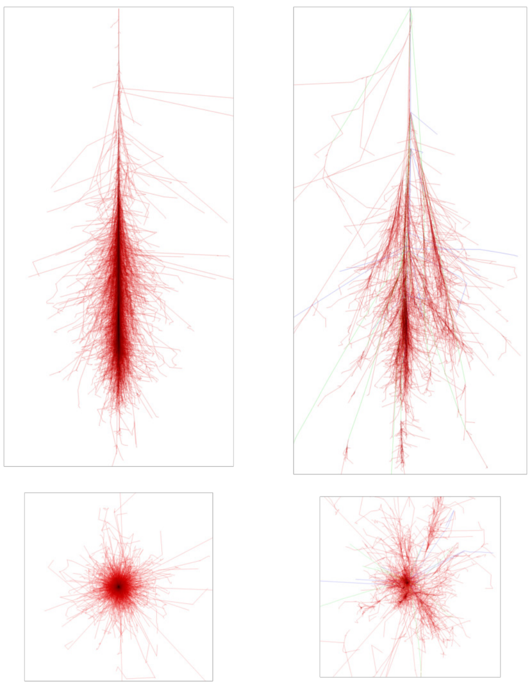

FIGURE 3.5: Monte Carlo simulations for 100 GeV events left: electromagnetic shower triggered by a gamma, right: hadronic shower triggered by a cosmic particle. (Credit: Johannes Knapp)

3.4 The MAGIC Telescopes

The "Florian Goebel" Major Atmospheric Gamma-ray Imaging Cherenkov (MAGIC) Telescopes are a system of two 17m-diameter IACT (Eckart Lorenz, 2004). Telescopes located at Roque de Los Muchachos Observatory on the Canary Island of La Palma, Spain, at an altitude 2220m above sea level (see Figure 3.6)). They have been designed to observe VHE gamma-rays from tens of GeV to hundreds of TeV. Their light structure allows quick response for transient events such as Gamma-Ray Bursts (GRBs) and other transient events. The drive system has a fast repositioning mode that allows rotating the telescope 180 degrees in less than 20s.

FIGURE 3.6: The MAGIC site consists of two IACTs, MAGIC-I and MAGIC-II, and an operation house with MAGIC LIDAR on the top.

The MAGIC Telescopes consist of two identical telescopes MAGIC-I and MAGIC-II (Figure 3.6), which have been operating together in stereoscopic mode since 2011. Previously, MAGIC-I operated as a standalone telescope in 2004-2009 (mono mode). Afterward, the commissioning of clone telescope MAGIC-II held 2009-2011, which is called the pre-upgrade period. During this period, both of the telescopes had some hardware changes to improve the systems and make them identical (see Table 3.2). The details of the hardware components will be explained in the following subsection.

Years	Status of the Telescopes	Specifications
2009-2011	MI - MAGIC-II Pre-Upgrade First Stereo data, MAGIC-II still on commissioning.	Dead time is 500 microseconds MAGIC-I operating with 4NN triggers
2011-2012	MI- MAGIC-II Upgrade Stereo data after first hardware upgrades	Dead time is 26 microseconds change of MAGIC-I and MAGIC-II redout systems Change of PSF
2012-	MI- MAGIC-II Post Upgrade First stereo data after hardware upgrades	Dead time is 26 microseconds Change of Camera MI

TABLE 3.2: Table of upgrade periods of the stereoscopic MAGIC system

In addition to the MAGIC Telescopes, there is an operation building on the MAGIC site called Counting House, where all the electronic devices are stored for signal processing and storage. Additionally, the telescopes are operated from this building. There is a telescopic laser system on the rooftop of the Counting House, called

MAGIC LIDAR (see Chapter 4), in addition to a weather station for checking the optimal weather conditions for the operations.

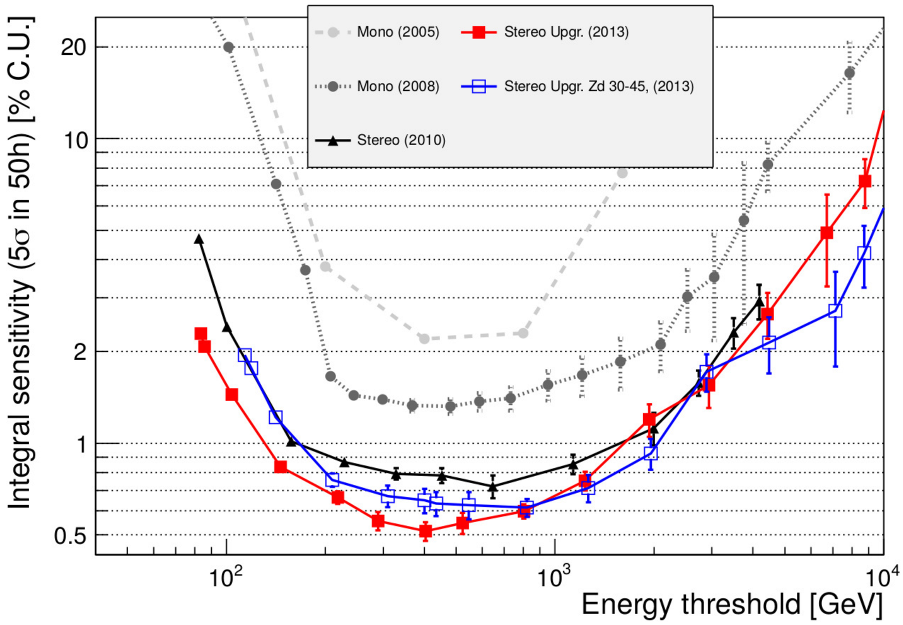

FIGURE 3.7: The sensitivity of the MAGIC Telescopes (Aleksić et al., 2016). The integral sensitivity has been improved by switching to the stereo configuration with two telescopes.

3.4.1 Technical Description

Mount

The MAGIC Telescopes have been designed with an identical light structure in order to allow fast re-pointing for follow-up of transient phenomena that require rapid response. They can point towards any direction above the horizon in less than 40 seconds in normal mode and less than 20 seconds in alarm mode. Carbon fiber-epoxy tubes are connected with aluminum knots, so the system is both light and rigid. The part that holds the reflector is called frame and is 60 tons in total, and 72 tons with all the components (Bretz et al., 2009). An arch system has been designed to locate the 0.75 tons camera at approximately 17m focal length from the reflector and fixed by thin steel cables to the main dish frame. The deformation of the mounting is less than 3.5mm, and the possible effects on the image are corrected by an automatic mirror reorientation system - Active Mirror Control (AMC).

Drive

Driving each telescope is powered by two servo motors for azimuth and one servo motor for elevation by which telescopes can move between -90 to 318 degrees in azimuth and -10 to 160 degrees zenith in height. Three absolute 14-bit shaft encoders continuously cross-check the position of each telescope, and the mechanical pointing accuracy of the system is better than 1 degree (1/5 of the pixel diameter). Furthermore, the telescope's pointing precision is monitored by a system called Starguider, which allows further offline correction of mispositioning via software. The Starguider system consists of a 4.6 field of view (FoV) CCD camera mounted close to the center of the reflector, which observes the camera of the telescope during the operations. It determines the exact pointing position by comparing the bright reference stars, guide stars on the catalogs, and the LED light indicators placed on the telescope's camera. This estimation depends on the atmospheric conditions. Therefore the number of the observed and expected stars in the catalog are monitored during the observations.

Mirrors

The reflecting surface is placed on a 17m diameter octagonal parabolic shape dish. MAGIC-I reflector consists of 956 aluminum mirrors of $0.5 \times 0.5m^2$ grouped in panels of four facets. MAGIC-II reflector, on the other hand, is composed of $1m^2$ of 143 aluminum mirrors (placed in the inner region) and 104 glass mirrors (in the outer region). The surface of each mirror is coated with a 100 nm thick layer of quartz to protect them from corrosion and external agents. Focal length is the same as the diameter, making the focal-to-diameter ratio one.

Camera - Calibration

The light collected by the reflector is focused on the camera, and the detected photons are amplified by photomultiplier tubes (PMTs). PMTs have high quantum efficiency (QE), fast response, high gain, and are small enough to build finely pixelized cameras. Each PMT is equipped with a hexagonal light collector (Winston cone) that prevents contamination by environmental light not arriving from the mirror. A transparent plexiglass window protects the camera and together with two lids that are only open during the observations. The camera is protected with cooling and heating systems to prevent high temperature and humidity.

During the standalone period (mono mode), the camera of the MAGIC-I telescope (see Figure 3.8) was hexagonal in shape with a FoV 3.6-degree diameter. It was equipped with two types of PMTs which were placed on the inner and outer zone. The interior zone consisted of 397 PMTs with 30 mm diameter and 0.1 FoV each. This zone was used as the trigger area. The outer zone, on the other hand, consisted of 180 PMTs with a diameter of 60 mm and 0.2 FoV.

The camera of the MAGIC-I telescope was upgraded in 2009-2011, and currently, both MAGIC-I and MAGIC-II have identical cameras (see Figure 3.8). The cameras have a circular shape with a FoV 3.5-degree diameter. Each camera consist of 1039 identical PMTs with a diameter of 30 mm and 0.1-degree FoV. The standard trigger area is located at the innermost 2.5-degree diameter zone. The PMTs are grouped into 169 independent clusters for monitoring the triggers. The system is flat-fielded and calibrated with a Q-switched Nd-YAG laser located at the center of the telescope reflector.

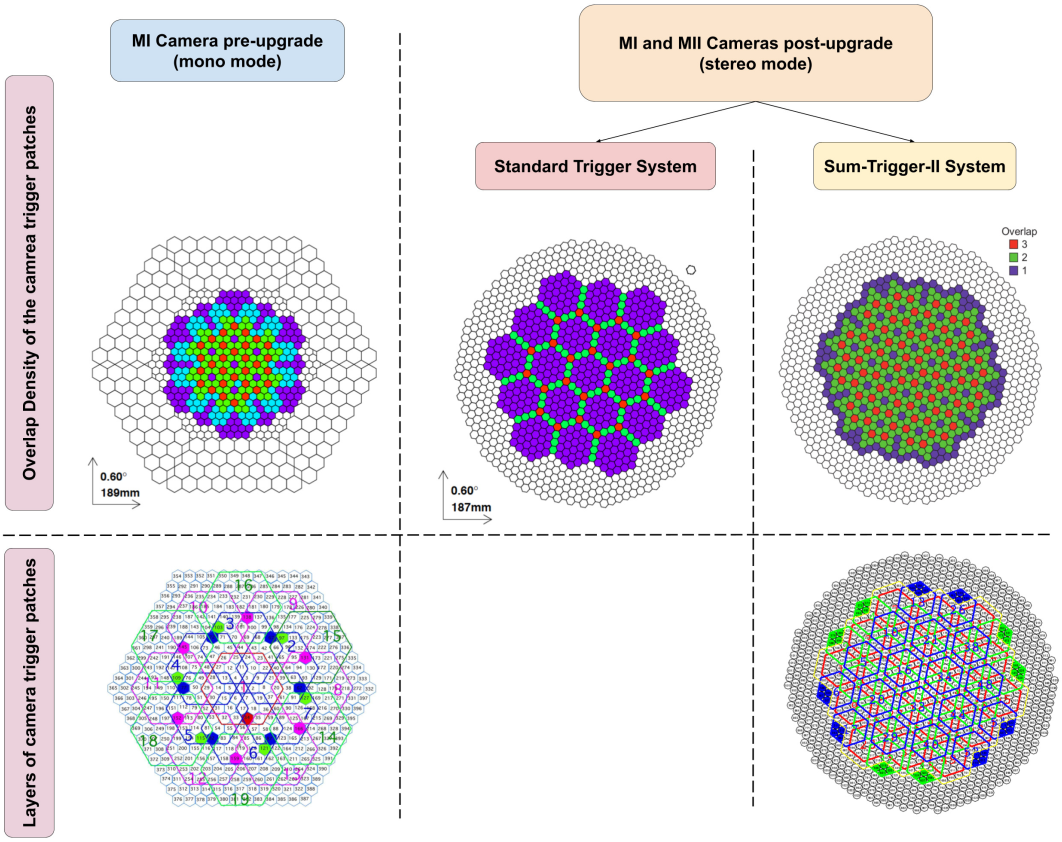

FIGURE 3.8: Cameras of the MAGIC Telescopes and the trigger areas adapted from (Aleksic, 2015) (Dazzi et al., 2021) (Gaug, 2006). The left panel shows the old MAGIC-I camera used during the standalone (mono mode) period, and the right panel shows the MAGIC-I and MAGIC-II cameras after the upgrade. The colors indicate trigger areas with different photoelectron levels. The cyan hexagons (36 pixels each) show the 19 L1 trigger macrocells. Pixels that are covered by more than one macrocell are shown in green (single overlap) or red (double overlap).

Readout

As mentioned previously, the Cherenkov photons are converted into electrical pulses in PMTs. The electrical signal is amplified and converted into an optical signal by vertical cavity surface emitting laser diodes (VCSELs) located at the base of each PMT. These analog optical signals are transferred to the Counting House for further signal processes through 162 m optical fiber. By this conversion method of electromagnetic to optical, the signals are not affected by the electromagnetic noise during the transmission and the loss of the signal is minimized. The optical signals are converted back to electrical pulses on receiver cards and split into two branches through fast GaAs PIN diodes. One of the branches enters the trigger system and the other switches to the data acquisition system (DAQ). When the trigger strikes, sampling stops, and the digitized signal is recorded in the raw data file. DAQ digitizes electrical pulses using Analog to Digital Converters (ADCs). The simple working principle is shown in Figure 3.9.

Before the upgrade, MAGIC-I standalone system was using a digitization system of DRS2 waveform digitizer, and after the upgrade, currently, DRS4 digitizer is being

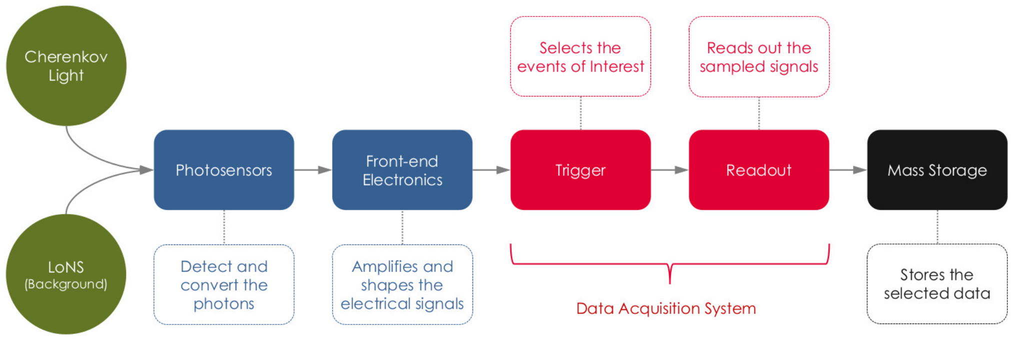

FIGURE 3.9: The working principle of the IACTs (Dazzi et al., 2021). Green circles represent the radiation captured by an IACT. Filled blocks represent the main components of an IACT electronic chain, where the component functions are shown in unfilled blocks.

used (Sitarek et al., 2013), which decreased loss of observation time due to process speed from about %12 to a negligible fraction.

Standard Trigger System

The most important aim of the trigger system is discriminating the Cherenkov shower from the Night Sky Background (NSB). The Cherenkov shower light is characterized by fast pulses (< 5 ns) and recorded by neighboring pixels simultaneously. The standard trigger system of the MAGIC Telescopes has four trigger levels. The first three levels are processed by individual telescopes, and the last level is shared with both systems (see Figure 3.10).

- **Level 0 (L0):** hosted on the receiver boards, it evaluates every channel individually and issues a trigger only if it exceeds a certain amplitude – the discriminator threshold (DT). DTs are programmable by software.
- **Level 1 (L1):** L0 signals are sent to L1, which examines the channels in search for spatial and temporal correlation over the decomposition of the trigger region in 19 overlapping macrocells. This topological condition is based on the close compact next neighbor (CCNN) logic; the L1 trigger accepts only events present in N adjacent pixels. The standard CCNN setup applied in MAGIC observations is that of 4NN.
- **Level 2 (L2):** The events triggered by L1 enter to L2 for further, shape-based monitoring. L2 does not discriminate events, but its units are used for event rate monitoring, rate scaling, and integration of L1, calibration, and stereo triggers.
- **Level 3 (L3 - Stereo trigger):** selects only those events that have triggered both telescopes individually within a specific time interval. In order to minimize the coincidence time window, the arrival times of L1 triggers of each telescope are delayed, depending on the pointing direction of the telescopes.

Sum-Trigger-II System

In addition to the standard trigger system, another trigger system is actively used by the MAGIC Telescopes called the Sum-Trigger-II system. This system aims to

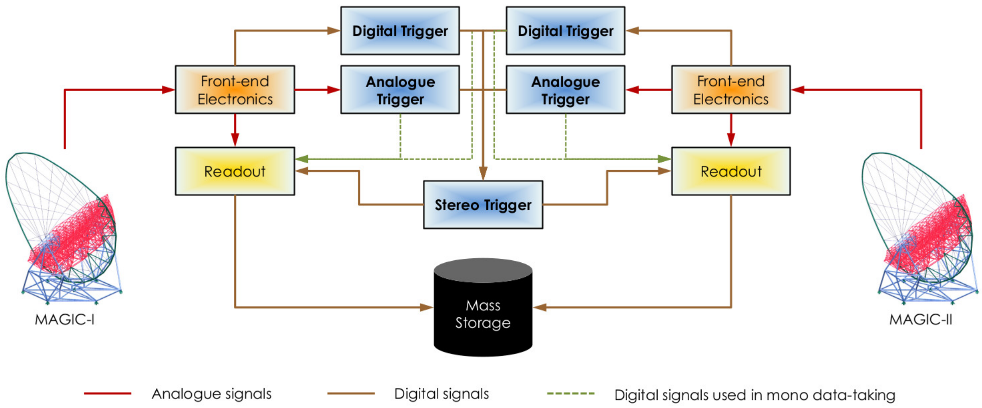

FIGURE 3.10: The context of the stereoscopic trigger systems of the MAGIC telescopes (Dazzi et al., 2021). Digital trigger system is used by the Standard Trigger System while the analog trigger system is used by the Sum-Trigger-II system which operates separately.

increase the sensitivity of the observations in the sub-100GeV region. For the lower energies, the smaller sizes of the Cherenkov showers make it harder to distinguish the events from the NSB. Therefore instead of applying a trigger threshold to the signals with a digital trigger system, the signals are added by an analogue trigger system and then a discrimination threshold is applied(see Figures 3.11 , 3.10).

Signals enter the Clip-Boards, where the necessary delay, amplitude adjustment, and clipping are applied. They are then moved to the Sum-Backplane, where the signals are propagated over the backplane. Afterward, signals are physically summed up in Sum-Board, and these signals are discriminated with a threshold. The digitized signal propagates over the Sum-Backplane again and finally connected to L3.

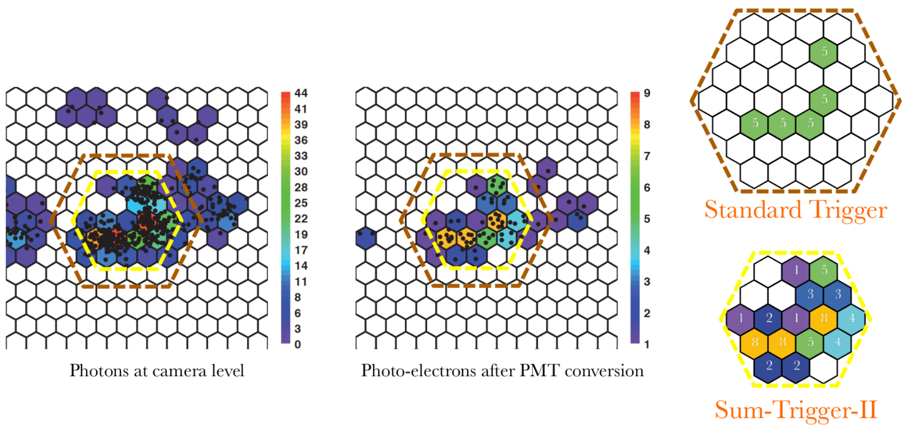

FIGURE 3.11: Simulated signal produced by a 31.8 GeV gamma-ray shower in one of the MAGIC cameras (Dazzi et al., 2015). The left panel shows the photons at the camera level with black dots. The middle panel shows the photo-electrons after PMT conversion, where only around 20 % of the entire photon population is converted in photo-electrons and processed by the trigger system. On the right, a comparison of the standard trigger and Sum-Trigger-II response to the same event.

The third gamma-ray pulsar, Geminga, was discovered by this system (MAGIC Collaboration et al., 2020). Additionally, it is worth to mention that, there was a Sum-Trigger system in the past which was only used by one telescope MAGIC-I and led to the first detection of the Crab Pulsar above 25GeV (Aliu et al., 2008).

3.4.2 MAGIC Data Analysis Chain

MAGIC Data analysis is performed by a ROOT-based package called MARS(MAGIC Analysis and Reconstruction Software) (Zanin et al., 2013) which is written in C++. The analysis can be grouped into three main levels: low-level, medium-level, and high-level analysis. The sub-programs of MARS and their order is shown in Figure 3.14.

Low-level Process

The observation data is recorded in RAW format for each of the telescopes independently during the observation. The data size is about 100 GB per telescope per hour of observation and reduced by a factor of about 200 with analysis.Here are the data types recorded by the MAGIC telescopes:

1. **Pedestal Run:** Firstly, pedestal events are recorded during an observation. These randomly triggered events are used for estimating the background level caused by NSB and the electronic noise and subtracted during the data calibration.

2. **Calibration Run:** Secondly, the calibration events are recorded, which are fast pulses similar to Cherenkov pulses. These events are later used for the calibration of the data for converting the stored charged values into phe.

3. **Data Run:** Lastly, the data events are recorded.

Transferring this large-size raw data from La Palma through a network connection takes time. Therefore, the low-level standard analysis is performed at MAGIC-site (called On-Site Analysis (OSA)) and transferred by internet to the data center at the Port d'Informació Científica (PIC) in Barcelona. Some non-standard analysis, such as Sum-Trigger-II analysis (MaTaJu cleaning), has to start from the low-level and needed to be done by the analyzer.

The low level-analysis aims to do the following steps by using the corresponding MARS programs shown in Figure 3.14.

- **Merpp:** RAW data is converted to root format. It organizes the parameters of events in root tree format. Meanwhile, telescope reports are also embedded in trees, such as technical details and weather conditions.

- **Sorcerer:** With this program, signal extraction and calibration of the received signals is performed for each telescope independently by using Pedestal and Calibration runs. The recorded digital counts are converted to phe with respect to the number of Cherenkov photons recorded in each pixel. The sliding time window used for the calibration is different for the DSR2 and DSR4 systems. Additionally, the data recorded by the Standard trigger and Sum-Trigger-II are analyzed differently in this level. For the Sum-Trigger-II data, the MaTaJu cleaning has an additional step which is spike removal. The spikes recorded with the signals are excluded from performing a linear interpolation algorithm.

- **Star:** With this program, image cleaning and the parametrization of the recorded showers are performed for each telescope independently. The aim of the image cleaning Figure 3.12 is to keep the triggered pixels from the showers and removing the rest of the useless pixel information, which helps to reduce the data size. The remaining pixels are fitted with an ellipse, and the Hillas parameters (Figure 3.13) are derived for distinguishing the gamma-ray shower from the hadronic shower and the muon showers, as well as estimating the energy and direction of the events. An additional step is performed at this level for the MaTaJu cleaning. If there are bright visible stars in the FoV which have magnitude<6, the exposed pixels have to be excluded in this level.

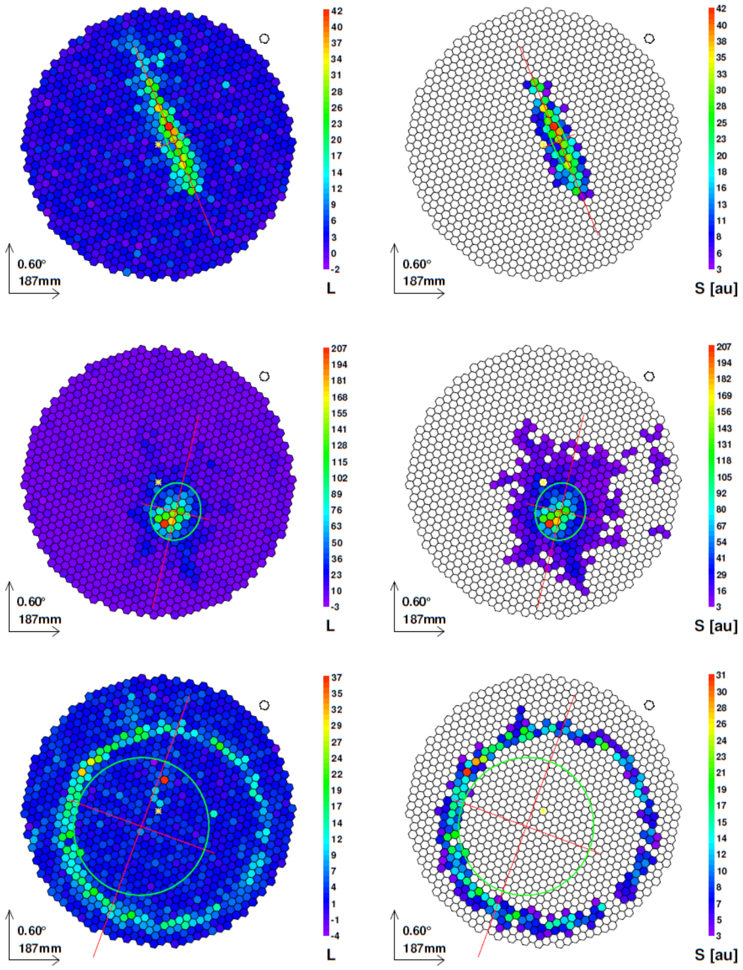

FIGURE 3.12: Left panels show the recorded events before the cleaning, and the right panels show after the cleaning. The top two images are the gamma-like events, the middle images are the hadron-like events, and the bottom images are muon-like events. (Aleksic, 2015)

Medium-level Process

The analyzers start the analysis chain of MAGIC from medium-level, which aims to combine the information of the two telescopes and characterize the recorded events.

Some non-standard analysis such as MaTaJu cleaning has to be performed by the analyzer starting from the low-level as mentioned in the previous section.

- **SuperStar:** This program aims to merge the simultaneous images recorded by the two telescopes separately(see Figure 3.4. In the meantime, some stereo parameters are estimated, which will be used to estimate the energy and the direction of the showers. This program is also run automatically by OSA for the Standard Analysis but has to be performed by the analyzer for the non-standard analysis such as MaTaJu cleaning.

- **Coach:** This program aims to classify the events as gamma-like or hadron-like events and calculate a probability for the events. This probability is named "hadronness", distributed between 0 to 1. For this purpose, Random Forest (RF) (Albert et al., 2008a) method is used, which compares the hadron-like dominated events with gamma MC simulations. In order to supply the hadron-like dominated events, other observational superstar data are used, which do not include any detected sources. These observational data have to be selected similar to the recorded target data, such as the trigger systems used, the Zenith Distance of the telescope, and especially in the same observation period in which the telescope performance is similar. Namely, this program has to be run for the different MC periods (see Table 3.3 for the MC periods used in this thesis). Additionally, so-called "look-up" tables are built with this program, which will be used for energy reconstruction.

- **Melibea:** With this program, events in the SuperStar level are characterized by using the look-up tables and hadronness information prepared by Coach. As a result, the estimated energy, and the direction are assigned for each event.

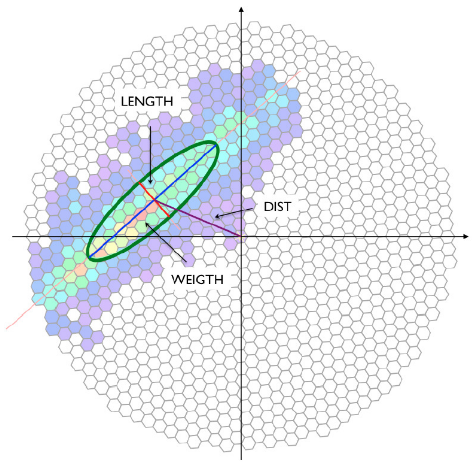

FIGURE 3.13: Illustration of the Hillas parametrization such as length, width, and distance (Aleksic, 2015). The length and the weight parameters are closely related to the energy of the gamma-like events. And the distance parameter is used to determine the location of the image relative to the camera center.

Observation Periods	**Dates**	**Specifications**
ST.01.02	2009-09-01 - 2009-11-01	MAGIC-I - MAGIC-II Pre-Upgrade
ST.01.02	2009-11-01 - 2011-06-01	Stereo data (stable system)
ST.02.01	2012-01-19 - 2012-02-25	MI- MAGIC-II Upgrade
ST.02.02	2012-02-26 - 2012-03-09	Stereo data after first hardware upgrades
ST.02.03	2012-03-10 - 2012-05-21	Stereo data after first hardware upgrades. Change of PSF
M2.02.04	2012-05-21 - 2012-06-19	MAGIC-II mono data
ST.03.01	2012.09.01 - 2013.01.17	MI- MAGIC-II Post Upgrade
ST.03.02	2013.01.18 - 2013.07.26	Stereo data after hardware upgrades with new LUTs applied in M1 AMC in 2013-01-17
ST.03.03	2013.07.27 - 2014-06-18 2014-07-05 - 2014-08-05	Stereo data after hardware upgrades with new LUTs applied in M1 AMC in 2013-07-26
M2.03.04	2014-06-19 - 2014-07-04	MAGIC-II mono
ST.03.04	2014.08.27 - 2014-08-30	Stereo data after mirror exchange, but before final AMC adjustment (pretty bad PSF!)
ST.03.05	2014.08.31 - 2014.11.22	Stereo data after mirror exchange and AMC adjustment
ST.03.06	2014.11.24 - 2016.04.28	Data after change of sampling to 1.64GHz
ST.03.07	2016.04.29 - 2017.08.02	Data after PSF improvement in spring 2016
ST.03.08	2017.08.02 - 2017.11.02	Data affected by dust-related drop in reflectivity
ST.03.09	2017.11.10 - 2018.06.29	Data affected by rain cleaned the dust from the mirrors
ST.03.10	2018.06.30 - 2018.10.30	Data affected by worse mirror reflectivity
ST.03.11	2018.11.01 - 2019.09.15	Data with recovered reflectivity
ST.03.12	2019.09.16 - 2020.02.22	Data with worse PSF

TABLE 3.3: Observation Periods of the MAGIC Telescopes

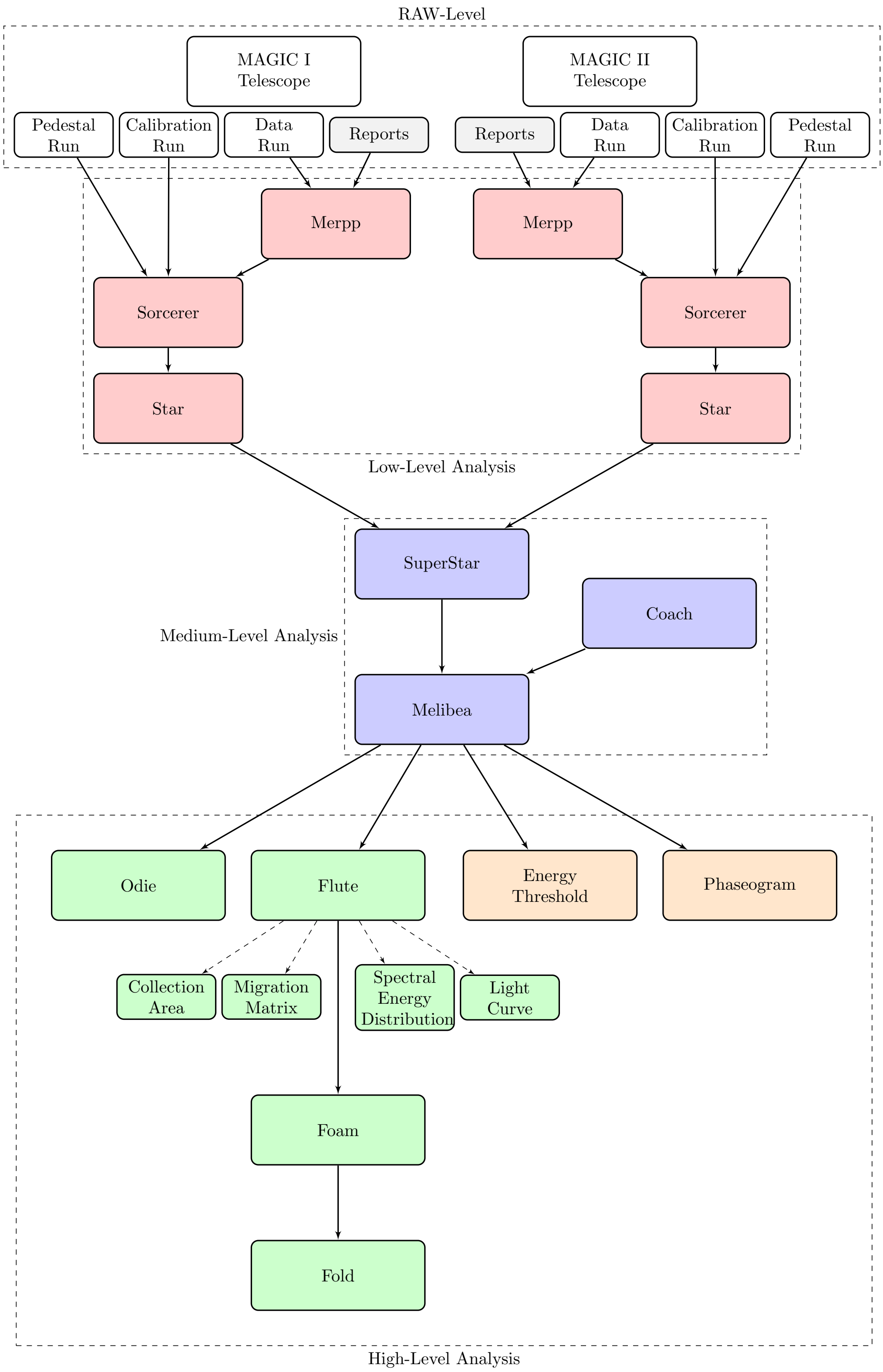

FIGURE 3.14: MAGIC Analysis Chain adapted from (Zanin et al., 2013). The data is collected in RAW format (shown as RAW-level). Then low-level, medium-level, and high-level analyses are performed with the order. Higher-order outputs can be increased (such as the yellow ones) with custom root-based C++ codes.

High-level Process

At this level, the scientific outputs of the data are created.

- **Odie:** This program calculates the significance of the signal. For this purpose, so-called *Theta*^{2} histograms are used (see Figure 3.15). Theta represents the angular distance between each event, and the source position. The signal region (ON) is decided with specific angular distance values, and the number of events collected in this region is called ON events. Moreover, the background region (OFF) is defined by the mirror position of the source relative to the camera center by using the same angular distance radiuses. The number of OFF regions (α=1/number of OFF regions) can be increased, and the number of excess events are calculated by the following formula:

$$N_{excess} = N_{ON} - \alpha N_{OFF} \tag{3.1}$$

The significance (S) of the signals for the VHE gamma-ray astronomy is calculated by the following *Li&Ma* formula (Li and Ma, 1983):

$$S = \sqrt{2}(N_{ON} ln[\frac{1+\alpha}{\alpha}(\frac{N_{ON}+N_{OFF}}{N_{ON}})] + N_{OFF} ln[(1+\alpha)(\frac{N_{OFF}}{N_{ON}+N_{OFF}})])^2 \tag{3.2}$$

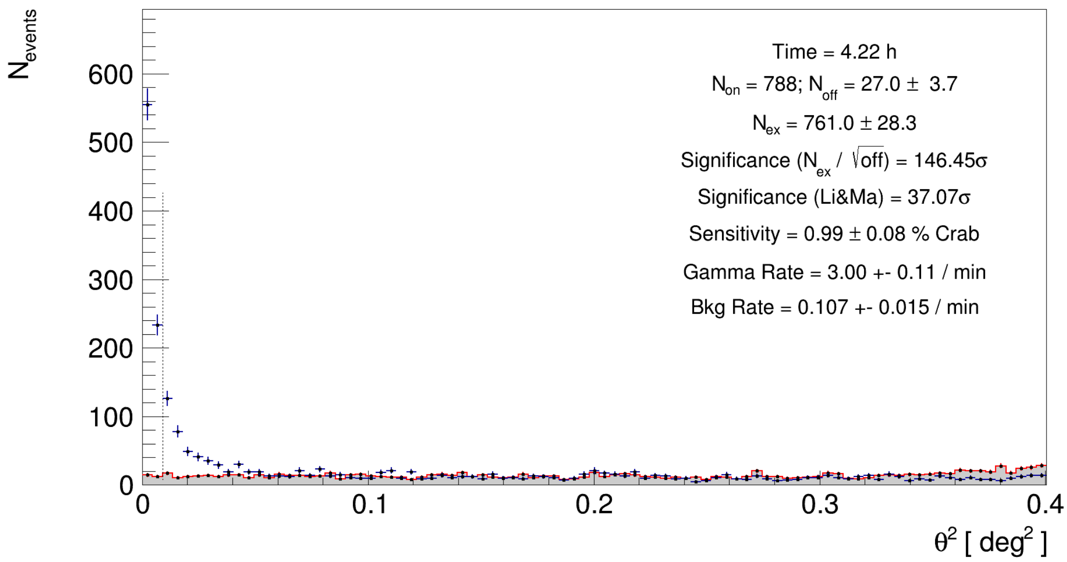

FIGURE 3.15: An example of *Theta*^{2} histogram created with the program, Odie. The blue points represent the events collected from the ON region, while the red ones are from the OFF region. In addition to the significance of the signal, more information can be obtained with the program, such as gamma and background rates per minute.

- **Flute:** With this program, flux and spectrum calculations are performed. Firstly, the program applies the hadronness and the *Theta*^{2} cuts. The user can define the cuts, or Flute determines the energy dependence of the cuts to achieve a given signal efficiency (selected by the user). Afterward, it calculates from the MC events the instrument response functions (collection area, and energy dispersion matrix) needed to convert the observed event rates into gamma-ray fluxes versus energy and time. Finally, the Spectral Energy Distribution (SED) (see Figure 3.16) and the Light Curves are produced.

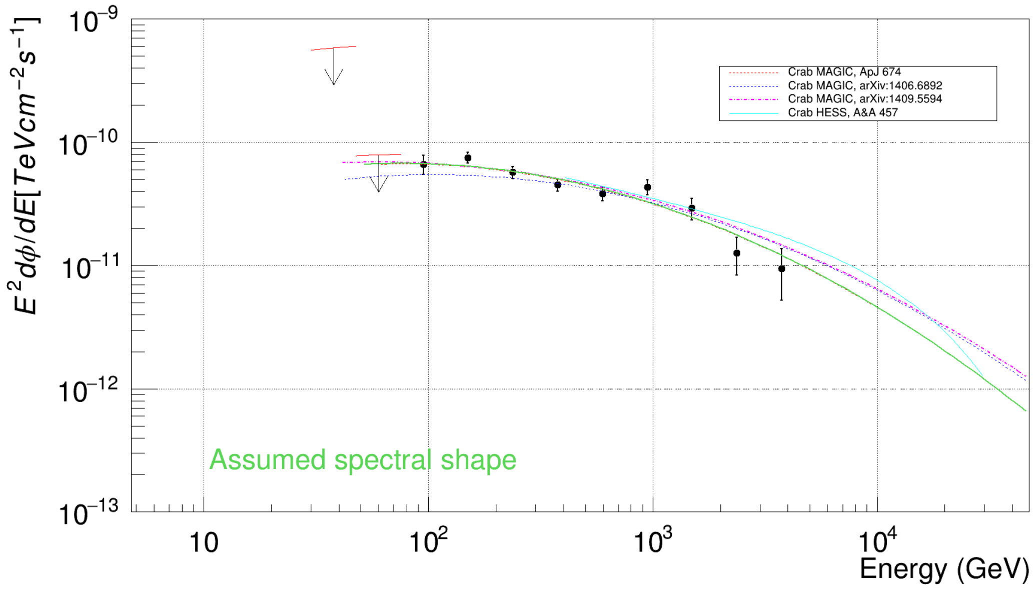

FIGURE 3.16: An example of an SED of Crab Nebula created with the program Flute. The recorded data are compared with the previously published Crab Nebula results. A spectral shape fit can also be obtained with this program.

- **Foam:** This program merges the spectrum of different observation periods, taking into account each period's collection area and weighting them accordingly.
- **Fold:** This program performs spectral unfolding by using either the output of flute or foam. The aim of this procedure is obtaining the energy spectrum (in true energy (E_{true})) of the observed gamma rays using a likelihood maximization approach, assuming a certain spectral model (e.g. a power-law).
- **Caspar:** This program creates skymaps (see Figure3.17), which are 2-D histograms of the events showing the relative flux to the residual background.

In this section, the standard scientific outputs of the higher-level analysis are shown. In addition to these, the energy threshold of the analysis, light curves of the pulsars, and custom scientific outputs can be created by writing custom root-based C++ codes.

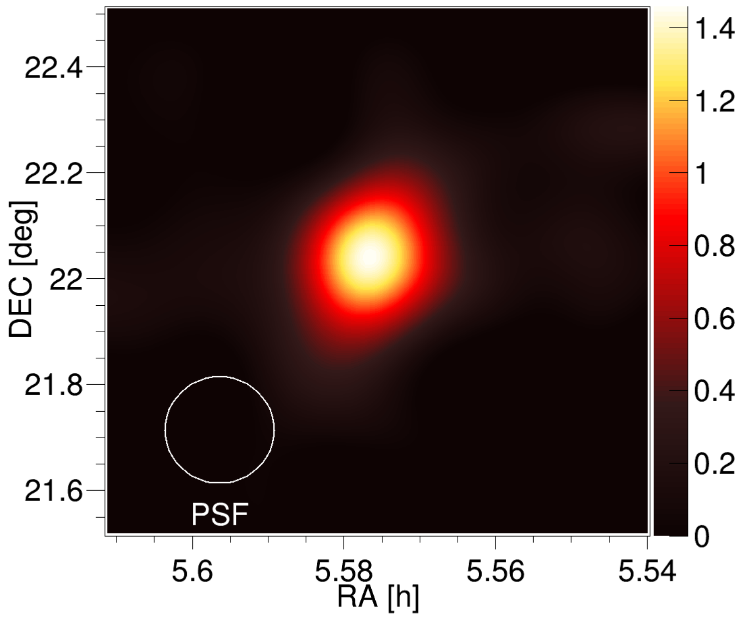

FIGURE 3.17: An example for the relative flux (in arbitrary units) skymaps created with the program Caspar. The relative flux is calculated as the number of smeared excess events divided by the residual background flux within 0.1 degrees (Zanin et al., 2013).

3.5 The Future of IACTs: the Cherenkov Telescope Array

The Cherenkov Telescope Array (CTA) is the next-generation ground-based gamma-ray observatory that is currently being constructed (see Figure 3.18). The aim of the observatory is hosting around 100 IACTs at the two different sites at the north and the south hemispheres. Three classes of telescopes are being designed to observe the gamma-rays in the energy range of 20 GeV to 300 TeV: Large-Sized Telescope (LST), Medium-Sized Telescope (MST), and Small-Sized Telescope (SST).

In addition to telescopes, it is planned to include different instruments to monitor atmospheric conditions on the sites (Daniel and CTA Consortium, 2015). One of these motoring systems is the Raman LIDAR system which is explained in more detail in Chapter 4).

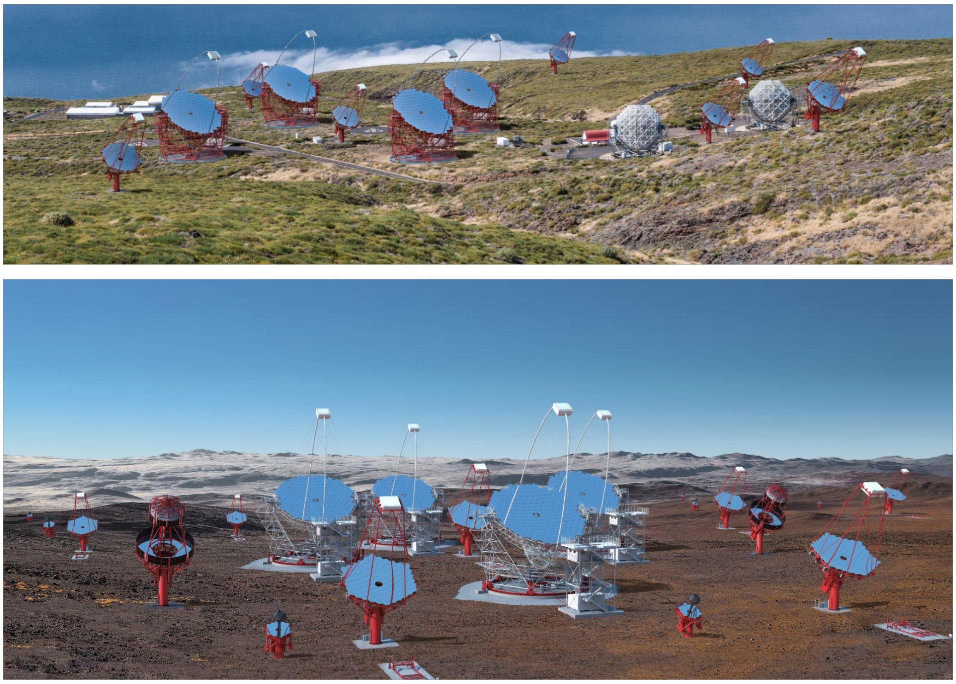

FIGURE 3.18: Artistic rendering of CTA observatory (Credit: Gabriel Pérez Diaz, IAC / Marc-André Besel, CTAO). CTA's southern hemisphere (CTA-S) site (in the up) will be located at the Instituto de Astrofisica de Canarias' (IAC's) Observatorio del Roque de Los Muchachos on the island of La Palma. Two MAGIC Telescopes can also be seen. CTA's northern hemisphere (CTA-N) site (in the down) will be located at the European Southern Observatory's (ESO's) existing Paranal Observatory in the Atacama Desert in Chile.

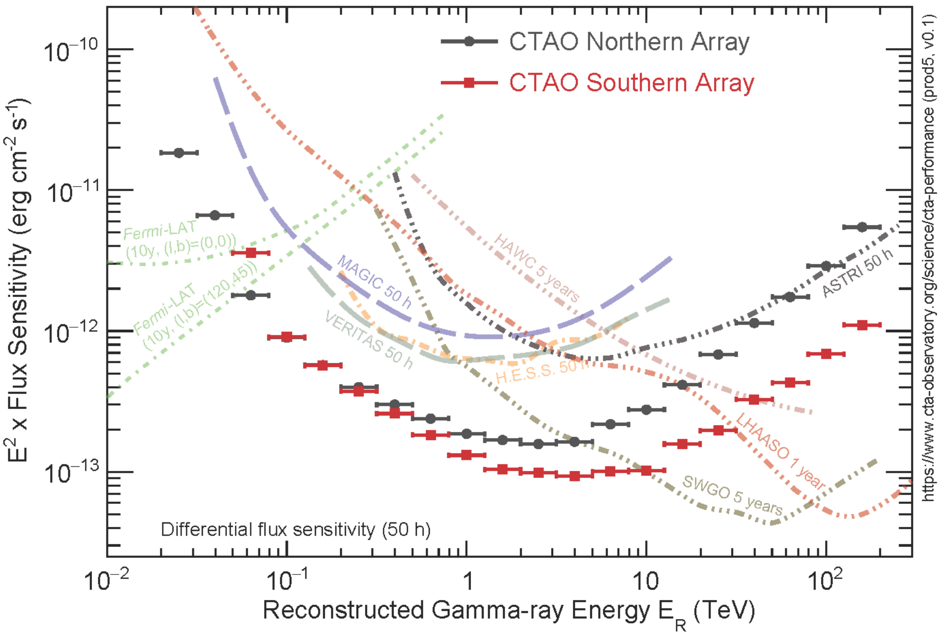

FIGURE 3.19: CTAO-N and CTAO-S sensitivity compared to the other instruments. (Credit:CTA-Observatory)

Chapter 4

LIDAR Systems for IACTs

Light detection and Ranging (LIDAR) systems are used for volumetric analysis in various fields, such as wind speed calculations for surfing purposes, water searches on the atmosphere of Mars, mapping the Amazon rainforests, or even in our cellphones nowadays for mapping the environment.

The significant usage of LIDAR systems for IACTs is the volumetric analysis of the atmosphere in order to estimate the light loss. As mentioned in the previous chapter, atmospheric showers are formed in the atmosphere at an altitude of 10 - 20 km above sea level. The light received from the particle showers depends on the atmospheric aerosol profile, which can be affected by the daily or seasonal variations in the atmosphere. Therefore, volumetric analysis of the molecular profile by LIDAR systems is beneficial for understanding and correcting light loss.

This chapter aims to give background information on LIDAR systems by describing working principles, essential calculations of LIDAR systems, and the MAGIC LIDAR basics, which the MAGIC Telescopes actively use during the observations. Lastly, Barcelona Raman LIDAR, CTA's pathfinder, will be presented. Polychromator characterization for light leakage tests will be explained. Finally, the first commissioning results will be reviewed.

4.1 Atmospheric effects

Peak emission of Cherenkov light from a typical atmospheric shower is produced at around 10km height of the atmosphere. The recorded radiation is mainly distributed between 300 nm to 600 nm (see Figure 4.1). Therefore, in this section, we will focus on the composition of the atmosphere and probable attenuation reasons for this wavelength range.

The atmosphere can be classified into five different layers. More than 90 percent of the mass is concentrated within the last two layers closest to the ground, the troposphere and the stratosphere, due to the exponential profile of the air density. The troposphere is the closest layer to Earth's surface with 10-15 km thickness, and the meteorological phenomena occur in this layer. Thus air molecules, and aerosols in this layer are the principal attenuation reasons for Cherenkov light.

The major factors which reduce the total transmission of the Cherenkov light in the atmosphere are molecular and aerosol scatterings (see Figure 4.2). These scatterings are generated by two elastic scattering phenomena called Rayleigh and Mie. Scattering models depend on the size of the target and the wavelength of the incident photons.

Rayleigh scattering was first proposed by Lord Rayleigh to explain the blue sky. This phenomenon occurs while the photon wavelength is much larger than the size of the target ($\lambda >> $ d), mainly corresponds to atoms or molecules in the atmosphere.

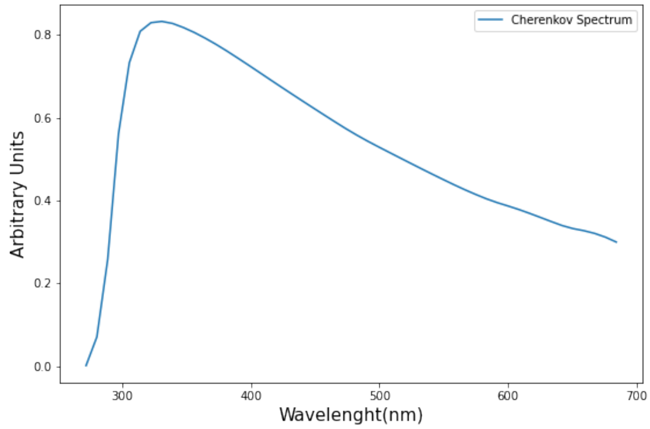

FIGURE 4.1: Typically observed spectrum of Cherenkov light generated by vertical TeV air showers at the altitude of 2200 m. The airshower light exposes to wavelength-dependent attenuation in the atmosphere. Adapted from (Doering et al., 2001).

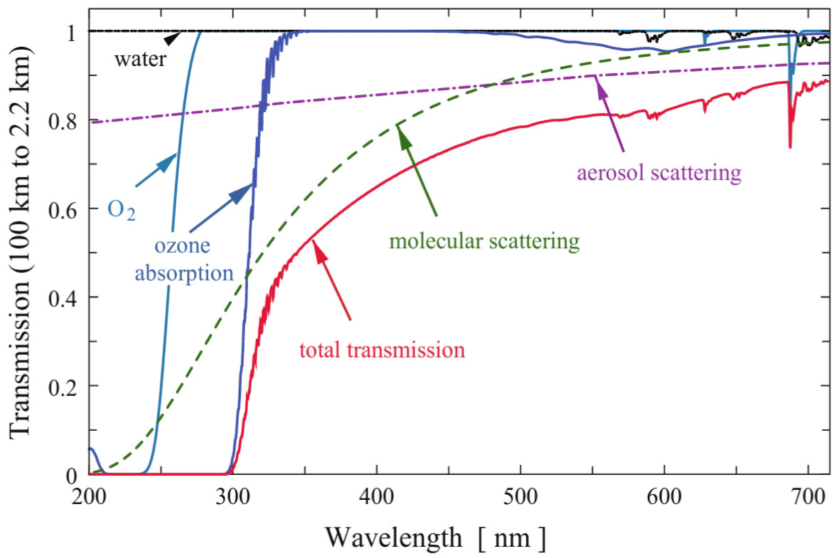

FIGURE 4.2: Direct transmission of light from space (here 100 km) altitude along a vertical path to an altitude of 2.2 km, as calculated with MODTRAN. The impact of the most important absorbers and scatterers is shown. Adapted from (Bernlöhr, 2000)

This phenomenon is relatively easy to model that the scattering coefficient of the molecules depends on the fourth power of the wavelength as in the equation 4.1:

$$\sigma_{sca,mol} \propto \lambda^{-4} \tag{4.1}$$

Additionally, when the photon wavelength is comparable or larger than the target size ($\lambda \geq$ d), Mie scattering occurs. This phenomenon was named after Gustav Mie. This case can explain the aerosol scattering mechanism caused mainly by clouds, fog, dust, or calima (winds including dust and sand coming from Africa) in the atmosphere. Mie scattering is harder to model because the scattering coefficient depends on the refractive index, size, and aerosols' shape. With a prior assumption of spherical targets, the Mie scattering is associated with the photon wavelength as in the equation 4.2

$$\sigma_{sca,aer} \propto \lambda^{-\text{Å}} \tag{4.2}$$

The Å refers to the Angstrom coefficient, which varies between 0.1 to 1.5 depending on the aerosol type.

On the other hand, inelastic Raman scattering is a relatively rare case compared to the elastic scatterings explained above. The occurrence of Raman scattering of a molecule is in the order of 10^{-4} to 10^{-3}. In this process, the molecule either gains energy with Stokes scattering or loses energy with Anti-Stokes scattering (see Figure 4.3). As a result, the wavelength of backscattered light will be shifted, which is unique for each molecule.

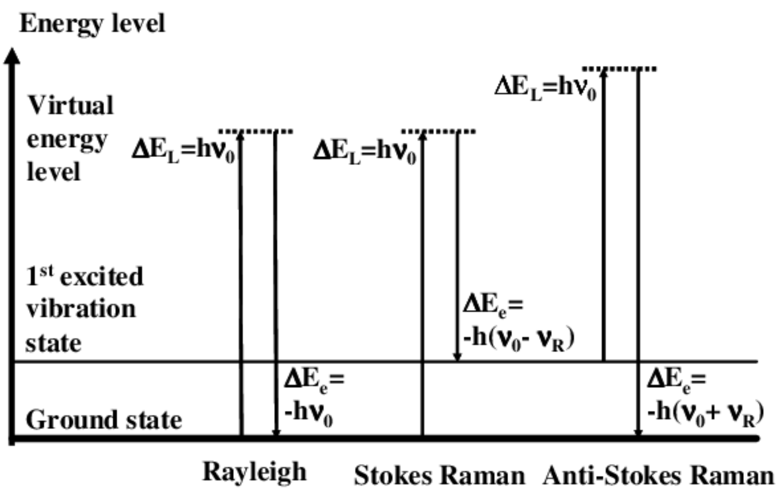

FIGURE 4.3: Energy diagram of Rayleigh, Stokes Raman and Anti-Stokes Raman scatterings (Wróbel, 2016).

4.2 LIDAR Technique

LIDAR systems are similar to RADAR or SONAR systems, which are utilized to scan the structure of a region remotely by active sensing methods. The working principle is the following: a pulsed laser is emitted into the target region, which is the atmosphere in our case. The backscattered light is then collected by a telescope and focused on a photo sensor that measures the amount of light returned. As a result, the received light travels twice the distance between the target and the laser.

The return power of the LIDAR can be calculated as in equation 4.3 called LIDAR equation ((Piironen and Eloranta, 1994)):

$$P(r,\lambda) = P_0 \frac{ct_0}{2} \beta(r,\lambda) \frac{A}{r^2} e^{-2\int_{r_0}^{r} \alpha(r,\lambda) dr} \tag{4.3}$$

In this equation, $P(r,\lambda)$ represents the return power received by the telescope. P_0 is the initial laser power, c is the speed of light, t_0 is the laser's pulse time, $\beta(r,\lambda)$

is the backscatter coefficient, r is the distance where the laser emission scattered in the atmosphere, A is the diameter of the telescope,λ is the wavelength, $\alpha(r, \lambda)$ is the extinction coefficient.

In this equation, there are two unknowns, extinction coefficient in equation 4.4 and backscatter coefficient in equation 4.5

$$\alpha(r, \lambda) = \alpha_{sca}^{aer}(r, \lambda) + \alpha_{sca}^{mol}(r, \lambda) + \alpha_{abs}^{aer}(r, \lambda) + \alpha_{abs}^{mol}(r, \lambda) \tag{4.4}$$

$$\beta(r, \lambda) = \beta_{sca}^{aer}(r, \lambda) + \beta_{sca}^{mol}(r, \lambda) \tag{4.5}$$

The relation between extinction and backscatter coefficients are known as the LIDAR ratio and can be written in two forms for molecular ratio in equation 4.6 and aerosol ratio 4.7.

$$L^{mol}(r, \lambda) = \frac{\alpha^{mol}(r, \lambda)}{\beta^{mol}(r, \lambda)} \simeq \frac{8\pi}{3} \tag{4.6}$$

$$L^{aer}(r, \lambda) = \frac{\alpha^{aer}(r, \lambda)}{\beta^{aer}(r, \lambda)} \tag{4.7}$$

The solution of the molecular LIDAR ratio is more straightforward and can be solved with elastic scattering phenomena. On the other hand, the aerosol LIDAR ratio is more complex to be solved, as mentioned for Mie scattering.

There are two main approaches to solving the LIDAR equation. The first approach is using some assumptions in order to solve the equation with single wavelength LIDAR systems. The most common methods are the slope method and the Klett method for forward or backward integration (Klett, 1981). The second approach uses both the elastic scattering λ_0 and Raman shifted light λ_{Raman} as a two inputs for solving the LIDAR equation. Thus, we can obtain two independent equations for two unknowns and the LIDAR equation can be solved with the following equation 4.8

$$\alpha^{aer}(r, \lambda_0) = \frac{\frac{d}{dr} ln(\frac{N_{Raman}(r)}{r^2 P(r, \lambda_{Raman})}) - \alpha^{aer}(r, \lambda_0) - \alpha^{mol}(r, \lambda_{Raman})}{1 + (\frac{\lambda_0}{\lambda_{Raman}})^{\mathring{A}}} \tag{4.8}$$

Approximately 78 % of the atmosphere consists of Nitrogen molecules (N_2), while 12% is composed of Oxygen molecules (O_2). Hence, Raman LIDAR systems widely use elastic and inelastic scatterings to solve the LIDAR equation and characterize the atmosphere. As can be seen in Figure 4.4, 532 nm incident photon has an elastic Rayleigh scattering at 532 nm and Raman scattering from N_2 at 607 nm. These phenomena occur similarly for inelastic scattering incident photon at 355 nm as elastic scattering at 355 nm and Raman scattering from N_2 at 387 nm.

4.3 The MAGIC LIDAR

The MAGIC LIDAR (see Figure 4.5) is a LIDAR system that operates with the MAGIC Telescopes to check and analyze the atmospheric effects during the data taking. The doubled frequency Nd:YAG laser operates at 532nm for elastic Rayleigh scattering with 5μJ pulse energy and 1kHz repetition rate. The backscattered light is collected with a 60cm diameter telescope with a 1.5m focal length. A pair of lenses and an interference filter are used to select photons in the 529-535 nm range. Then the

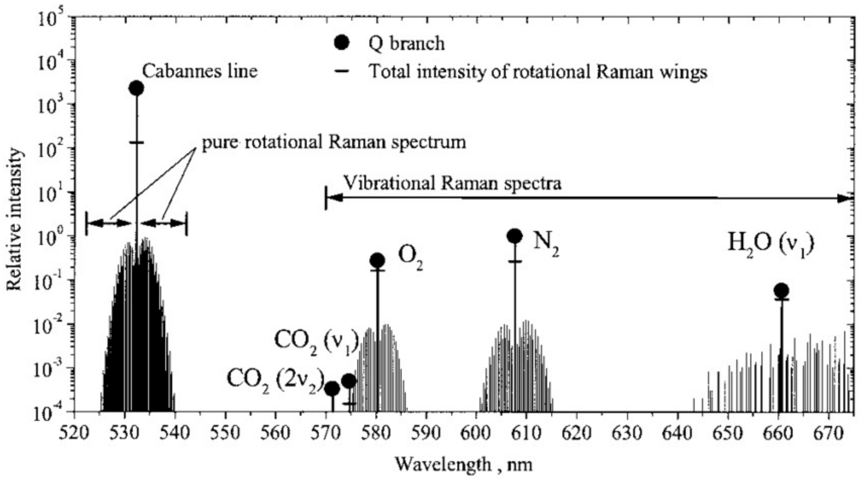

FIGURE 4.4: Overview of lidar backscatter signals for a laser wavelength of 532 nm. The temperature was set to 300K for the rotational wings' calculation. While elastic Rayleigh scattering occurs at 532nm, Raman scatterings of O_2 and N_2 occur at 580nm and 607nm, respectively (Behrendt et al., 2002).

backscattered light is recorded by Hamamatsu Hybrid Photo Detector (HPD) with a quantum efficiency of 55 percent at 532 nm (Fruck et al., 2014).

FIGURE 4.5: The MAGIC LIDAR (Fruck et al., 2014)

Because the MAGIC LIDAR is a single wavelength system, the lidar ratio is predicted with Klett's method (Fruck et al., 2014). These measurements are performed by analyzing the backscattered signal from 50000 single laser shots. Figure 4.6 shows a typical LIDAR plot of backscattered signal in which recorded delay times are converted to the distance by multiplying the speed of light by the delay time divided by two. The light loss is predicted using the slope method for the different layers of the atmosphere and calculations of the light loss caused by clouds or aerosols. As a result, we get the transmission values, which vary between 0 to 1.(Fruck et al., 2014)

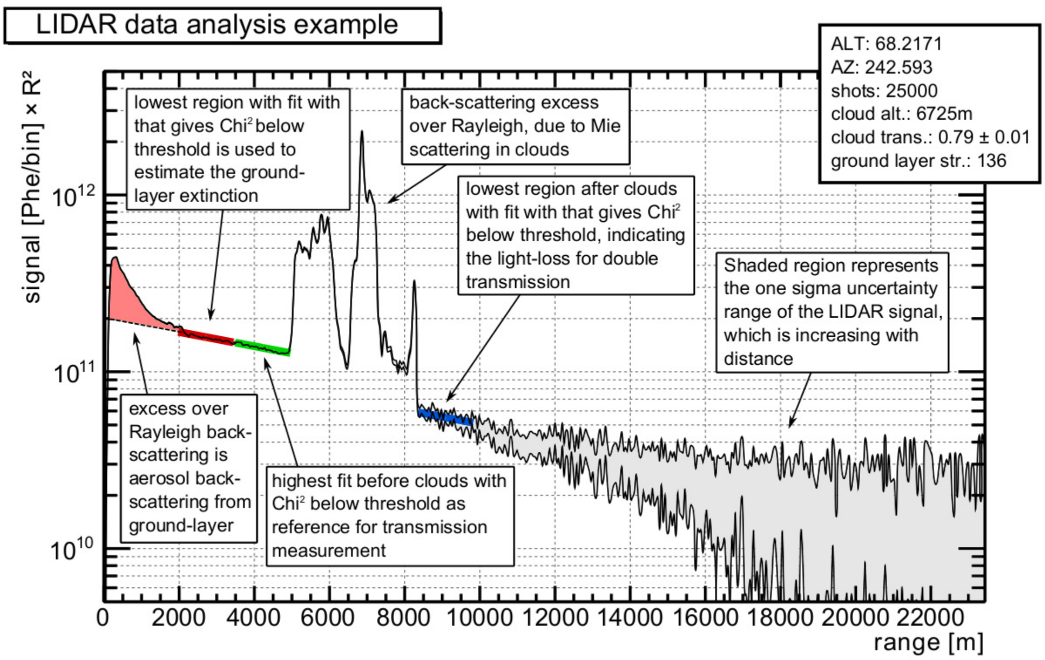

FIGURE 4.6: Illustration explaining the data analysis algorithm (Fruck et al., 2014)

4.4 The Barcelona Raman LIDAR

The Barcelona Raman LIDAR is a pathfinder of CTA for atmospherical transmittance analysis during the observations with excellent accuracy compared to the other LIDAR systems(see Figure 4.7.

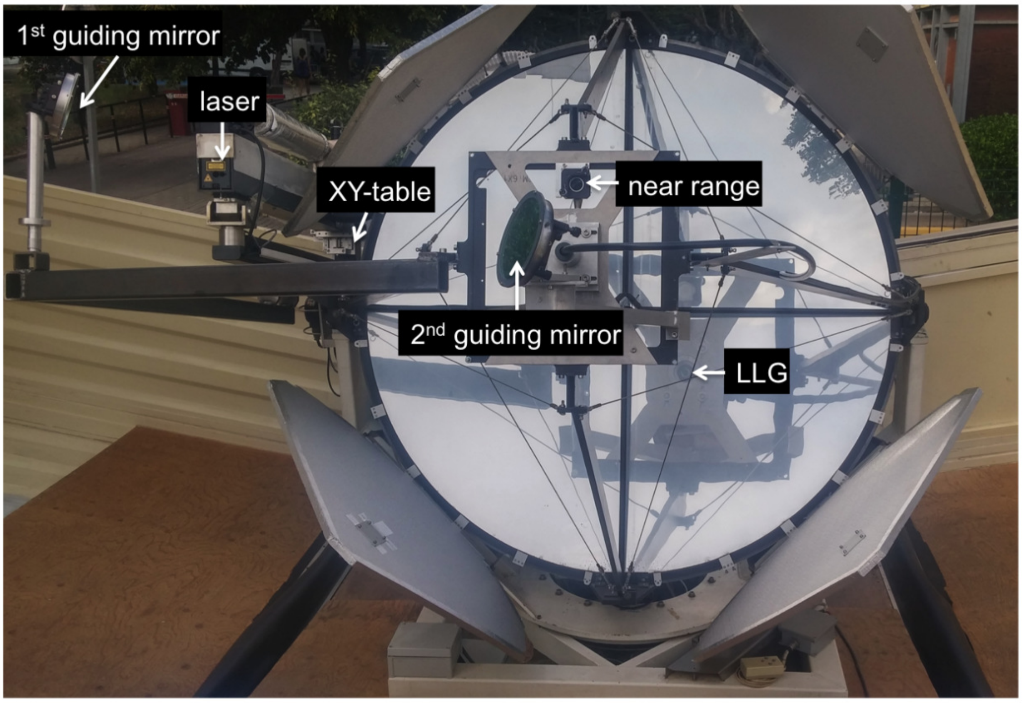

FIGURE 4.7: The Barcelona Raman LIDAR (Gaug et al., 2019)

It consists of 5 main components: the telescope, the laser, the polychromator, the data acquisition unit, and the data processor and display (see Figure 4.8.

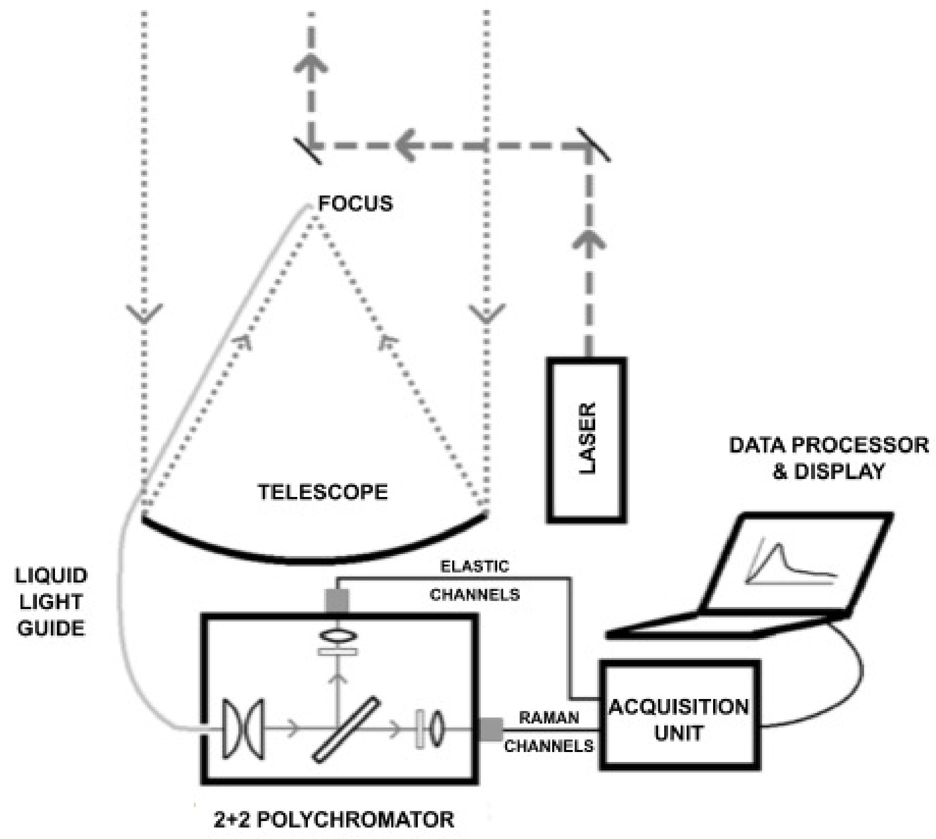

FIGURE 4.8: Schema of the Barcelona Raman LIDAR

The system was recycled from the discontinued CLUE experiment's openable shipping container, telescope, and the mount (Alexandreas et al., 1995). Frequency-doubled and tripled Nd: YAG laser is utilized for operations at 532nm and 355nm. The laser is mounted on an X-Y table for adjusting the laser beam co-axial to the telescope. The backscattered light is collected by a 1.8m diameter parabolic mirror with a 1m focal length telescope. Afterward, the focused light is transferred through Lumatec Series 300 liquid light guide (LLG) and separated into four different wavelengths (355 nm,532 nm,387 nm,607 nm) by in-house built polychromator (Deppo et al., 2012). Finally, the light is collected by four Hamamatsu R11920 high quantum efficiency PMTs and sent to a data acquisition system of LICEL (see Table 4.1).

4.4.1 Polychromator Light Leakage Tests

As mentioned in the previous section, the polychromator aims to separate four different wavelengths successfully. The incident light carried by the LLG is collimated by 100mm Lens Couples (LC) as soon as they enter to the polychromator box (see Figure 4.9 a). Eventually, the light beam is either reflected or transmitted by three Dichroic Mirrors(DM) placed 45 degrees to the entering angle (see Figure 4.9 b). 355nm, 387nm ve 532 nm wavelengths are channeled to corresponding outputs respectively through these DMs, and lastly, 607nm wavelength is directed to its output.

TELESCOPE	
Type	Former CLUE experiment container
Mirror	Parabolic mirror of 1.8 m diameter and 1.8 m focal length
Shadowing	Shadow of 400 cm 2 at the focal plane
Mirror reflectivity	55 % (current), 90% (upgraded)
LASER	
Model	Quantel Brilliant Nd:YAG
Wavelengths	1064 nm (primary), 532 nm and 355 nm (harmonics)
Energy per pulse	60 mJ
Pulse Repetition Frequency (PRF)	20 Hz
Beam waist diameter	6 mm
Beam divergence	0.5 mrad
Pulse duration	5 ns
LIQUID LIGHT GUIDE	
Model	Lumatec Series 300
Length	1.8 m
Active area diameter	8 mm
Numerical Aperture (NA)	0.59 (34 25e6 half-angle)
Transmissivity	> 0.7
Coupling to telescope	0.9
PHOTON-DETECTORS	
Type	Photomultiplier tubes
Model 1	Hamamatsu R11920-100 1.5 2019(for 355, 387, 532 nm)
Model 2	Hamamatsu H10425-01 1 2019 (for 607 nm)
Quantum efficiency	355 nm, 387 nm (45%), 532 nm (25%) with R11920-100
Quantum efficiency	607 nm (10%) with H10425-01
Dark current	3 nA
Current responsivity	1.1×10^5 A W
Transimpedance gain	50 ω
Internal gain	2×10^6
Noise factor	1.8
ACQUISITION UNIT	
Model	LICEL TR20-160
Analog-to-digital mode	20 Mbps 12 bit
Photon-counting mode	250 MHz
POLYCHROMATOR UNIT	
Model	Home-made
Lens transmissivity	95% each
Dichroic transmissivity	90% each
Dichroic reflectivity	95% each
Interference filters transmissivity	90% each

TABLE 4.1: The Barcelona Raman LIDAR parameters

The beam lights are again focused on each channel by LCs, and Interference Filters filter their noise (IF).

The polychromator is a large box with dimensions of 760mm x 550mm x 170mm with a total weight of 30kg (see Figure 4.9 c). Apart from the central part of the polychromator, there is an outer box which prevents possible light leakage from outside and environmental hardware noise with the help of an aluminum shield (see Figure 4.9)

Since high-precision measurements aimed with this system, light leakage tests had vital importance for the reliability of the system. It is essential to control if the Raman signal, which is two orders of magnitude lower than the elastic signal(see

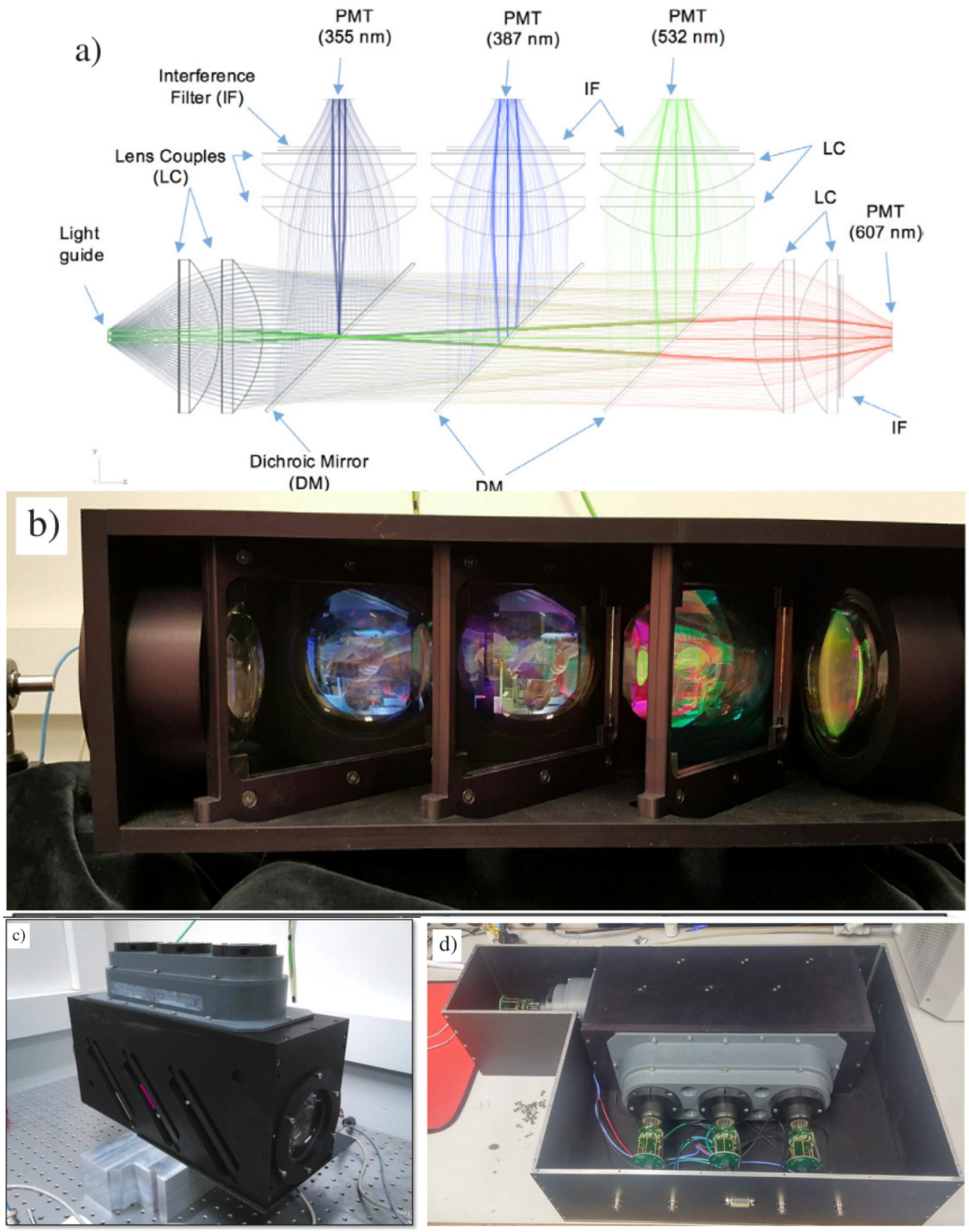

FIGURE 4.9: The Polychromator of the Barcelona Raman LIDAR. In the upper part a), the design for separating the incident light to 355nm, 387nm, 532nm, and 607nm can be seen. Lens couples, dichroic mirrors, and interference filters were used for this purpose. b) shows a picture of the polychromator's inner part. c) and d) show the output channels, connected PMTs, and the extra box for protecting the polychromator from environmental effects (Gaug et al., 2019).

Figure 4.10), is affected by external or internal factors. In this study, it was tested whether there was light leakage in Raman channels.

Before starting the tests, all parts were tested independently (Lopez Oramas et al., 2013) , and (López Oramas, 2014). The light leakage test setup of the polychromator, illustrated in Figure 4.11, consisted of 3 main groups: polychromator box,

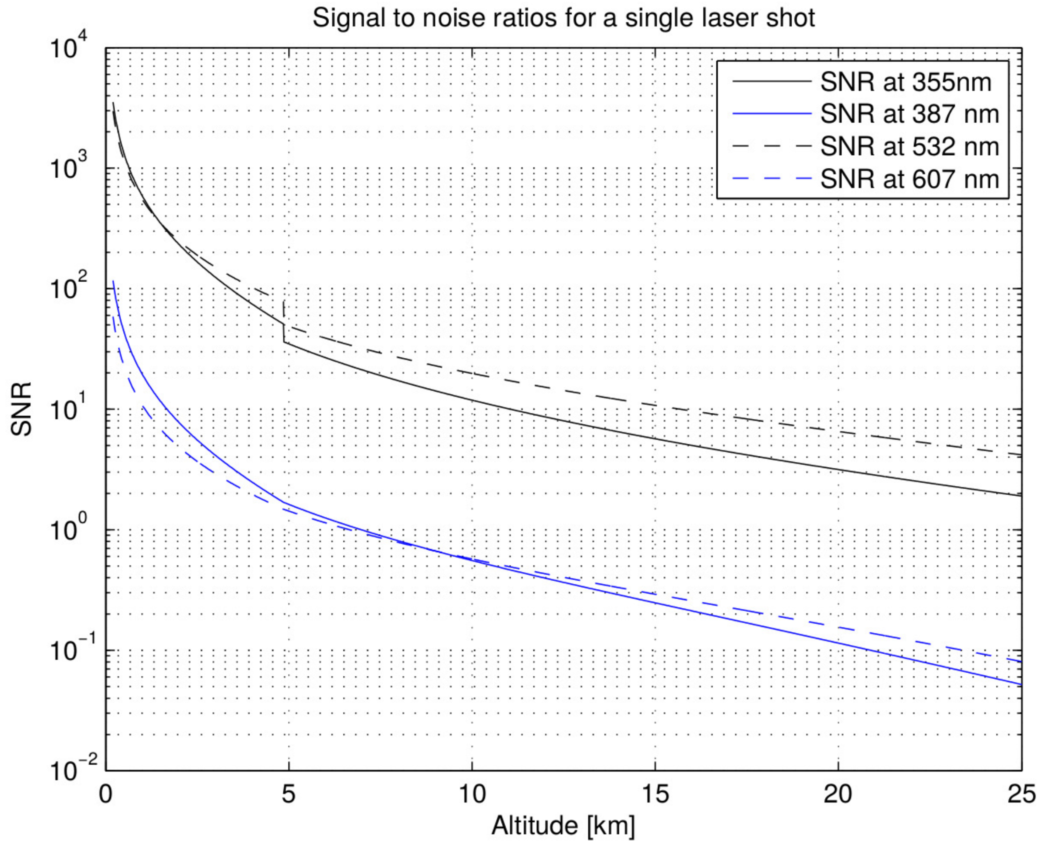

FIGURE 4.10: The return power of the Barcelona Raman LIDAR was estimated by link-budget simulation (Eizmendi Valles, 2011). The solid black line and dashed line refer to elastic scatterings of N_2 at 355nm and 532nm. The blue solid and dashed lines refer to inelastic Raman scattering of N_2 at 387nm and 607nm. The expected signal to noise ratio of Raman scatterings is two orders of magnitude lower than the elastic ones.

a light source system, and LLG. 4 pin diodes used for these tests. The light coming out of the Xe lamp (see Figure 4.13 for the spectrum) passed through a black box with collimator and filter sets, and then the wavelengths were selected with a monochromator. Just outside this black box, there was a shutter for background noise measurements.

The light coming out of the Xe lamp stabilized within 1-2 hours was transmitted to the polychromator with LLG's help after passing through the system mentioned above. For these tests, firstly, the measurement was made with 1nm steps between 300nm and 600nm with the shutter open (see Figure 4.11). Blue 355nm, orange 387nm, green 532nm, red show the signal measurement results on 607nm channels, with peak points corresponding to 238 µA, 437 µA, 341 µA, 25 µA, respectively.

After this first signal measurement, light leakage tests were started. Because the Raman scattering from the atmosphere is a weak signal and Rayleigh scattering is very dominant compared to this signal. Therefore, the purpose of these tests is to check possible light leakage from Rayleigh scattering in the Raman channels. For this reason, measurements were made from 387 and 607 Raman channels to test the presence of any Rayleigh markings in both channels in the 522-542 nm and 345-365 nm ranges to check whether there would be any Rayleigh markings. These tests

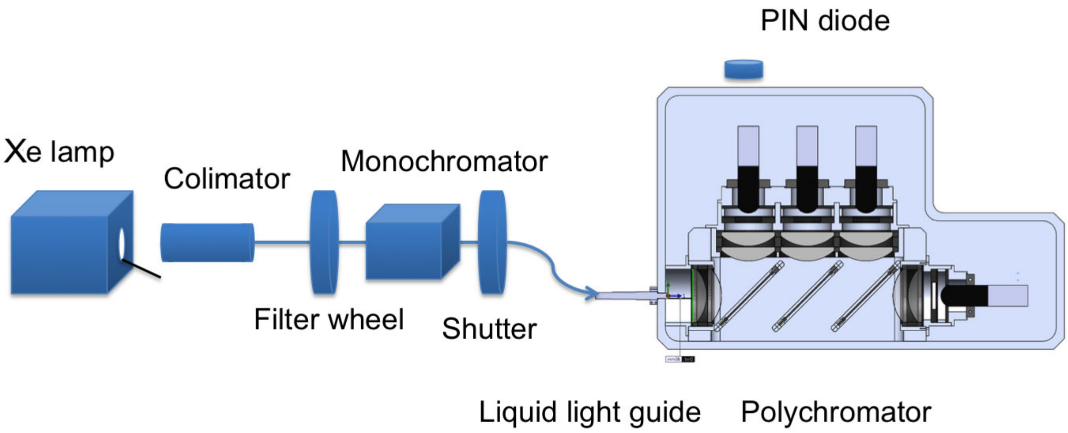

FIGURE 4.11: Illustration of the setup used for the light leakage tests of the polychromator (Gaug et al., 2019). It consisted of a xenon lamp, collimator, and filter wheels for removing unnecessary harmonics. A monochromator was used for selecting specific wavelengths, while the shutter was used for recording ON and OFF data for background subtraction.

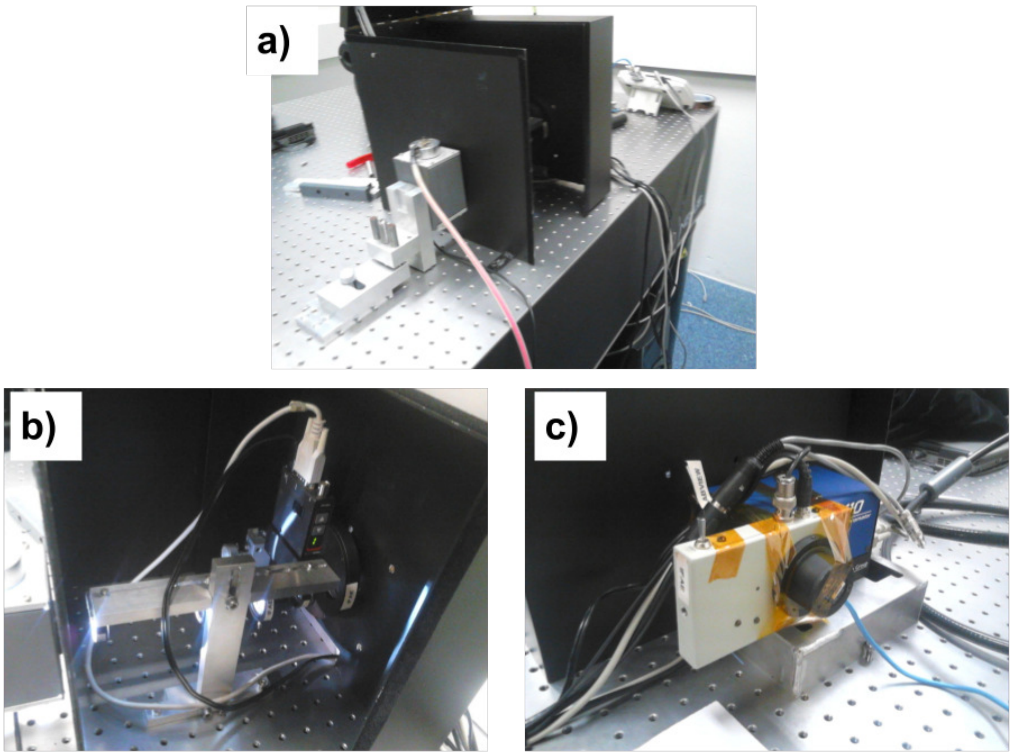

FIGURE 4.12: Photos of the setup used for the light leakage tests of the polychromator Blackbox that was used for the polychromator tests. used materials. CM110 Compact Monochromator, Newport 818-UV Low-Power Silicon Cylindrical Detector, thorlab FW102C filter wheels,

were scanned with monochromator at 522-542 and 345-365nm intervals with 1 nm steps. With these scans shutter open and closed, two measurements of each nm scan were recorded. This scan is repeated 1000 times. As a result, 1000 on, 1000 off

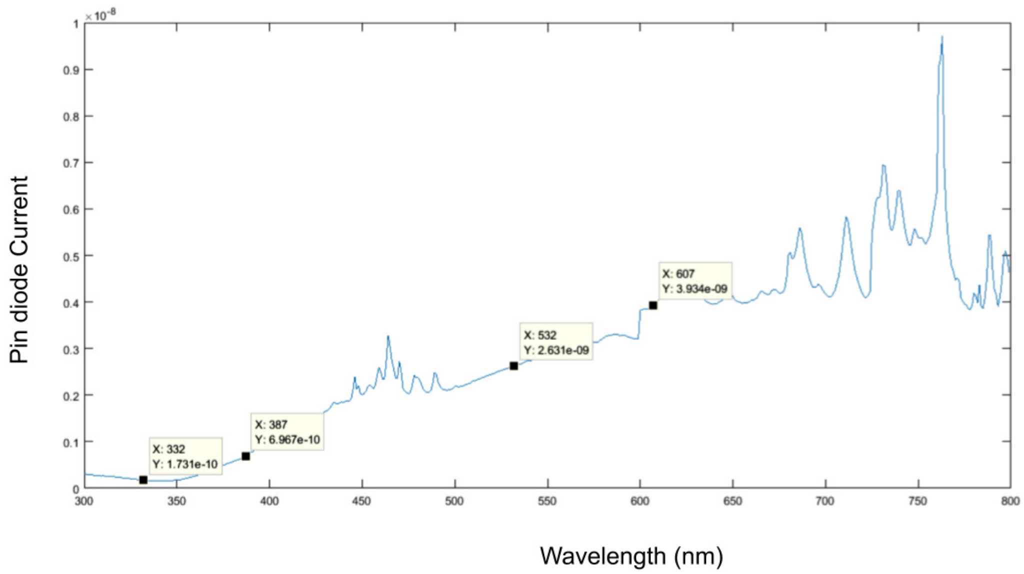

FIGURE 4.13: Spectrum of the Xenon Lamp used for the light leakage tests which is recorded by a pin-diode. Credit: Oriol Calpe

measurements were taken for each wavelength.

The results of the test can be seen in Figure 4.15. Top right and left plots show off subtracted PMT currents to check possible 355 and 532 Rayleigh leakages in 387 Raman channels. Likewise, the bottom right and left panes show the results of the 607 channel. We obtained 0.02 ± 0.17 pA, 0.01 ± 0.17 pA, 0.00 ± 0.16 pA , 0.00 ± 0.18 pA respectively which refers to signal/noise ratios in 387nm Raman channel 2.2 x 10^6 , 607 Raman channel 1.3 x 10^5.

	355 nm leakage	**532 nm leakage**
387 nm Raman Channel	0.02 ± 0.17 pA	0.01 ± 0.17 pA
607 nm Raman Channel	0.00 ± 0.16 pA	0.00 ± 0.18 pA

TABLE 4.2: Light Leakage Results in Raman Channels

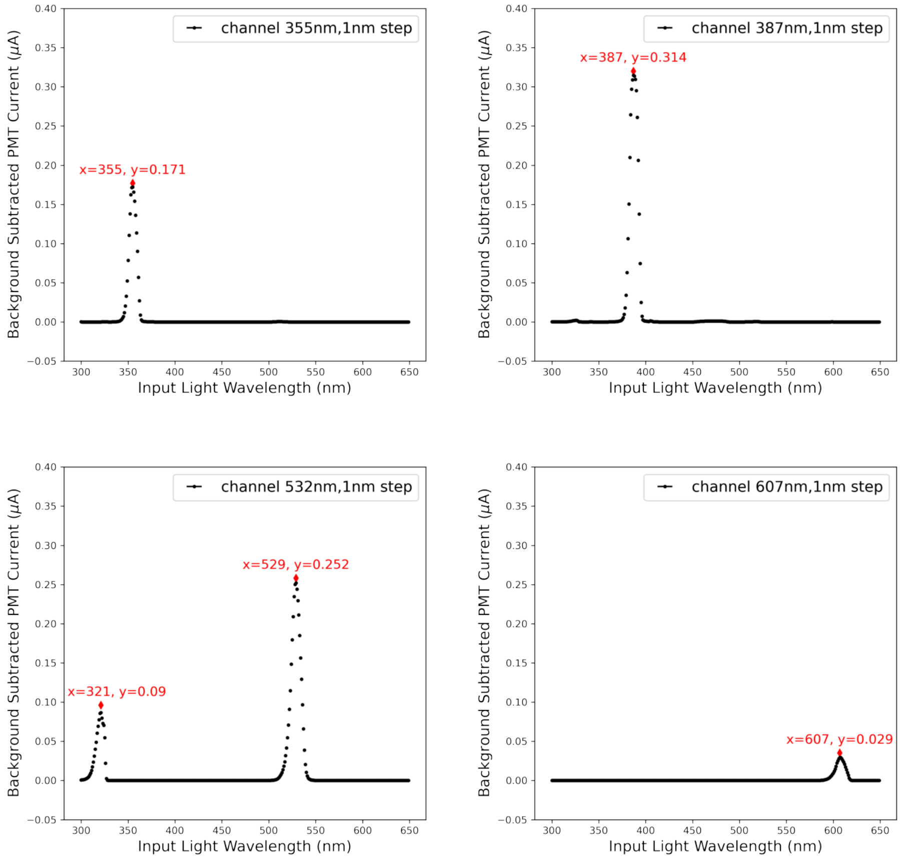

FIGURE 4.14: Scan for each output of the polychromator. One ON and one OFF data were taken with a 1nm step scan. The peak emission of the background-subtracted results shows that the polychromator is capable of separating the wavelengths to the outputs successfully.

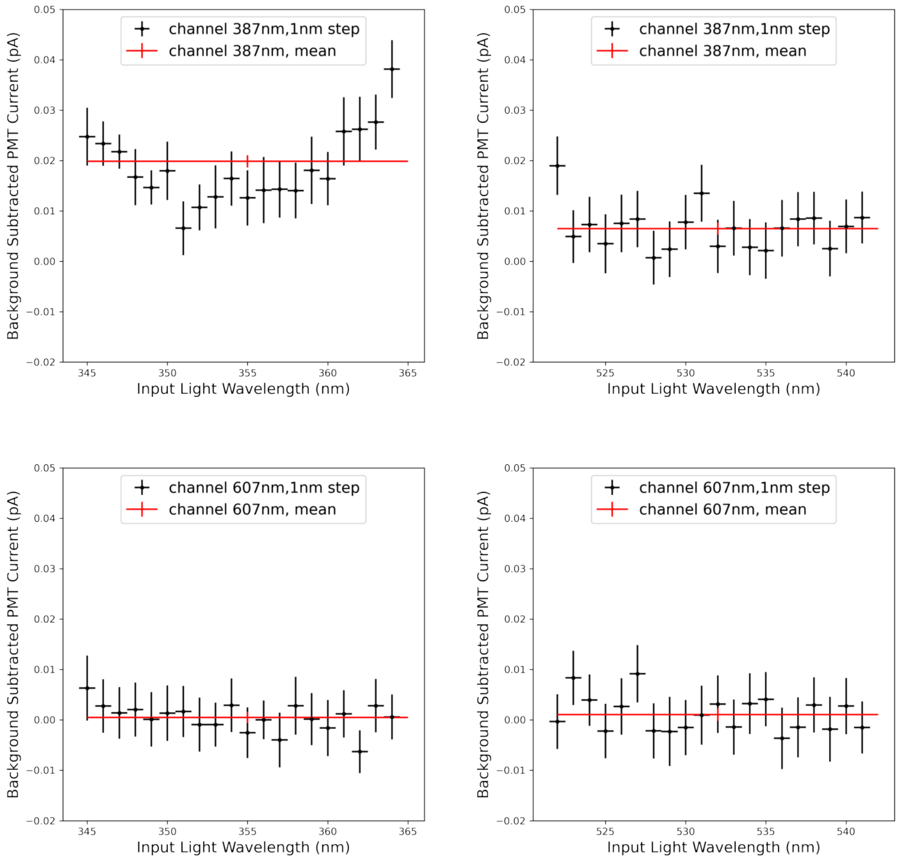

FIGURE 4.15: Light leakage tests for the 387 nm and 607 nm Raman channels of polychromator. One nm scan was performed for the corresponding wavelength ranges, and 1000 ON and 1000 OFF (for background subtraction) data was collected and subtracted after averaging for ON and OFF. The error bars were calculated by the standard deviation. The upper two figures were recorded from the 387nm Raman channel output, while the down two figures were from the 607 nm output. Possible light leakages from 355nm and 532nm elastic scattering were checked, and the results are compatible either very low or compatible with zero (see Table 4.2).

4.4.2 First commissioning results

After the tests of all parts and the light leakage test of the polychromator, the commissioning data period started and is still ongoing.

The first step in the commissioning is to align the laser. After all the safety measures are taken, the laser was shot in low power to the zenith. The beam is arranged by the eye to pass through the guiding mirrors to the zenith. After this rough adjustment, the fine-tuning started by using an oscilloscope to maximize the elastic channels' signal by moving the laser mount. The last precise alignment step was performed by checking the signal's maximum through the LICEL data acquisition system. As soon as the alignment is done, it is stable for an extended period.

The first successful commissioning data is shown in Figure 4.16 (Ballester et al., 2019). 387nm Raman scattering plots can be seen with 355nm and 532nm Rayleigh scattering. These signals were recorded by using the laser in the full power mode. With the LICEL data acquisition system, both analog and single-photon counting of the PMTs were recorded and glued see Fig 4.16. 607 nm Raman channel was too weak to detect during this commissioning tests and is still under inspection. The most probable reason is the relatively weaker signal received by the channel in Figure 4.14, in which a light loss in the polychromator could cause the signal reduction before reaching the channel.

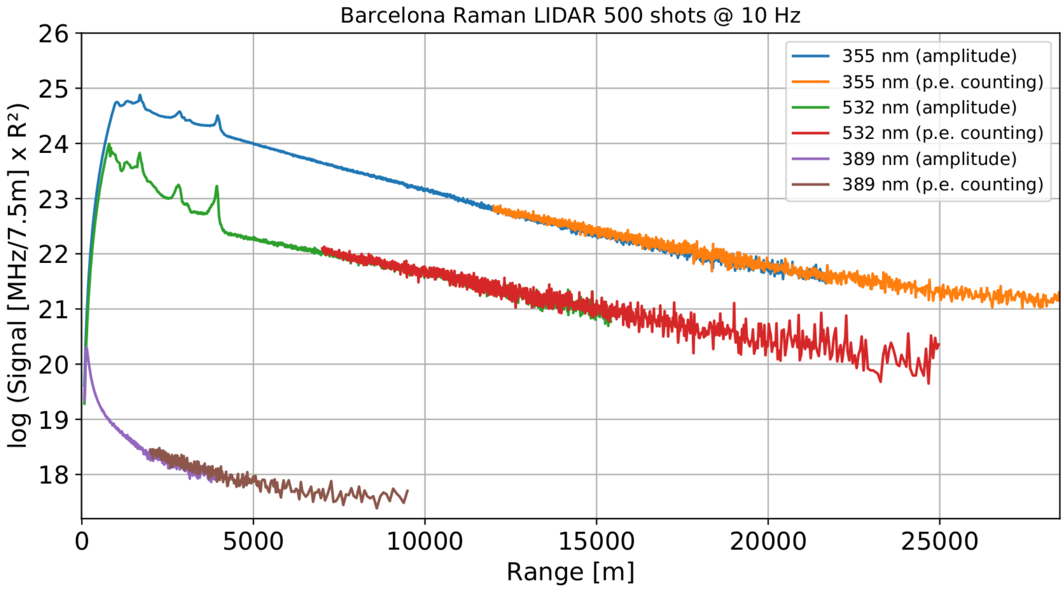

FIGURE 4.16: First commissioning Results (Ballester et al., 2019)

The first successful results show that the system can exceed 25km of the atmosphere with elastic channels. The other significant result is detecting Raman shifted light at 387nm, which shows that parallel to the polychromator light leakage tests, the full system can separate the wavelengths without any problem. As explained in previous chapters, now the Barcelona Raman LIDAR will be able to solve the LIDAR equation using both elastic and Raman channels by calculating the extinction coefficient see Figure 4.17.

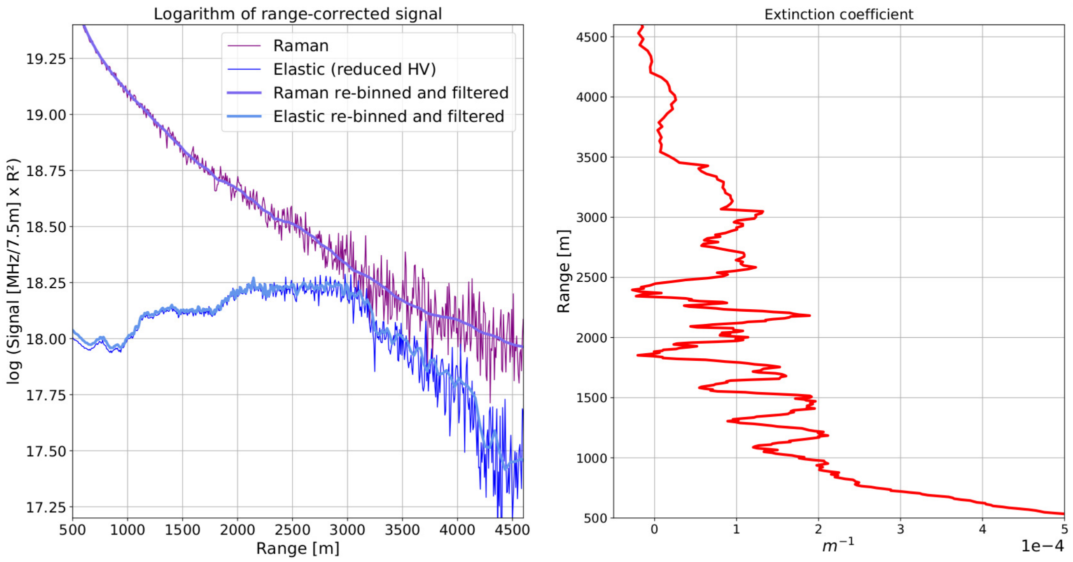

FIGURE 4.17: First commissioning Results2 (Ballester et al., 2019)

Chapter 5

PSR J0218+4232 Observations with the MAGIC Telescopes

Millisecond pulsars are essential sources to be studied for understanding the evolution of pulsars. They are also helpful for testing the emission models since their properties are different from young pulsars, as explained in Chapter 1.

The aim of this chapter is first to give the background information of the millisecond pulsar, PSR J0218+4232. After that, the MAGIC observations in 2018-2019 and analysis results will be presented. Additionally, another source in the FoV, which is 3C66A blazar, will be presented.

5.1 The Target Selection

PSR J0218+4232 (hereafter J0218) was selected after possible candidates were cataloged. First of all, all the MSPs and their properties were listed by using the catalog (Patruno, 2021). Afterward, MSPs detected by Fermi-LAT (Abdo et al., 2013) were selected, and the rest of the pulsars were excluded. Finally, the sources were checked for visibility from the MAGIC site, and not visible sources were eliminated. Table 5.1, the possible candidates and their magnetic field strengths at light cylinder radius and their characteristic ages can be found. Their magnetic field strength at the light cylinder was calculated with the following formulas in Equation 1.3.

Name	P (s)	$\dot{P}$ (s/s)	B at R_{LC}	Visible Months	References
PSR B1937+21	1.55×10^{-3}	1.05×10^{19}	9.94×10^{5}	March-November	Abdo et al., 2013
PSR J0218+4232	2.32×10^{-3}	7.74×10^{20}	3.14×10^{5}	July-February	Abdo et al., 2013
PSR J1816+4510	3.19×10^{-3}	4.31×10^{20}	1.36×10^{5}	February-October	Kaplan et al., 2012
PSR J1311-3430	2.56×10^{-3}	2.10×10^{20}	1.28×10^{5}	December-June	Pletsch et al., 2012
PSR J0034-0534	1.87×10^{-3}	4.97×10^{21}	1.06×10^{5}	July-December	Abdo et al., 2013
PSR J1741+1351	3.74×10^{-3}	3.02×10^{20}	7.70×10^{4}	March-September	Abdo et al., 2013
PSR J2214+3000	3.11×10^{-3}	1.40×10^{20}	7.35×10^{4}	May-December	Abdo et al., 2013
PSR J2043+1711	2.38×10^{-3}	5.24×10^{21}	6.40×10^{4}	April-November	Abdo et al., 2013
PSR J2017+0603	2.89×10^{-3}	8.30×10^{21}	5.94×10^{4}	May-November	Abdo et al., 2013
PSR J0613-0200	3.06×10^{-3}	9.59×10^{21}	5.93×10^{4}	September-March	Abdo et al., 2013
PSR J1544+4937	2.15×10^{-3}	2.93×10^{21}	5.55×10^{4}	August-January	Bhattacharyya et al., 2013
PSR J0751+1807	3.47×10^{-3}	7.79×10^{21}	4.24×10^{4}	October-April	Abdo et al., 2013
PSR J1745+1017	2.65×10^{-3}	2.73×10^{21}	3.63×10^{4}	February-September	Barr et al., 2013
PSR J2302+4442	5.19×10^{-3}	1.33×10^{20}	2.78×10^{4}	June-January	Abdo et al., 2013
PSR J1640+2224	3.16×10^{-3}	2.83×10^{21}	2.08×10^{4}	February-September	Abdo et al., 2013
PSR J1713+0747	4.57×10^{-3}	8.53×10^{21}	1.92×10^{4}	February-September	Abdo et al., 2013
PSR J0030+0451	4.86×10^{-3}	1.02×10^{20}	1.80×10^{4}	July-January	Abdo et al., 2013
PSR J2317+1439	3.44×10^{-3}	2.42×10^{21}	1.75×10^{4}	June-January	Desvignes et al., 2016

TABLE 5.1: List of MSP sources visible at the MAGIC site

The results were plotted in Figure 5.1 also shows that J0218 is one of the best MSP candidates for the MAGIC site. PSR B1937+21 was excluded because it is located at the galactic plane, and signal detection could cause some complications compared to J0218.

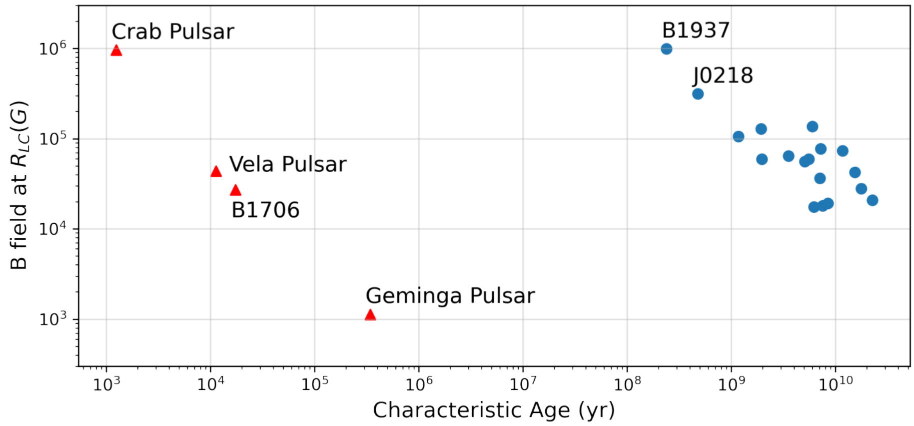

FIGURE 5.1: Magnetic field strength at the light cylinder radius vs. characteristic age of the millisecond pulsar candidates (see Table 5.1.)

5.2 The Millisecond Pulsar PSRJ0218+4232

PSR J0218+4232 is a millisecond pulsar in a binary system with two days of orbital period. The companion star is a white dwarf.The source is located at three kpc away. The first discovery in the radio band reported by (Navarro et al., 1995). The source has an unusual feature in which almost 65 percent of the emission is not pulsed in radio and X-rays (see Figure 5.2 a, b and c). It has been thought that the source is a nearly aligned rotator. PSR J0218+4232 is the first millisecond pulsar shows hints in gamma-rays by EGRET (Kuiper et al., 2000) (see Figure 5.2 e).It is one of the first millisecond pulsars detected by Fermi-LAT (Abdo et al., 2013). Some hints of VHE emission were discussed in (Fidalgo, 2019) (Saz Parkinson et al., 2017).

In the 2005-2006 period, the source had been observed by MAGIC-I telescope in mono mode(Anderhub et al., 2010). The observations were carried out by ON-OFF mode in which the source was pointed in the ON mode while a nearby dark patch was pointed in OFF mode for gamma-hadron separation. 20h of good quality data were collected. No significant pulsed emission was detected (see Figure 5.3).

5.3 MAGIC Observations 2018-2019

Since the performance of the system was upgraded by stereoscopic observations, PSR J0218+4232 was observed for the first time with the MAGIC Telescopes in Stereoscopic mode during November 2018 - November 2019. About 90h of good quality data were collected. The observations were carried out with standard wobble configuration(see Chapter 3) which the source was observed with 0.4 degrees offset.The wobble configuration is shown in Figure 5.17.

Zenith angle distribution varied between 13 to 35 degrees, and the data was taken with Sum-Tigger-II configuration, as explained in Chapter 3.

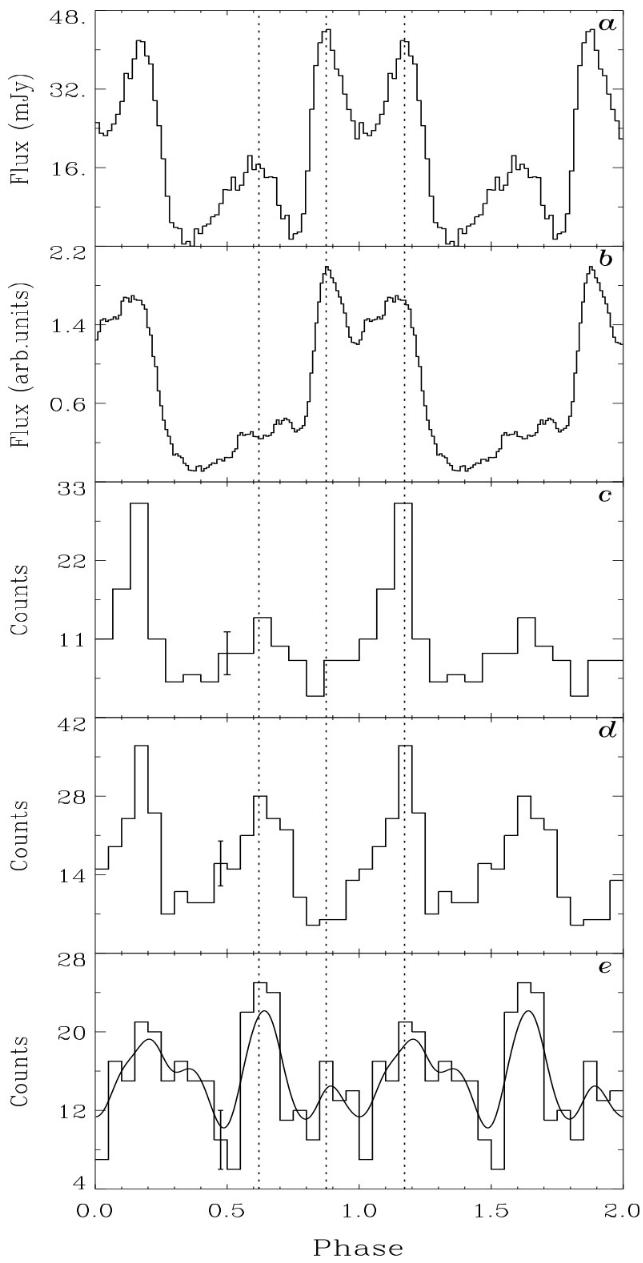

FIGURE 5.2: Pulse profiles of PSR J0218+4232 in radio, X-rays, and gamma-rays studied in (Kuiper et al., 2000). The first panel a) and b), shows radio pulse profiles at 610 MHz and 1410 MHz, respectively. c) and d) show X-ray pulse profiles recorded by ROSAT HRI at 0.1–2.4 keV and BeppoSAX MECS at 1.6–10 keV. Lastly, the gamma-ray pulse profile recorded by EGRET at 100–1000 MeV is shown.

5.4 Data Selection

Strict quality cuts for data selection are essential for analyzing faint sources like pulsars, particularly for detection purposes. Therefore, transmission cuts and detailed inspections for the data quality play a crucial role in the results. First, the data taken during the nights that the MAGIC LIDAR was not operating because of technical reasons were excluded. And then, a requirement of 0.85 transmission cut was set to preserve a significant portion of good quality data.

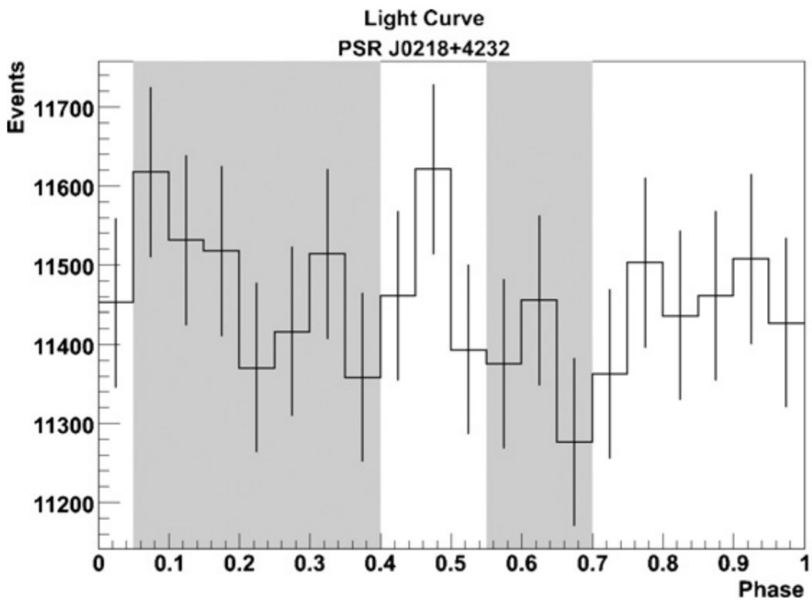

FIGURE 5.3: Pulsed emission search from J0218 by MAGIC-I telescope during 2006 October - 2007 January (Anderhub et al., 2010). Phaseogram was created for energies between 50 GeV - 300 GeV with a 120 GeV energy threshold. EGRET pulse peaks (see Figure 5.2, e) were used as on-pulse regions for the signal search, which is shown as shadowed area. There was no significant detection.

5.5 Data Reduction

The data were taken with the Sum-Trigger II system for optimizing the analysis energies below 100 GeV. Therefore, special cleaning and calibration processes were applied, called MaTaJu cleaning (see Chapter 3) for further details), therefore low-level analysis started from the RAW data level. Moreover, low energy-optimized dedicated Monte Carlo simulations were used. The data samples are shown in Table 5.2 used as background events for training RF. These OFF samples have similar ZA distribution and the same quality cuts. Those OFF data were taken with Sum-Trigger II, and the same cleaning and calibration were applied. Although the Geminga pulsar has been detected with 6.3 sigmas by the MAGIC Telescopes recently (MAGIC Collaboration et al., 2020), the data sample used for the detection was about 80 hours, and dedicated barycentric corrections were applied for studying pulsed emission. For the data sample we used as background events, the overall gamma-ray excess does not exceed one sigma significance and only four hours of data is used as background, and gamma-hadron separation was not affected by the detected pulsed emission.

TABLE 5.2: Data used as background sample for training Random Forest for J0218 Analysis

Source	Date
Geminga	2018-11-18, 2018-12-04, 2018-12-13, 2019-01-09, 2019-01-12, 2019-01-14,

The standard trigger MAGIC analysis has a threshold of 50 GeV for low zenith angle observations for the Crab Nebula (Aleksić et al., 2016). On the other hand, we achieved a 20 GeV threshold for low zenith angle observations for -4.5 spectral index source by using Sum-Trigger-II trigger system and dedicated analysis (see Figure 5.4).

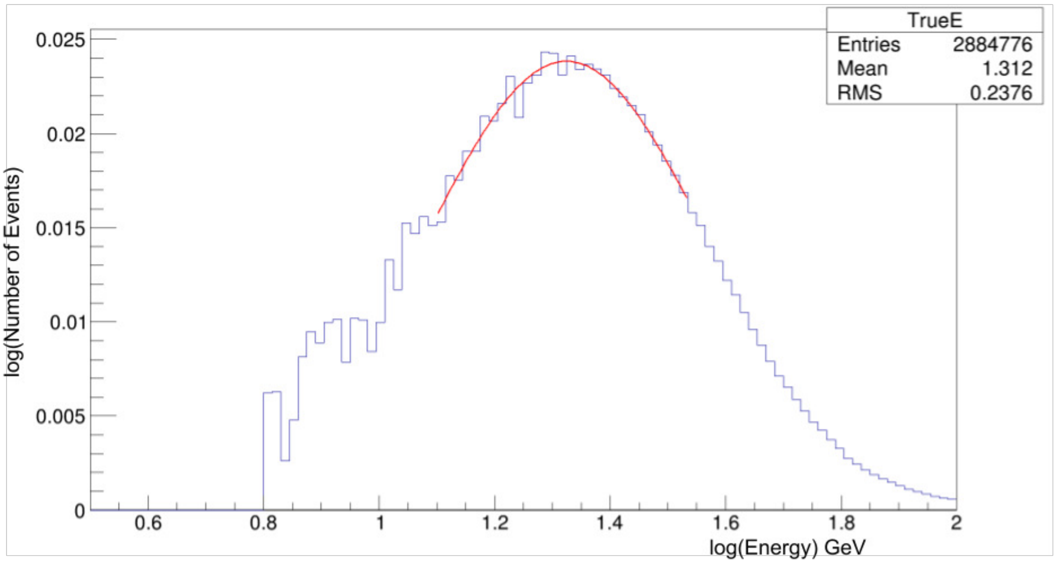

FIGURE 5.4: The minimum energy threshold was calculated for the analysis using a sample of test Monte Carlo simulations. The x-axis represents the logarithm of estimated energy in GeV, and the y axis represents the logarithm of the number of simulated events. The same data selection processes were applied to this simulated data set, and the energy threshold was calculated by estimating the peak of the data distribution, which refers to 20 GeV for this particular analysis.

5.6 The Crab Nebula Sanity Check

A sanity check was performed to check the performance of the analysis. For this purpose, the same trigger system was used, and data reduction was applied to the Crab Nebula. The spectrum of Crab Nebula (see Figure 5.5) has a lower energy threshold compared to the standard trigger results(see Chapter 3). The results are compatible with published Crab Nebula flux levels.

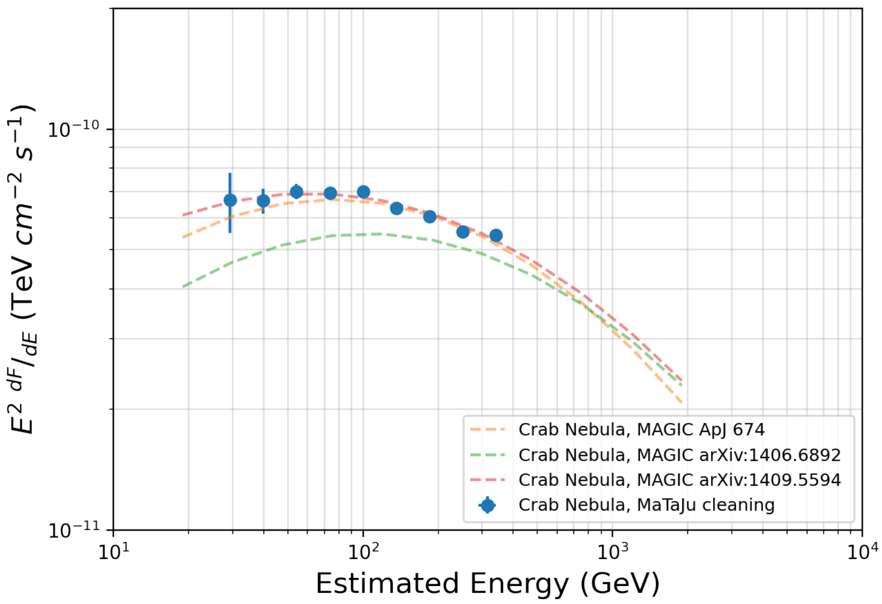

FIGURE 5.5: A test was carried out using the standard candle, Crab Nebula, to check the PSR J0218+4232 analysis performance.

5.7 Background Subtraction

Usually, the background events are subtracted from the off-phase region for the MAGIC analysis. For this source, we have used a new background subtraction method both for the phaseogram and the spectral analysis due to the following facts: possible un-pulsed emission (see section 5.2) and large on-phase in Fermi-LAT phaseogram (5.6).

Therefore, instead of subtracting the background events from the off-phase, we used three different source-free FoV regions for collecting the background events (see Figure 5.7). The distribution of the angular distance square both for the signal region and the background can be seen in Figure 5.8.

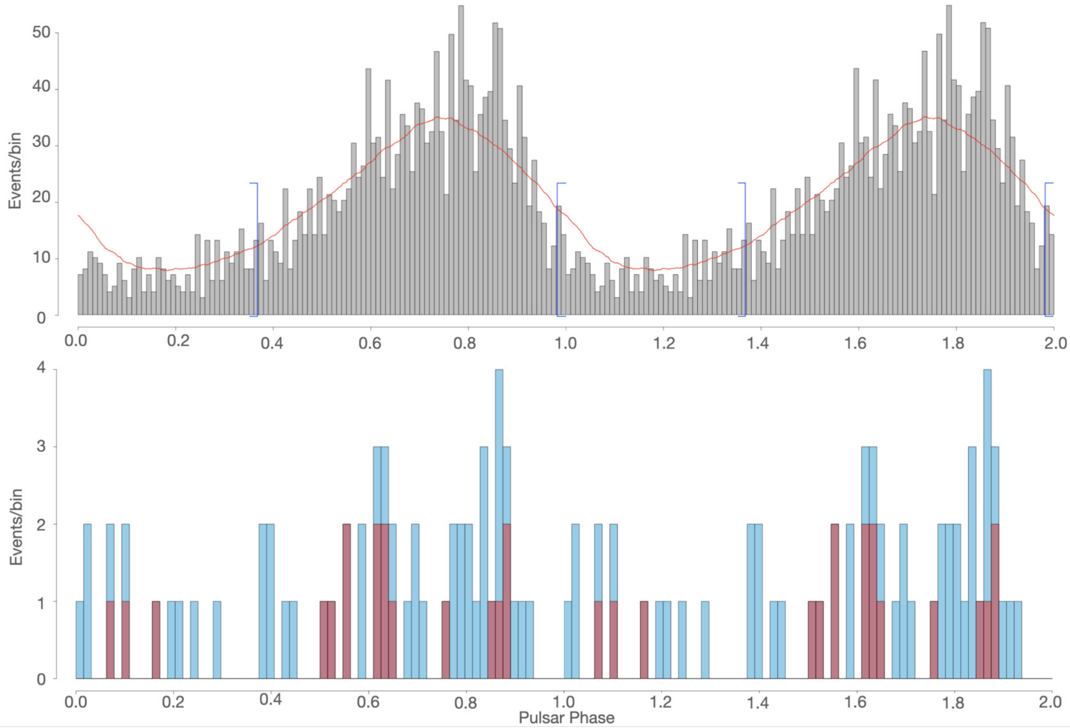

FIGURE 5.6: Fermi-LAT phaseogram created using 11.5 years of data (Acciari et al., 2021). The thick black line refers to 1-10 GeV events, while blue and pink histograms show events above 10 GeV and 25 GeV, respectively. The off-pulse region is shown as the grey shaded area [0–0.34)U(0.98,1].

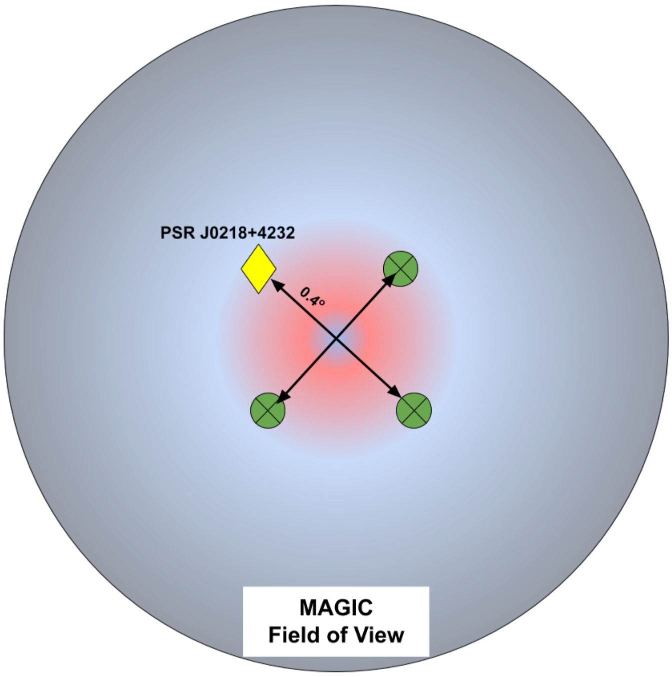

FIGURE 5.7: MAGIC camera FoV configuration for the J0218 and 3C66a/B observations. The source was pointed 0.4 degrees away from the camera center, which is so-called wobble mode observations. The source is represented as a yellow diamond. We used three different source-free FoV regions 0.4 degrees away from the camera center for the background subtraction. Those regions are represented as green circles.

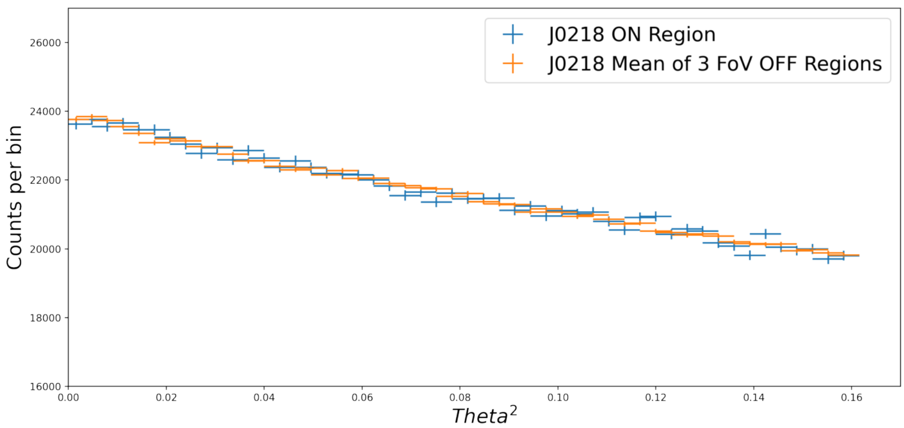

FIGURE 5.8: *Theta*^{2} distribution of the events from the PSR J0218+4232 position is represented by the orange data points. On the other hand, the blue data points refer to the *theta*^{2} distribution of events collected from the three different fields of view positions. Those events were averaged and phase-normalized for the PSR J0218+4232 on-pulse defined in Fermi-LAT phaseogram 5.6)

5.8 Results

The MAGIC results shown in this section were obtained by the author. The total amount of data is 90 hours.

VHE emission search between 20GeV to 200 GeV is performed both for checking pulsed and un-pulsed emissions (see Figure 5.9). Rotational phases of the pulsar were computed with Tempo2 package (Hobbs, Edwards, and Manchester, 2006) using the timing parameters reported in (Acciari et al., 2021). The off-pulse region was estimated by using 11.5 years of Fermi-LAT data and a non-parametric SOPIE (Sequential Off-Pulse Interval Estimation) package (Schutte and Swanepoel, 2016). For the On-pulse region was defined as 0.34 to 0.98 pulse interval while the rest was assigned as OFF-pulse region (Acciari et al., 2021). For the pulsed emission search, region independent signal tests were applied, H-test, Z^2_{10}, and no pulsation is detected 5.3.

Moreover, the significance of the excess events was computed in the ON-phase region by using the Li & Ma formula (Li and Ma, 1983). The ON-pulse region is so broad that the OFF-pulse region provides low statistics for background calculations, which are indicated as yellow and grey-dashed regions in Figure 5.9. Therefore, the background events were computed from three different and source-free FoV regions, which have the same distance to the camera center as J0218. The mean value of the normalized number of OFF events and the error is plotted as the purple band in Figure 5.9. The significance of the excess events calculated for the phaseogram in Figure 5.9 is 0.05 σ, we therefore have not found evidence of pulsed emission (see Table 5.3. In addition, signal region independent tests ((Mochol and Petri, 2015) were performed to search for a signal, and they were also compatible with no pulsed emission signal.

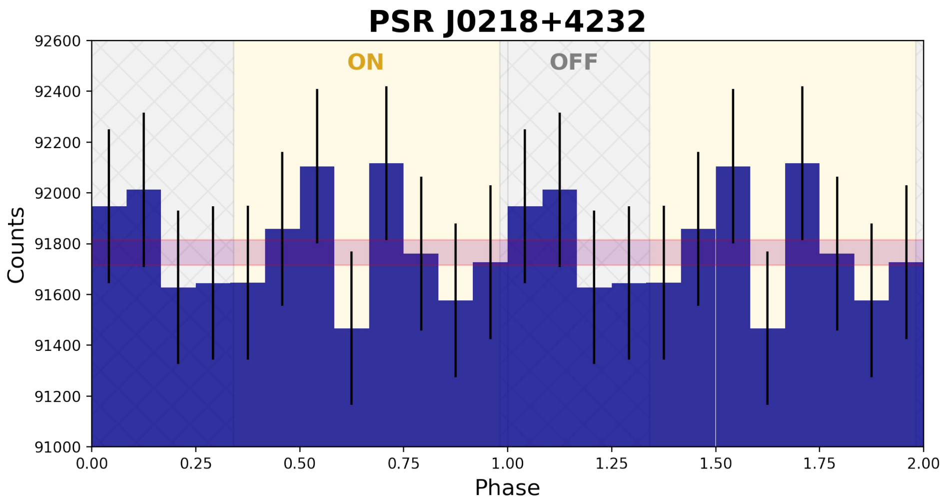

FIGURE 5.9: Search for VHE pulsations of PSRJ0218+4232 by using MAGIC analysis in this work. The solid blue histogram represents events of 20-200 GeV collected from the FoV on region. Besides, the purple vertical area refers to the events collected from three FoV background regions. The gold and grey-dashed areas refer to the on-pulse signal and the off-pulse regions, respectively. No significant pulsation was detected (see Table 5.3).

Additionally, smaller energy bins were used for possible pulsed emission checks of the source in Figure 5.10 , and no pulsed emission was detected.

TABLE 5.3: MAGIC Pulsed emission Signal Test Results

Tests	Results
Li&Ma(Eq.17)	0.05σ (Excess: 22.2$\pm$387.75)
$\chi 2/\mathrm{ndf}$	5.54/11
H-test	0.05
Z^2_{10}	13.13

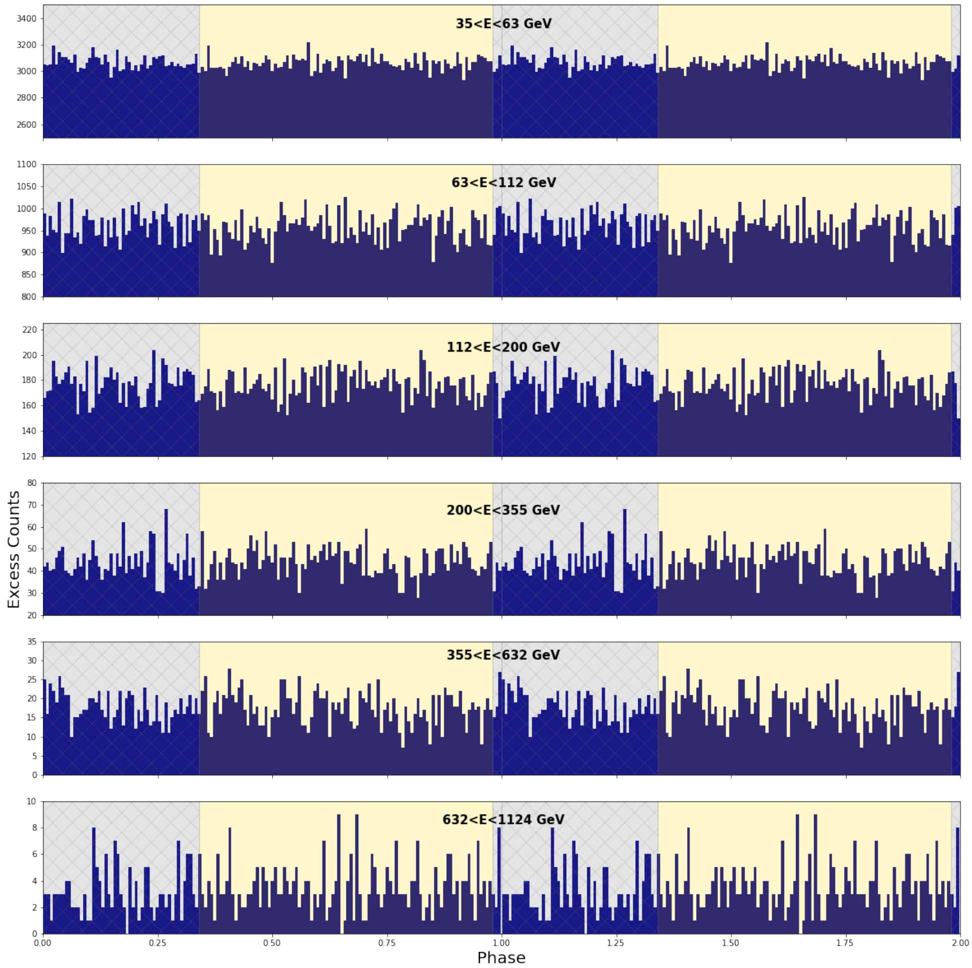

FIGURE 5.10: VHE pulsations searched for smaller energy binning samples using the PSR J0218+4232 analysis. The solid blue histogram represents events for different energy ranges. No significant pulsation was detected.

Spectral analysis of J0218 was performed with the same method used for phaseogram, in which the background subtraction was performed using the three FoV background regions mentioned above. Upper limits (UL) were set on the pulsed emission a 95 % confidence level (Rolke and López, 2001), assuming a Gaussian systematic uncertainty in the overall signal efficiency of 30 % standard deviation (see Figure 5.11). The blue points and ULs represent Fermi results published in (Abdo et al., 2013), and the orange ULs represents this work. UL points can be seen in Table 5.4

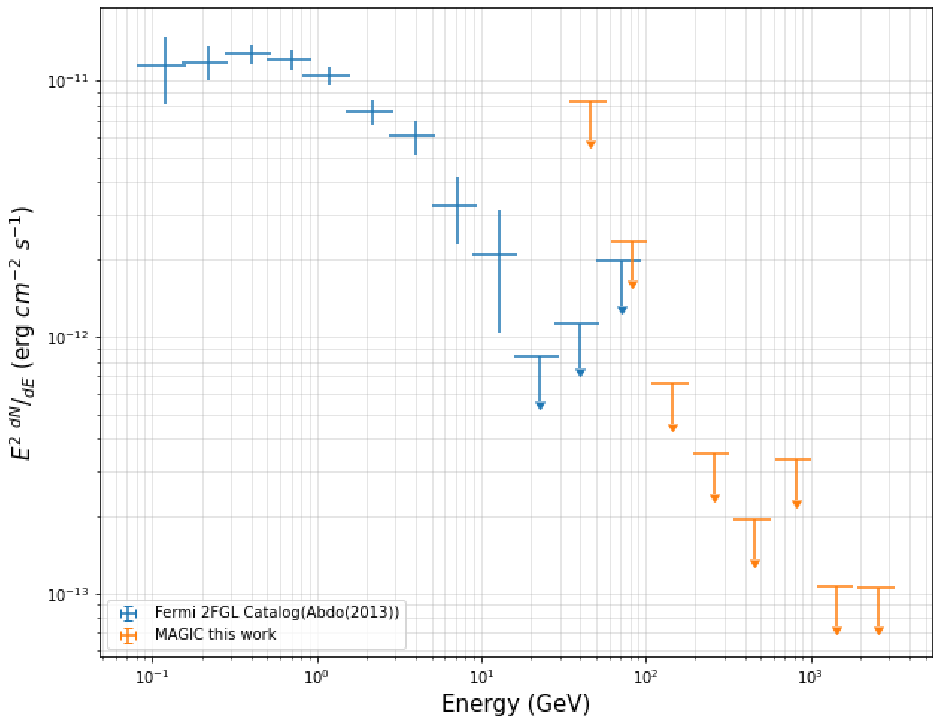

FIGURE 5.11: Spectral energy distribution of PSRJ0218+4232. In blue, Fermi-LAT measurements (adapted from (Abdo et al., 2013)) are shown. In orange, the upper limits obtained with MAGIC in this work are shown. The ON-pulse region was used [0.34,0.98] for both of the analysis.

Bin Center (GeV)	**On pulse** $E^2dN/dEdAdt$ $[TeV cm^{-2}s^{-1}]$ $x10^{-12}$
45	8.3
81	2.3
145	0.7
258	0.4
459	0.2
816	0.3
1452	0.1
2583	0.1

TABLE 5.4: SED Upper Limits of PSR J0218+4232

In addition to the pulsed emission search, we also investigated possible DC emissions by using all the data without any phase-cut. Excess plots in Figure 5.13 do not show any significant gamma-ray emission.

We also checked the skymap of the source, see Figure 5.12. No significant excess was detected from the source. However, a significant gamma-ray emission was detected from the 3C66A/B region, and thanks to the good PSF of the MAGIC Telescopes, the blazar did not contaminate the J0218 analysis. A dedicated analysis will be presented in the following sections.

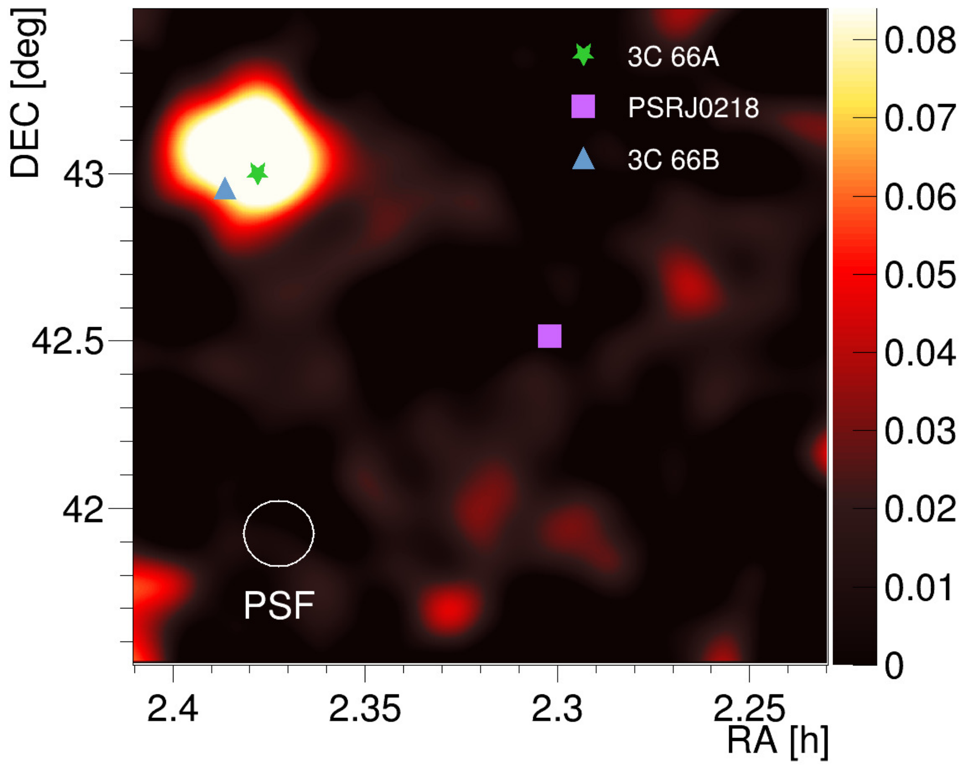

FIGURE 5.12: MAGIC relative flux map of the region around PSR J0218+4232 (indicated by a purple square). Although no VHE emission was detected from J0218, 3C66A (green cross), was detected with significance above 5σ.

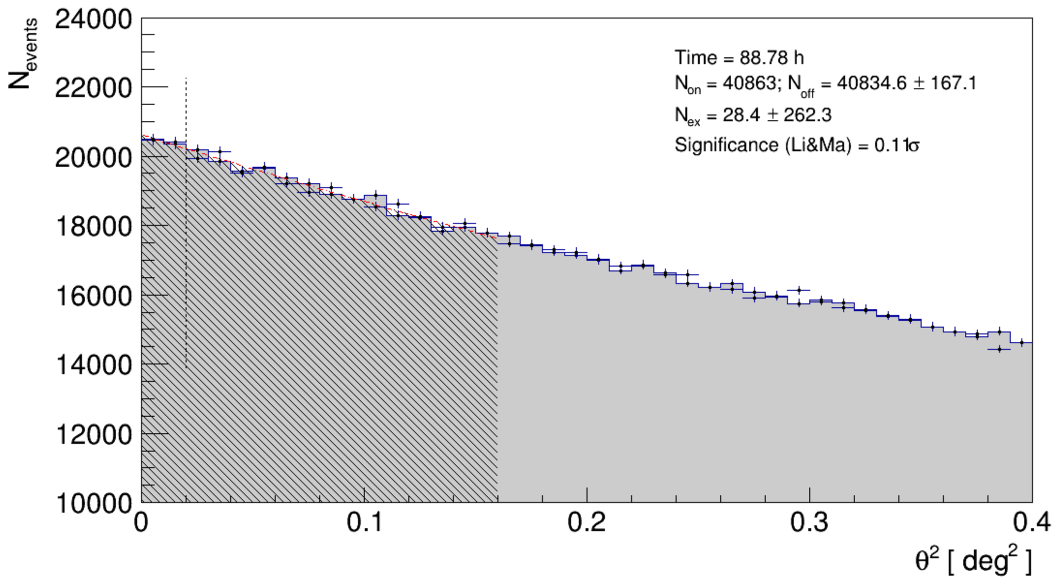

FIGURE 5.13: Angular distribution of the events for PSR J0218+4232 without any phase cut. Three source-free FoV regions used for the background subtraction. No un-pulsed emission is detected.

5.9 The Blazar 3C66A

3C66A is an intermediate BL Lac object (see Figure 5.14) which is less than 1 degree away from J0218. It is one of the first observed IBL Lac objects detected at TeV energies. The latest redshift results estimated the value of 0.34 (Torres-Zafra et al., 2018). Moreover, there is a radio galaxy called 3C66B only 0.12 degrees away.

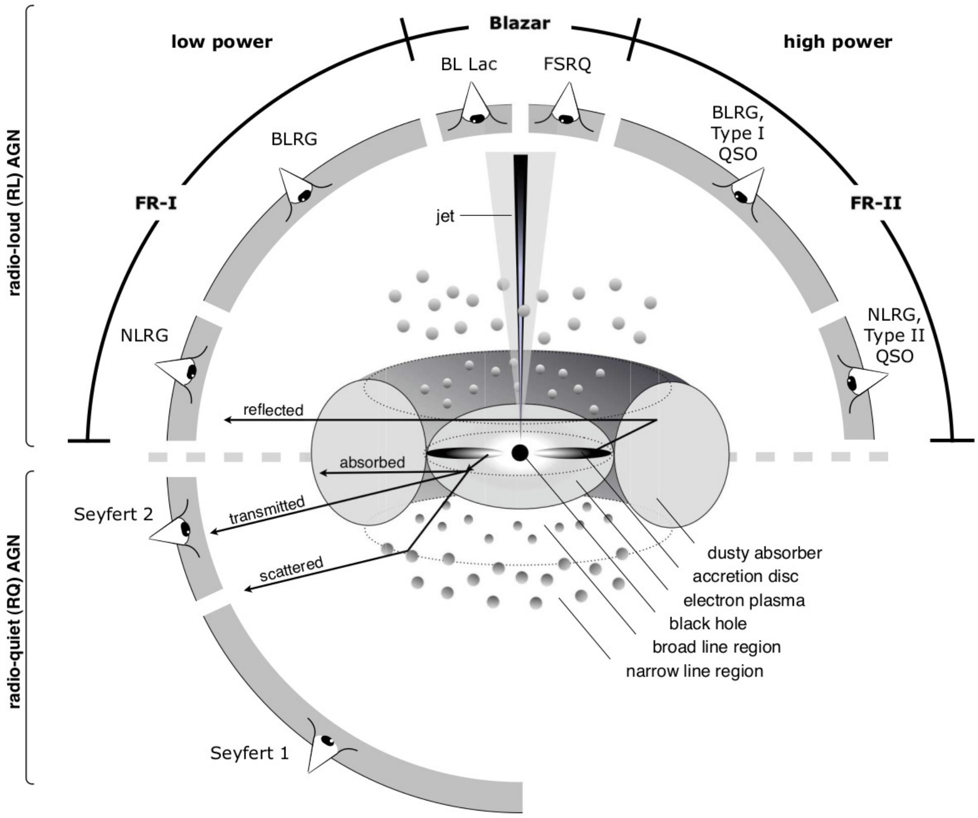

FIGURE 5.14: Schematic representation of the AGN types (Beckmann and Shrader, 2012). They are classified according to our viewing angle, the power of the central black hole, and its jet. Blazars are the type of AGNs that VHE gamma-ray emission can be observed because our viewing angle allows us to observe the jets directly.

The separation of 3C66A and the J0218 sources had been a problem when gamma-ray emission were detected by EGRET (see the left panel in Figure 5.15). For the first time, a 3.5 sigma separation was announced (Kuiper et al., 2000). The separation of the two sources improved with Fermi analysis (Abdo et al., 2011) (see the right panel in Figure 5.15).

In addition, VERITAS has detected the 3C66A both in flare and dark-run period (Aleksić et al., 2011a). The 14h of flare data taken in 2007 September 2008 January, while the 33h of dark run data taken in 2008 September 2008 November. Both spectra were nearly identical with photon indices of 4.1 $\pm$ 1.2 (see Figure 5.16). The integral flux above 200 GeV for the flare period was reported as (2.5 $\pm$ 0.4) x $10^{-11} cm^{-2} s^{-1}$, while the average flux for the dark run period was (1.4 $\pm$ 0.2) x $10^{-11} cm^{-2} s^{-1}$.

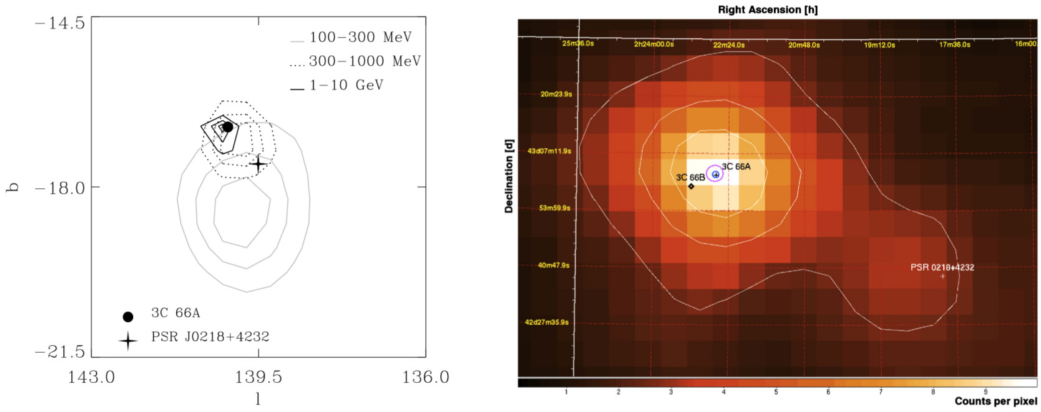

FIGURE 5.15: Skymaps of PSR J0218+4232 and 3C66A. EGRET Map of these two sources is shown on the left-hand side(Kuiper et al., 2000). The contours represent the peak of emission with 1,2,3 σ contours for different energy ranges. Besides, Fermi-LAT skymap (Abdo et al., 2011) is shown on the right-hand side with a better resolution than the EGRET map. The region of two blazars 3C66A/B, and the PSR J0218+4232 can be seen separately. The contour levels refer to 2.8, 5.2, and 7.6 counts per pixel.

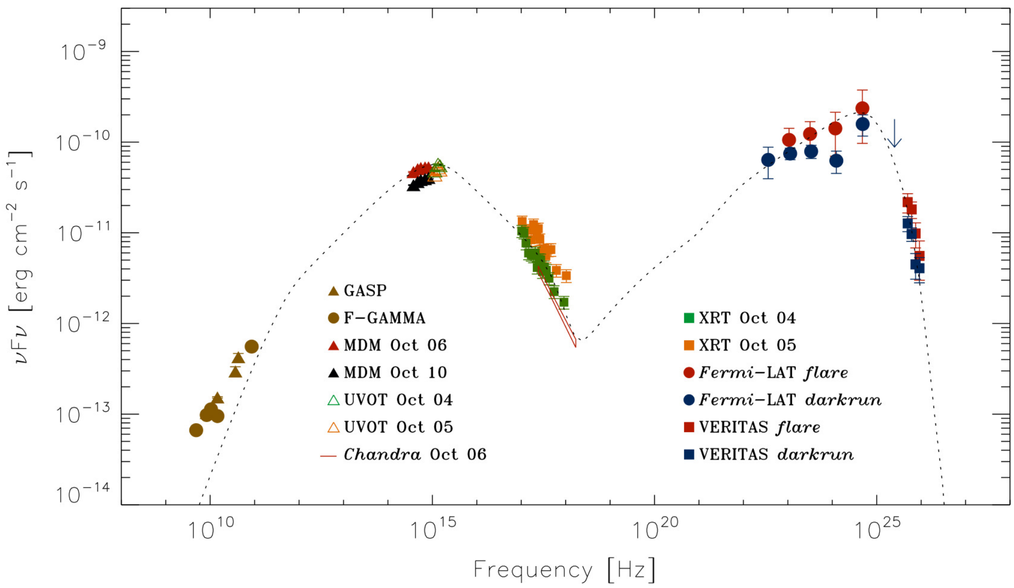

FIGURE 5.16: Broadband spectral energy distribution of 3C 66A during the 2008 October multi-wavelength campaign (Abdo et al., 2011). Each observations data sets were mentioned in the legend. A reference theoretical model created by the EBL-absorbed EC+SSC model for z = 0.3 was plotted as dashed lines.

5.9.1 Data Selection

The 3C66A analysis focused on energies up to 700 GeV, and the source is more luminous compared to J0218. The same data set used for the J0218 which refers to 90h of good quality data.

5.9.2 Data Reduction

Because the 3C66A IBL Lac source is already reported up to TeV energies, instead of optimizing the analysis for lower energies like performed for MSP, we used standard cleaning and calibration as mentioned in Chapter 3. Apart from the cleaning and calibration methods, the same data reduction processes of J0218 was applied for this analysis.

Off-Axis Analysis

Due to the fact that the MAGIC observations were performed with targeting J0218, 3C66A did not have a fixed offset from the FoV center for different Wobble positions (see Figure 5.17). For the W1, the distance between the camera center and 3C66A was 0.84 degrees, while for W2, 1.22 degrees, and for W3, 0.66 degrees, for W4, 1.33 degrees.

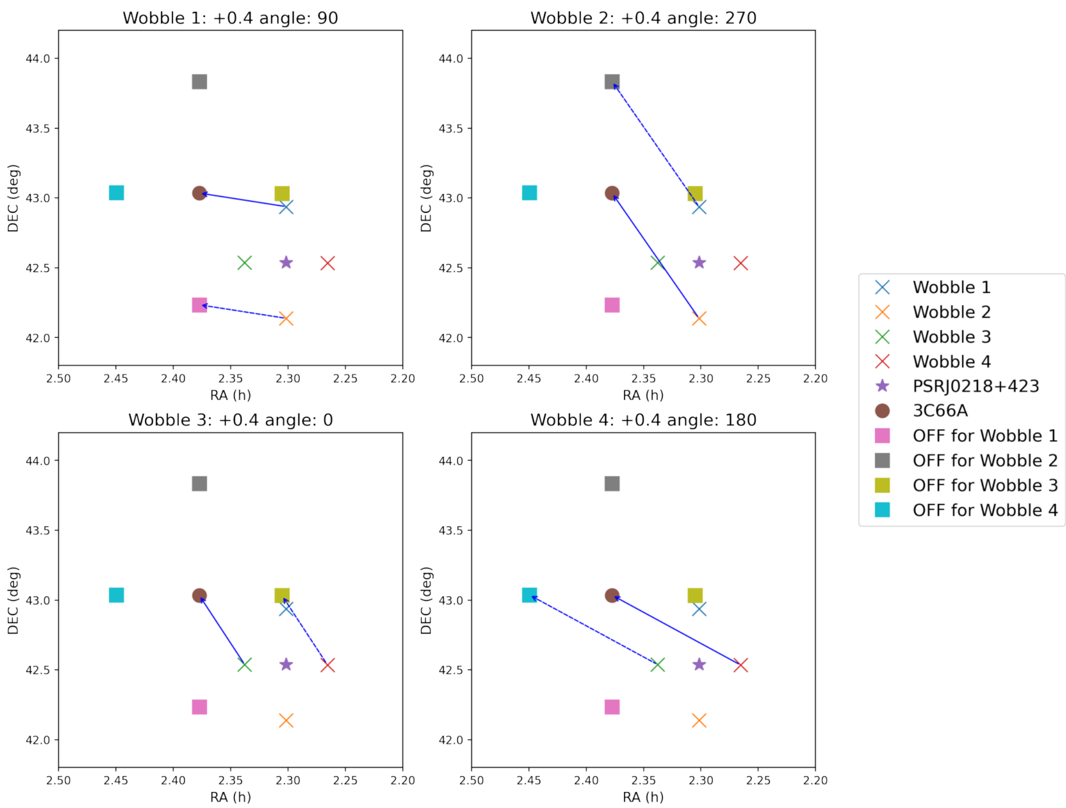

FIGURE 5.17: The configuration of PSRJ0218+4232 (purple star) observations by MAGIC in Wobble mode. The FoV center pointed 0.4 degrees away from the source, called W3 (green x), and then pointed to a new position opposite to W1 with respect to the source called W4 (red x). Afterward, the FoV center pointed to two other wobble positions, perpendicular to the W3-W4 pair called W1 (turquoise x) and W2 (orange x). The 3C66A is indicated as a brown circle. Because the observations are wobbling around PSRJ0218+4232, standard usage of "simultaneous off" regions can not cover the same sectors of the camera as 3C66A in different wobbles. Therefore we applied off from the wobble partner method. The OFF regions(represented as squares) are taken from the Wobble partners, which spends about the same time in about the same sectors of cameras as 3C66A does.

A sanity check for the performance of the analysis is shown in Figure 5.18. Crab Nebula samples for the test were selected from the same observation period as mentioned above. The observations were carried out with the Sum-Trigger-II configuration system such as 3C66a, standard cleaning and calibration were applied, and the same Random Forests were used. The results are compatible with published Crab Nebula flux levels.

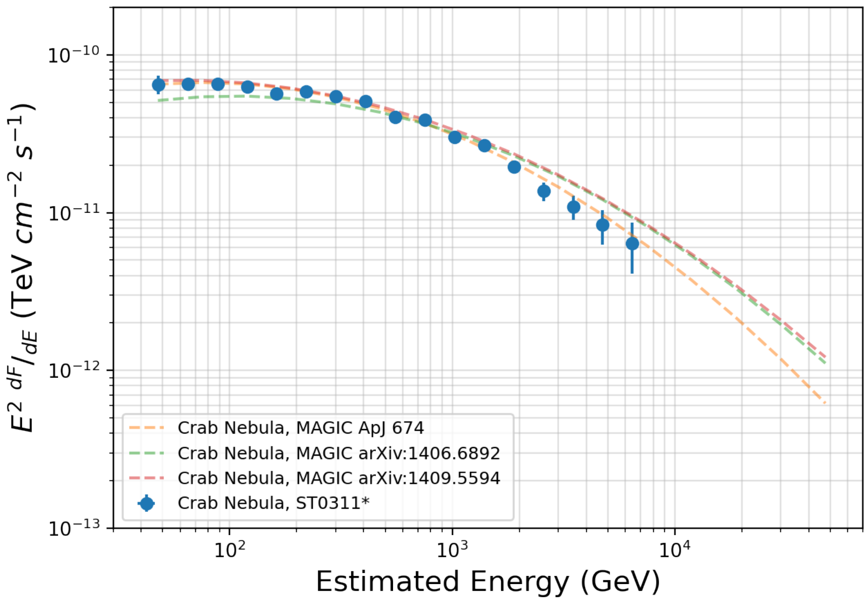

FIGURE 5.18: A test was carried out using the standard candle, Crab Nebula, to check the 3C66A analysis performance. The results are compatible with the previously published spectral shape of the Crab Nebula, which indicates that the analysis performed successfully.

5.9.3 Results

For these results, 90 hours of data were used in total.

The significance of gamma-ray rates was checked for each night, and for one night (27.09.2019), three times significance per square root of hours was detected compared to the other nights. Figure 5.19 shows the excess plot of the high flux night. The source was detected with more than six sigma in 2 hours. Figure 5.20 shows the excess plot of the rest of the data set excluded the high flux night. The source was detected above seven sigmas.

Analysis performed for this source was divided into two flux levels after these results. It will be called flare for the high flux night and non-flare for the rest of the data set.

We checked skymaps to understand the source of the emission. Figure 5.20 shows the skymap of the flare night and the non-flare nights. In both of the skymaps, the 3C66A is represented by the cross, and squares represent the nearby radio galaxy 3C66B.

Spectral analysis was performed with off from the wobble partner mode, as explained in the data reduction section. Spectral analysis was performed for flare and

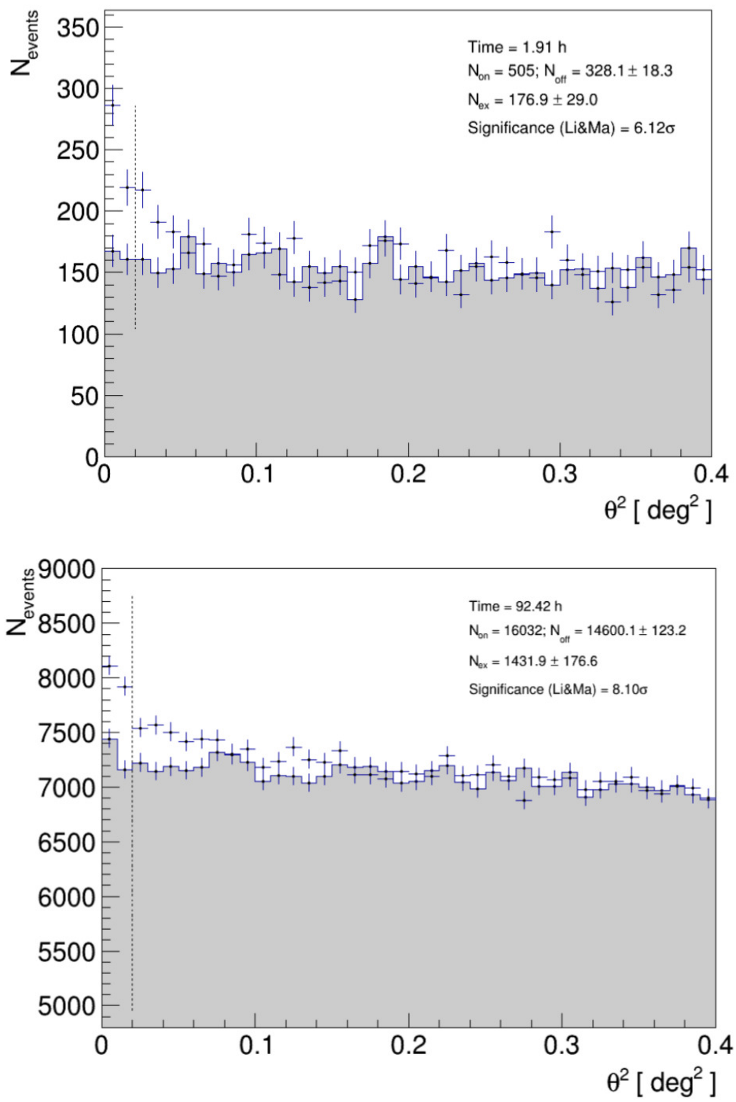

FIGURE 5.19: Angular distribution of the events for 3C66A for the flare (upper plot) and the non-flare (lower plot) phases. In both of the phases, the source is detected with a significance above 5σ

non-flare periods separately. The spectral flux levels were calculated for each analysis period and each wobble position to calculate the effective area with Flute 3. Afterward, spectra were combined with Foam Chapter 3. Forward folding for estimating the true energy and EBL correction and fitting was done with Fold explained in Chapter 3. The redshift 0.34 was used as reported in (Torres-Zafra et al., 2018).

In Figure 5.21, spectral analysis results are shown. The referenced Crab Nebula is represented with dashed lines. The observed integrated flux points can be seen in Table 5.5.

Absorbed spectral points are corrected with EBL correction of Dominguez model (Domıénguez et al., 2011) for redshift z=0.34 (Otero-Santos et al., 2020). The best-fitting function for the intrinsic spectra of flare and non-flare are power-law with the following expression, and the details of the fit results can be found in the Table 5.5.:

$$f_{E_0}(\frac{x}{E_0})^{\alpha} \tag{5.1}$$

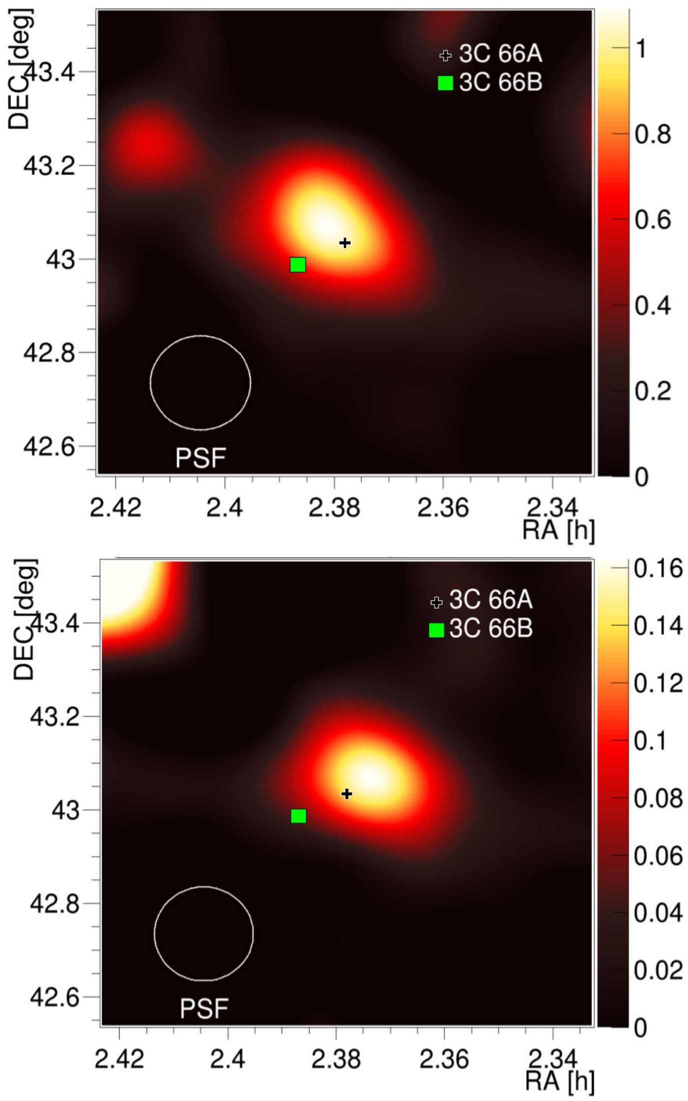

FIGURE 5.20: The skymap of the 3C66A region for flare (upper plot) and non-flare (lower plot) period.

Bin Center (GeV)	**High Flux** $E^2dN/dEdAdt$ $[TeVcm^{-2}s^{-1}]$ $x10^{-11}$	**Bin Center** (GeV)	**Low Flux** $E^2dN/dEdAdt$ $[TeVcm^{-2}s^{-1}]$ $x10^{-11}$
62	6.6 ± 1.8	53	1.1 ± 0.6
90	2.8 ± 0.9	78	0.9 ± 0.2
122	2.7 ± 0.6	111	0.3 ± 0.1
166	2 ± 0.5	155	1.5 ± 0.1
223	1.8 ± 0.4		
295	0.5 ± 0.3		
384	0.6 ± 0.3		

TABLE 5.5: Forward folded SED points of 3C66A

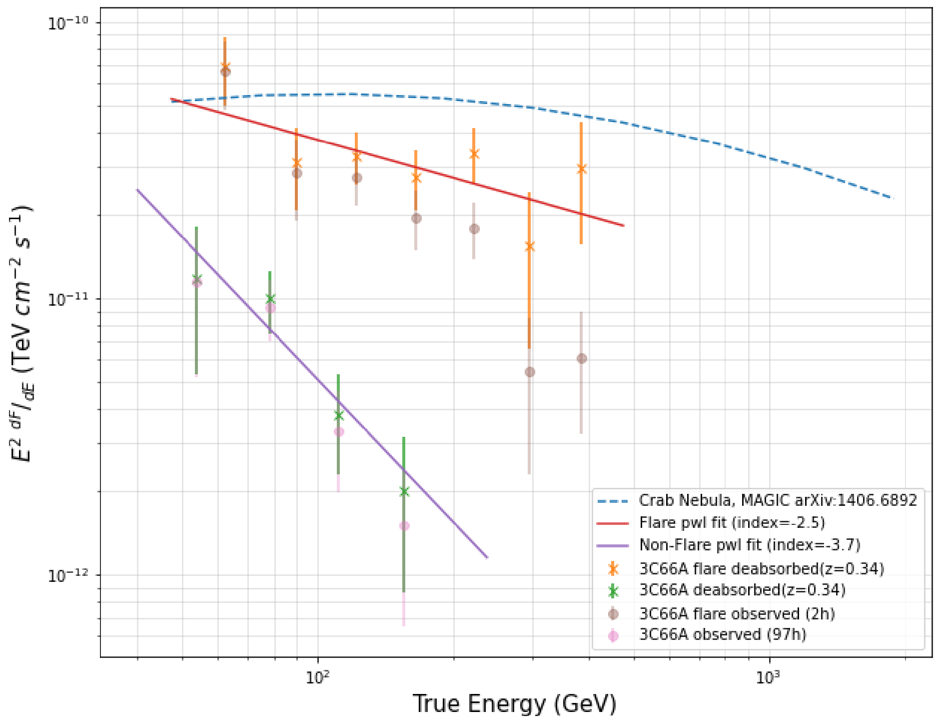

FIGURE 5.21: Forward folded and redshift corrected SED results of 3C66A. The brown data points represent the flare period forward folded SED, and the orange data points represent the de-absorbed SED points calculated for 0.34 redshift. Furthermore, the pink and green data points represent observed and de-absorbed SED, respectively. The flare and non-flare periods fitted by power-law function(see Table 5.6) with different spectral indexes which indicates to different physical emission processes.

	Redshift	E_0 (GeV)	f_{E_0} $TeV^{-1}cm^{-2}s^{-1}$	α	χ^2/dof
MAGIC (Aleksic 2011)	z=0.444	200	(9.6±2.5)x10^{-11}	3.6±0.4	
flare	z=0.34	150.36	(4±0.7)x10^{-10}	3.7±0.4	4.3/7
non-flare	z=0.34	106.44	(1.4±0.1)x10^{-9}	2.45±0.2	1.9/6

TABLE 5.6: Results of spectral fit to power-law function

Chapter 6

The Crab Pulsar with the MAGIC Telescopes

One of the most studied astrophysical objects is the Crab Nebula and the pulsar at its center. Because the Crab Nebula is a bright and generally stable source in VHE, ground-based gamma-ray observatories have been using as a standard candle. In addition to this, the Crab Pulsar is the first and the most studied pulsar detected at the VHE regime.

Firstly, this chapter aims to give background information on the Crab Pulsar and the studies carried out by the MAGIC Telescopes. Then, data analysis of the 2009-2019 period will be explained. Finally, the results will be presented, and VHE emission outcomes will be compared with the previously published results of the MAGIC Telescopes.

6.1 The Crab Pulsar studies with the MAGIC Telescopes

The Crab Pulsar, also known as PSR J0534+220, is a young pulsar with a 33ms spin period and 2kpc distance. It is one of the few pulsars which has been detected almost in all wavebands. Besides, it is the most powerful pulsar in our galaxy with 4.6 10^{38} erg s^{-1} spin-down luminosity, and the first pulsar detected with Cherenkov Telescopes (Aliu et al., 2008). With high luminosity, persistent pulsed emissions, and hints of radiation up to 1.5 TeV energies, the Crab pulsar has been one of the best sources for testing the pulsar emission models like the polar cap model (M. A. Ruderman and Sutherland, 1975)(Baring, 2004)(Daugherty and A. K. Harding, 1982), slot gap model (Arons and Scharlemann, 1979)(Alice K. Harding et al., 2008)(Muslimov and Alice K. Harding, 2004a), and outer gap model (Cheng, Ho, and M. Ruderman, 1986)(Hirotani, 2008)(Tang et al., 2008)- and has challenged them for giving rise to new models (Hirotani, 2011)(Lyutikov, Otte, and McCann, 2012)(Alice K. Harding and Kalapotharakos, 2015)(Aharonian, Bogovalov, and Khangulyan, 2012b)(Mochol and Petri, 2015) (see Chapter 1).

The MAGIC-I telescope started operation in 2004 using the standard mono trigger with an energy threshold of about 60 GeV. With that, upper limits were derived for pulsed gamma radiation from the Crab pulsar (Albert et al., 2008b). A new trigger system (mono sum trigger) was installed in 2007, which lowered the trigger threshold to about 25 GeV and led to the detection of pulsed gamma radiation from the Crab pulsar (Aliu et al., 2008). The relatively high energy cutoff in the phased average spectrum indicated that emission occurs far out in the magnetosphere, which excluded the polar cap model's relatively low cutoff prediction (Aliu et al., 2008).

After the MAGIC-II installation in 2009, the MAGIC telescopes have operated in stereoscopic mode with a standard trigger threshold of around 50 GeV.

Since then, the main pulse (P1) and interpulse (P2) of the Crab Pulsar had been studied. The energy spectra and a pulse profile analysis above 25 GeV for both the main pulse and the interpulse were reported for the first time (Aleksić et al., 2011b). The flux measured with the MAGIC Telescopes was significantly higher than the exponential cutoff spectrum's extrapolation determined by Fermi-LAT (Aleksić et al., 2011b). VHE spectra of both peaks between 50-400 GeV were studied in (Aleksić et al., 2011b) , (Aleksić et al., 2012). The VHE emission was interpreted as an additional component produced by the inverse Compton scattering (Aleksić et al., 2012). Bridge emission between the main pulse and interpulse above 50 GeV was detected (Aleksić et al., 2014).

Lastly, the hint of TeV pulsed emission was detected from the source, making it the most compact TeV accelerator known and corresponds to electron acceleration to TeV-emitting energies near or beyond the light cylinder. This emission implied that an Inverse Compton(IC) process is the dominant emission mechanism for gamma rays above 50 GeV (Ansoldi et al., 2016) (see Figure 6.1 and Figure 6.2)

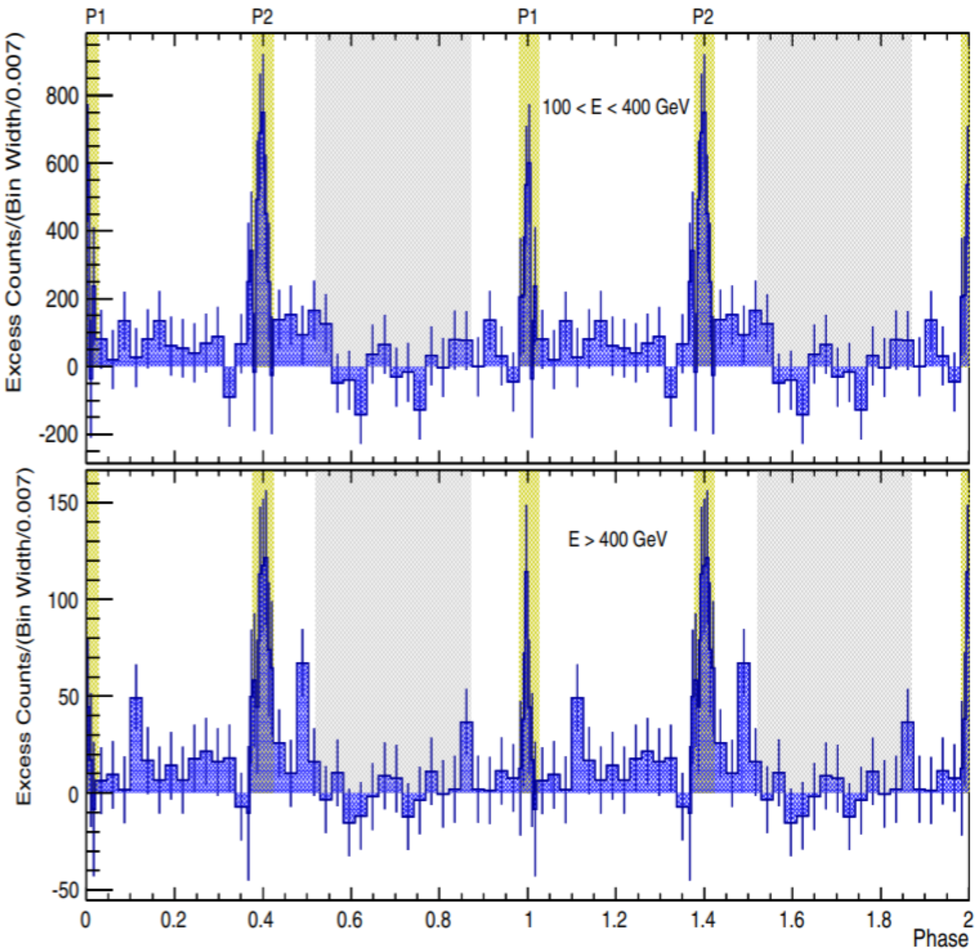

FIGURE 6.1: The Crab Pulsar phaseograms between 100-400 GeV and above 400 GeV (Ansoldi et al., 2016)

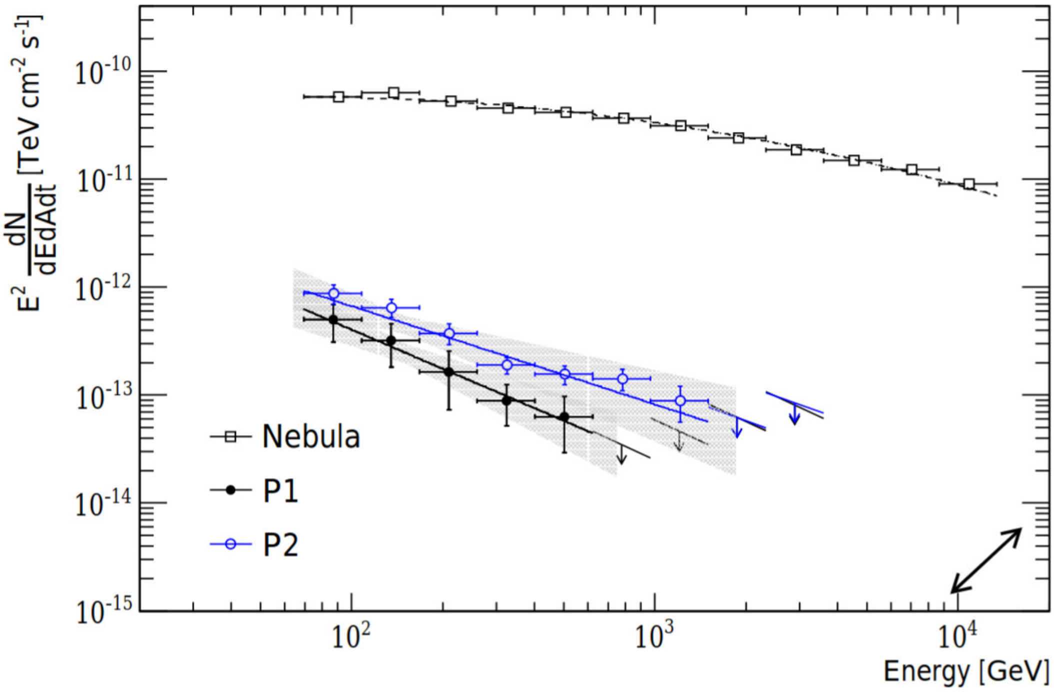

FIGURE 6.2: Phase-folded spectra of the Crab Pulsar. Black circles represent the Crab Pulsar peak 1, while the blue circles show the Crab Pulsar peak 2 by MAGIC Telescopes between 70GeV - 1.5 TeV. Besides, the Crab Nebula spectrum is shown as open circles. The upper limits are computed for 95 % CL with assuming power-law spectrum (see Table 6.3 for the fit parameters published in (Ansoldi et al., 2016))

6.2 The Magic Observations in Stereoscopic Mode

The Crab Nebula observations have been performed periodically to test the performance of the system and the scientific study of the source since the MAGIC Telescopes were built in 2004. For this study, we will only use the data taken with stereoscopic mode, which has better sensitivity and energy resolution than the mono mode (Aleksić et al., 2016). There are two primary samples used in this work. The first sample belongs to 2009 to 2014 data, and the low-level analyses are performed by Daniel Galindo (Galindo Fernández, 2018). Lastly, the 2014 to 2019 sample will be presented, which was analyzed by the author of this thesis.

6.2.1 2009-2014

This period was firstly analyzed by Daniel Galindo (Galindo Fernández, 2018). This 221 hours of stereoscopic data set were used for the TeV emission study (Ansoldi et al., 2016) as well as additional 100h data taken with only the MAGIC-I. For this thesis, the stereo data re-analysis started from the medium-level event lists. Additionally, a bug fix in the stereoscopically reconstructed shower parameters was applied by the author of the thesis, which will be explained in the following subsection.

Correction of the Energy Miscalibration

For this data set, a bug for calculating the stereoscopically reconstructed energy was found and fixed. The reconstracted energies were sometimes overestimated compared to the parameters estimated by each telescope independently. Figure 6.3 shows the effect of the bug on this data set for the Crab Pulsar.

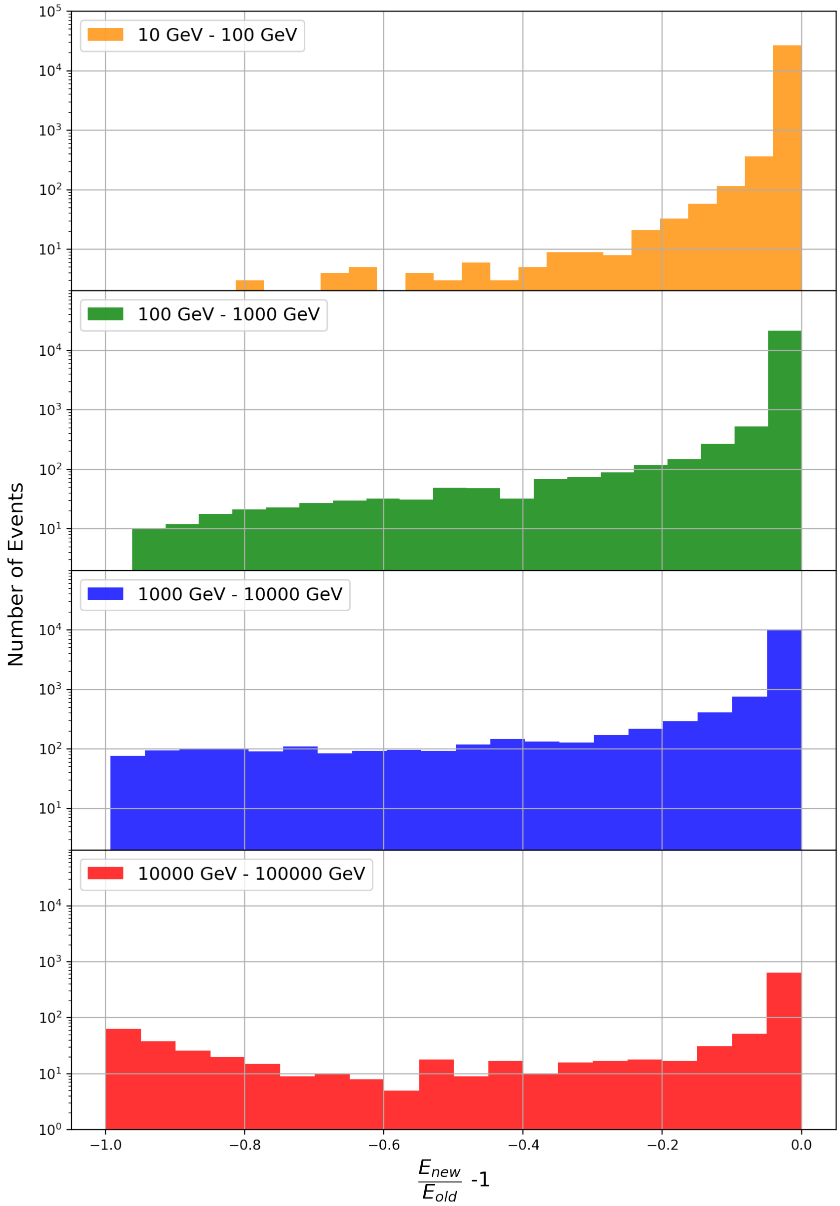

FIGURE 6.3: The energy reconstruction algorithm bug fix for 2014-2019 data sample for the Crab Pulsar. The data was separated into different energy ranges from the upper panel to the lower one, 10-100 GeV, 100-1000GeV, 1000-10000 GeV, 10000-100000 GeV, respectively. While the x-axis representing the number of events, the y-axis shows the fraction of the stereoscopically reconstructed shower parameters to the miscalculated results. The parameters were overestimated compared to the correct values.

6.2.2 2014-2019

This section will be dedicated to the analysis carried out for this work by the author of the thesis. The data used in this data set includes only the standard trigger configuration. The details of the data reduction and the results will be discussed in the following sections.

6.3 Data Selection for 2014-2019 data

As discussed in the previous chapter, weak source analysis as pulsars requires strict data quality cuts. 0.85 Transmission cuts were applied for this analysis. Moreover, the days that the MAGIC LIDAR was not operating due to technical problems were excluded.

The data taken in the dates between 2017.08.02 - 2017.11.02 (ST.03.08) and 2018.06.30 - 2018.10.30 (ST.03.10) (see Table 3.3) were excluded due to the bad weather conditions. There was a gradual decrease in mirror reflectivity for those days and resulted in insufficient data quality. The data in the first period was affected by a strong Calima, and the quality of the data was not fulfilling the needs of pulsar analysis. On the other hand, the latter period of data was affected by a storm, and some hardware problems arose during that period.

The data used after the quality cuts can be seen in Table 6.1 with a total amount of 124 hours of good quality of the sample.

Date	Period	Zenith Angle bin (deg)	Effective Time (h)
2014.11.24 - 2016.04.28	ST.03.06	05-35	30.5
		35-50	4.2
		50-70	21
2016.04.29 - 2017.08.02	ST.03.07	05-35	21.1
2017.11.10 - 2018.06.29		35-50	11.4
		50-70	4.8
2018.11.01 - 2019.09.15	ST.03.11	05-35	8.1
		35-50	6.71
		50-70	0.4
2019.09.16 - 2019.12.10	ST.03.12	05-35	9.4
		35-50	4.71
		50-70	1.8
Total:			124 h

TABLE 6.1: The Table of the Crab Pulsar Data Analysed in this work

6.4 Data Reduction for the 2014-2019 data

The data set was divided into twelve subsamples and analyzed independently. Each subsample was separated according to the analysis periods and zenith angle periods specified in Table 6.1. For each subsample, the data samples mentioned in Table 6.2 used for the RF training were carefully selected. The gamma-ray detection did not exceed one sigma significance in each of these training samples and fulfills the same zenith angle distribution and transmission cuts.

6.5 The Crab Nebula Sanity Checks

The trained Random Forest for each subsample was checked by comparing the Crab Nebula spectrum results with previously published results. In Figure 6.4, 6.5, and

MC Period	Source	Date
ST.03.06	DarkPatch32	2015-01-22, 2015-02-24, 2015-02-25
ST.03.06	DarkPatch35	2015-02-23,2015-04-15
ST.03.06	DarkPatch34	2015-04-15
ST.03.06	G70.6	2015-04-20, 2015-04-22
ST.03.06	DarkPatch21	2015-09-30, 2015-10-01
ST.03.06	Dragonfly	2016-04-13, 2015-04-14
ST.03.07	DarkPatch34	2016-12-07
ST.03.07	DarkPatch08	2017-02-03
ST.03.07	DarkPatch06	2017-02-24
ST.03.07	DarkPatch10	2017-02-24
ST.03.11	DarkPatch50	2019-09-19
ST.03.11	Cyg-X3	2019-06-05, 2019-06-06, 2019-06-07
ST.03.12	Perseus-MA	2019-11-03,05,09,20,21 ,29,2020-01-01
ST.03.12	DarkPatch50	2019-09-19
ST.03.12	DarkPatch46	2019-09-20
ST.03.12	DarkPatch47	2019-09-21

TABLE 6.2: The data used as background sample for training Random Forest for the Crab Pulsar Analysis

6.6 the Crab Nebula spectra of all subsamples can be seen in two different zenith angle separation. The spectra show consistent results compared to the published MAGIC results.

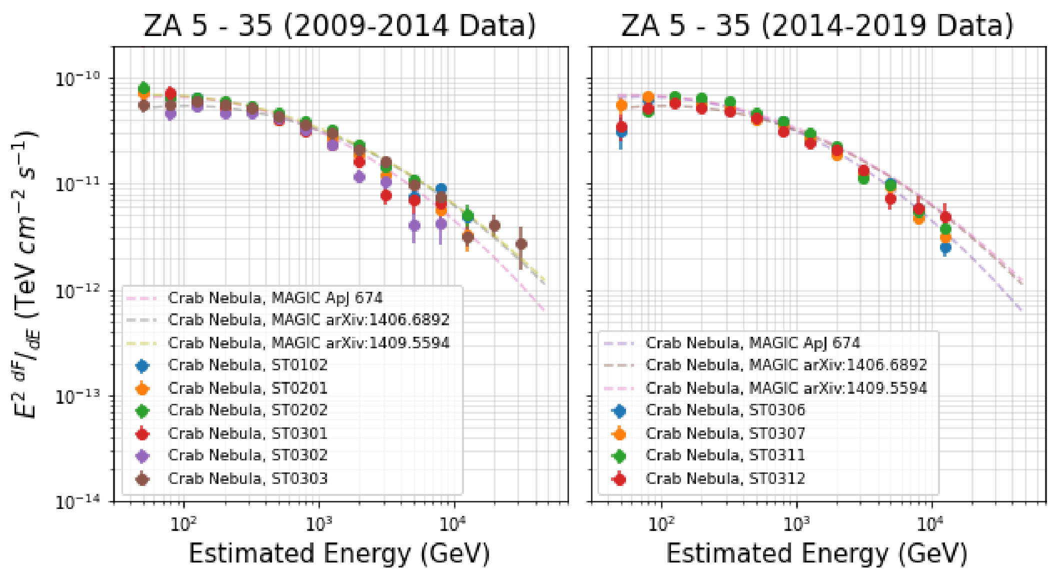

FIGURE 6.4: The Crab Nebula spectrum of each subsample (see Table 6.1) varies between 5-35 Zenith Angle.

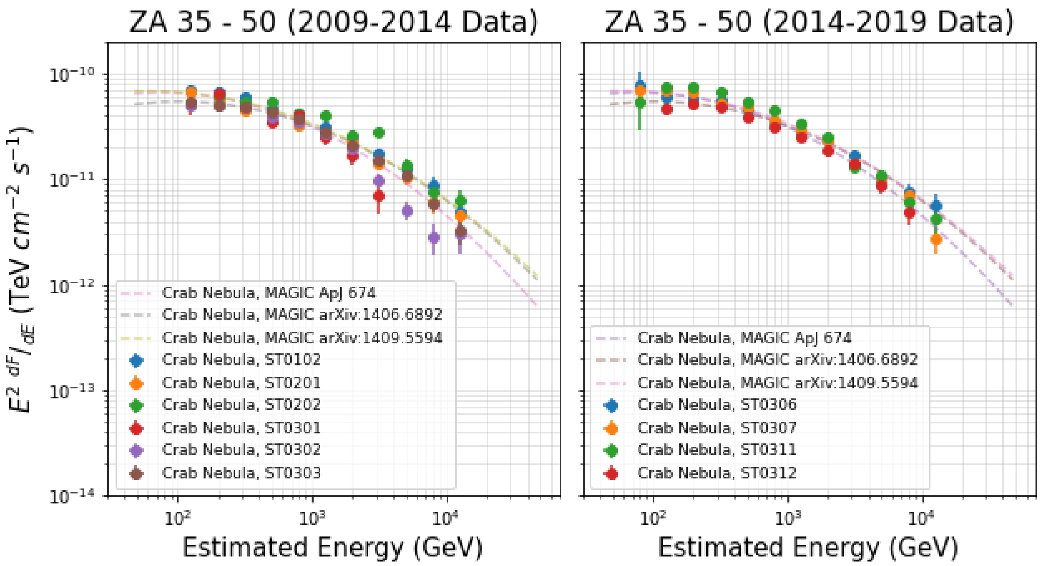

FIGURE 6.5: The Crab Nebula spectrum of each subsample (see Table 6.1) varies between 35-50 Zenith Angle.

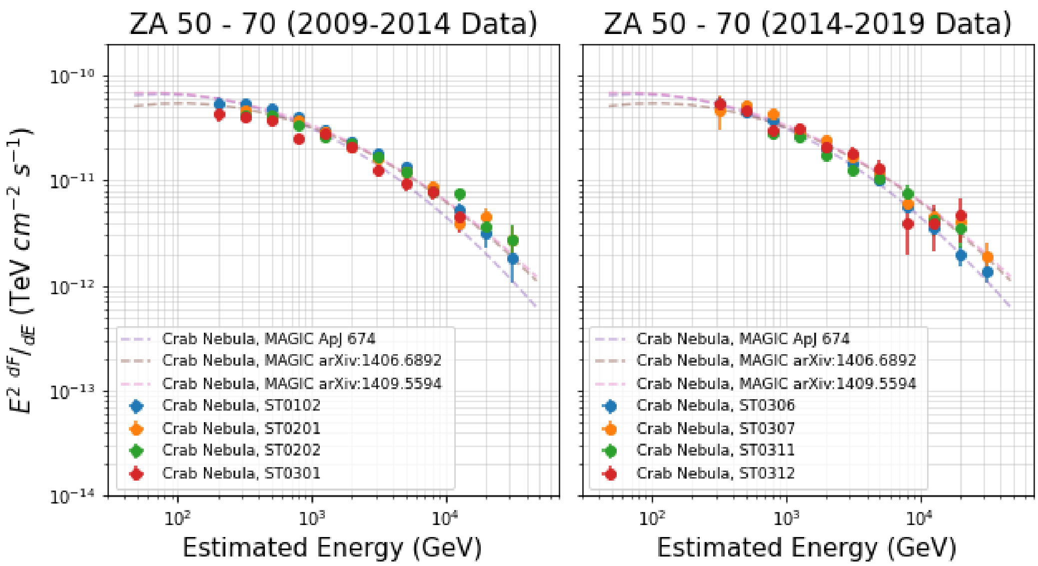

FIGURE 6.6: The Crab Nebula spectrum of each subsample (see Table 6.1) varies between 50-70 Zenith Angle.

6.6 Cut Optimization

Cut optimization plays a crucial role in Crab Pulsar's analysis above 100 GeV. The Crab Nebula gamma-rays also start to become a background for the Crab Pulsar, as well as the background composed of hadrons, electrons, and positrons. Therefore the hadronness and *theta*^{2} cuts were optimized for rejecting this gamma-dominant background ((Aleksić et al., 2012)).

For this purpose Li & Ma (17) formula was modified as the following:

$$\sigma_\gamma = LiMa(N_{on}\frac{\Gamma_{TP}}{\Gamma_{OP}} + N_{ex}\alpha, N_{on}, \frac{\Gamma_{TP}}{\Gamma_{OP}}) \tag{6.1}$$

For this calculation, the phase of the collected events restricted in the Off-phase

(OP) [0.52 - 0.87] region in order to optimize the cuts with events from the Crab Nebula. N_{on} is the total number of events collected with 0.18 theta2 cut, and N_{off} is the number of events collected from anti source position with the same $theta^2$ cut. N_{ex} refers to the number of excess events calculated by subtracting N_{on} and N_{off}. Γ_{TP} represents total pulse (TP) phase width combination of P1 and P2, and Γ_{TP} is phase width of OP. Besides, α is the parameter for taking into account the gamma-ray background and refers to the Crab Nebula to the Crab Pulsar (P1+P2) flux, as measured in (Ansoldi et al., 2016).

With this formula, significance values (σ_γ) were calculated for 30 binned ranges of hadronness and $theta^2$ values for energy range between 5-50000 GeV with 30 bins division. In the end, the maximum significance was selected, and the corresponding cuts were applied to each subsample.

6.7 Results

In this section, the Crab Pulsar results at VHE will be shown, which was observed by the MAGIC Telescopes in stereo mode between 2009-2019. There are two major data sets in this study, 2009-2014 and 2014-2019.

2009-2014 data have been used in the latest Crab Pulsar publication by the MAGIC Telescopes (Ansoldi et al., 2016). This data set was combined with around 100h mono mode observations by the Magic Telescopes (see Figure 6.1, Figure 6.2, and Table 6.3).

For this study, a bug in the stereoscopically reconstructed energy of 2009-2014 data set fixed by the author and combined with 124h of data taken in 2014-2019 by the MAGIC Telescopes.

Firstly, the effect of the bug in the spectrum of the Crab Pulsar was investigated. As mentioned in the section 6.2.1, the bug resulted in overestimated reconstructed energy (see Figure 6.3).

Afterterward two data sets were combined and achieved 345 hours in total. Spectral analyses were performed for the Crab Nebula, and the phase folded Crab Pulsar P1 and P2 separately. These analyses started with creating a spectrum by Flute for each subsample independently (for each of the observation period and the Zenith Angle observations) (see Chapter 3). After each spectrum was created, they were combined with Foam (see Chapter 3). Lastly, the best-fitting parameters of the intrinsic source spectrum (see Figure 6.7) was calculated using the Fold(see Chapter 3).

The best-fitting function both for P1 and P2 are power-law with the following expression and parameters in Table 6.3:

$$f_{E_0}(\frac{x}{E_0})^{\alpha} \tag{6.2}$$

The spectral flux results for each energy bin of Figure 6.7 can be found in Table 6.4.

In addition to the spectral analysis, the phase folded light curves, phaseograms, and this combined set of data were studied (see Figure 6.8). The number of excess events and the corresponding Li&Ma significance calculations can be found in Table 6.5. P2 still shows the hint of up to TeV emission above 400 GeV (Ansoldi et al., 2016). In the meantime, P1 gets dimmer above 400 GeV.

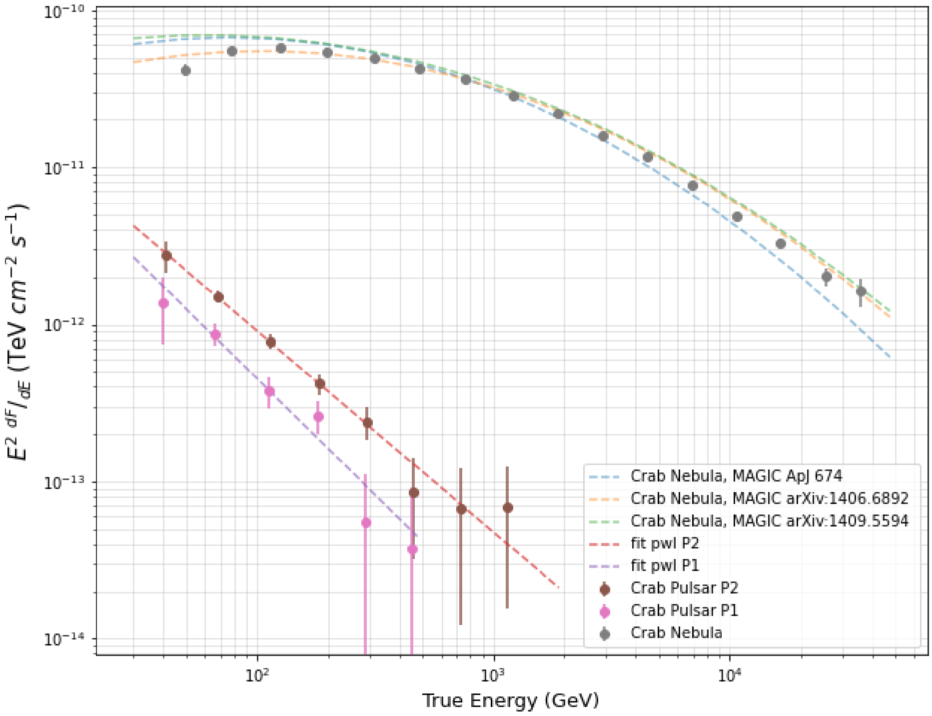

FIGURE 6.7: The spectra of the Crab Nebula and the Crab Pulsar P1 and P2 were computed by this work. The combined data set consists of 2009-2019 stereo mode observations by the MAGIC Telescopes. After each subsamples spectrum computed independently for computing the IRFs, the combined spectrum for each of the segments created. Intrinsic source spectrum and the best-fitting function can be seen in this Figure, and the corresponding parameters can be found in Table 6.3 and Table 6.4

		E_0 (GeV)	f_{E_0} $TeV^{-1}cm^{-2}s^{-1}$	α	χ^2/dof
MAGIC (Ansoldi et al., 2016)	P1	150	(1.1±0.3)x10^{-11}	3.2±0.4	0.3/3
	P2	150	(2.0±0.3)x10^{-11}	2.9±0.2	5.4/5
MAGIC this work	P1	150	(1.1±0.2)x10^{-11}	3.5±0.2	5.7/5
	P2	150	(2.4±0.2)x10^{-11}	3.3±0.1	1.1/7

TABLE 6.3: Results of the spectral fit parameters for the power-law function in equation 6.2 for Figure 6.7 as MAGIC this work and Figure 6.2 as MAGIC (Ansoldi et al., 2016)

Bin Center (GeV)	**P1** $E^2dN/dEdAdt$ $[TeVcm^{-2}s^{-1}]$ $x10^{-13}$	**P2** $E^2dN/dEdAdt$ $[TeVcm^{-2}s^{-1}]$ $x10^{-13}$
41.0	14 ± 6.2	28 ± 6.3
68.0	8.6 ± 1.4	15 ± 1.4
113.1	3.8 ± 0.8	7.8 ± 0.8
183.3	2.6 ± 0.6	4.2 ± 0.7
292.4	5.5 ± 0.6	2.4 ± 0.6
460.7	3.8 ± 0.5	0.9 ± 0.5
726.4		0.7 ± 0.5
1142.1		0.7 ± 0.5

TABLE 6.4: Forward folded spectral flux results of the Crab Pulsar shown in Figure 6.7

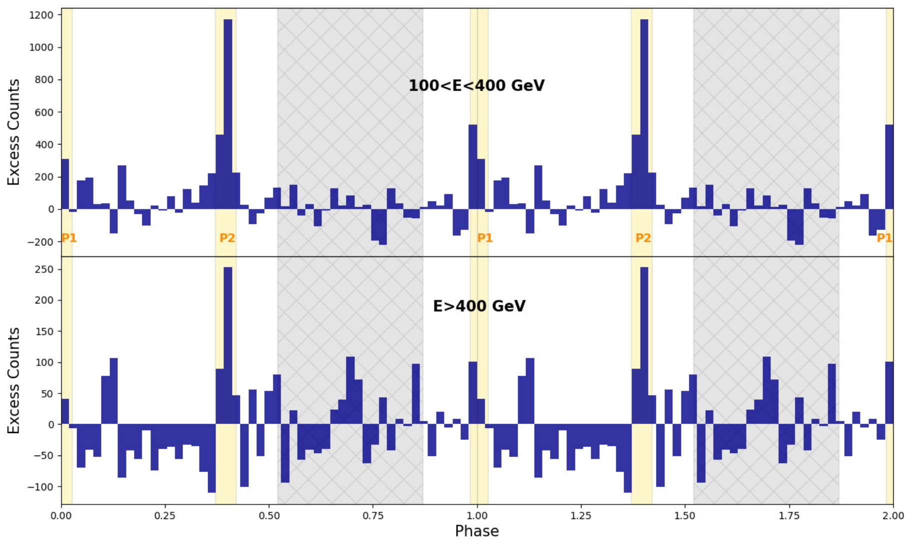

FIGURE 6.8: The Crab Pulsar phaseogram of data collected 2009-2019 by the MAGIC Telescopes. The upper panel shows the results for an energy range of 100-400 GeV events while the lower panel shows the events above 400 GeV.

Energy Range(GeV)	N_{ex}	Significance(LiMa)	
100-400 GeV	P1	1194.24 ± 169.67	7.13
	P2	2443.27 ± 177.39	14.10
>400 GeV	P1	139.62 ± 123.43	1.13
	P2	505.30 ± 128.00	3.98

TABLE 6.5: Excess events from the Crab Pulsar P2 and P1 for the energies between 100-400 GeV and above 400 GeV

Chapter 7

Lorentz Invariance Violation Limits with the Crab Pulsar

Pulsars are one of the essential sources for LIV ToF studies, as mentioned in the previous Chapters. Emissions up to TeV energies detected from the Crab Pulsar and the Vela Pulsar increase pulsars' competitiveness for these studies. The discovery of new pulsars at VHE and the detection of millisecond pulsars can improve the limits obtained by the LIV studies.

Firstly, in this chapter, LIV effects on pulsars and expectations on the phase delays will be explained. Afterward, the latest published limits obtained by Crab Pulsar with MAGIC observations will be reviewed, and lastly, the LIV limits obtained by this study will be presented.

7.1 What to Expect From Pulsars for the LIV studies

Using the formalism mentioned in the Chapter 2 (see 2.2), the mean phase delay, $\triangle\phi_n$, produced by the LIV effect test was described in (M. L. Ahnen et al., 2017):

$$\triangle\phi_n = c_n \cdot \left(\lambda_n \left(\frac{E}{GeV}\right)\right)^n \tag{7.1}$$

with

$$c_1 = \xi_1 \cdot \frac{d_{pulsar}}{c \cdot P_{pulsar}} \times 10^{-19} (GeV^{-1}) \tag{7.2}$$

$$c_2 = \xi_2 \cdot \frac{3}{2} \frac{d_{pulsar}}{c \cdot P_{pulsar}} \times 10^{-24} (GeV^{-2}) \tag{7.3}$$

where d_{pulsar} and P_{pulsar} are distance and period of the pulsar. λ_1, and λ_2 are called linear and quadratic LIV effect intensities, respectively, and their values were defined as the following:

$$\lambda_1 \equiv 10^{19} GeV / E_{QG_1} \tag{7.4}$$

$$\lambda_2 \equiv 10^{12} GeV / E_{QG_2} \tag{7.5}$$

With this equation, the expected LIV-induced phase shift for each pulsar can be calculated. Distance, and spin period of the pulsar, and the LIV intensity are the three main factors affecting the phase shift.To visualize the effect of LIV on the pulse shape of a pulsar, firstly, the Crab pulsar P2-like events were simulated (see Figure 7.1).

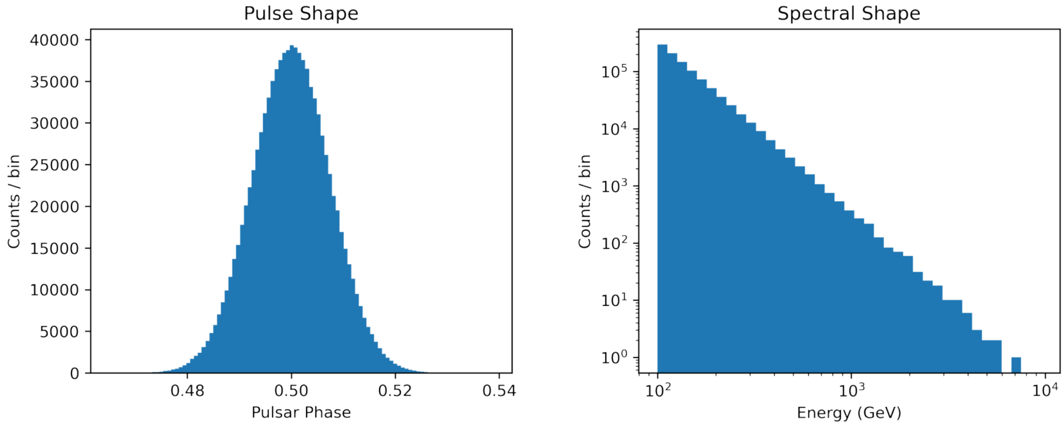

FIGURE 7.1: Crab Pulsar P2-like pulse shape and energy spectrum simulation was generated with 1.000.000 events coded by a custom Pyhton3 script. The phase of each event was assigned by a random Gaussian distribution with 0.045 phase-width as the Crab Pulsar P2, where the mean was located at 0.5 phase. The energy of the particles was assigned with a random distribution of spectral shape of -3.0 spectral index as the Crab Pulsar P2 between 100 GeV to 10 TeV.

With this pulse, five different cases were simulated. The first case is the Lorentz Invariant case that no phase shift is expected; therefore, the pulse shape was preserved as the original. For the other four cases, LIV-induced phase shifts were injected (see Equation 7.6) for the linear and quadratic cases with superluminal and subluminal effects for each of them. For this injection, the distance was used 2.9 kpc, similar to the Crab Pulsar. Additionally, the energy scales for the linear and the quadratic cases (E_{QG_1}, and E_{QG_2}) were chosen arbitrarily (2.4×10^{17}, and 6.1×10^{10} GeV) for making the pulse shape deformation visible in the phase-interval 0-1. The results can be seen for the linear and the quadratic cases respectively in Figure 7.2 and Figure 7.3.

$$phase_{shifted} = phase_{LI} \pm \triangle\phi_n \tag{7.6}$$

There is no intrinsic effect of pulsars that can mimic precisely the same energy-dependent phase distortion. Therefore, the LIV effect on the pulse shape can be distinguished.

Different amounts of phase shifts are expected for each pulsar. As mentioned in Chapter 1, there are three major pulsar candidate groups for VHE gamma-ray astronomy: young pulsars, normal pulsars (middle-aged pulsars), and the millisecond pulsars (old pulsars). The ATNF pulsar catalog (Manchester et al., 2005) was used to make an estimation of the phase shifts caused by linear and quadratic LIV cases for the different pulsar groups. Firstly, all the radio pulsars were extracted from the catalog on the website (https://www.atnf.csiro.au/research/pulsar/psrcat/). Pulsars with the unknown spin period, spin period derivative, or distance parameters were excluded because they are needed for calculating the phase shifts. As a result, 2167 pulsars remained, and all these pulsars were plotted in P-$\dot{P}$ diagram (see Figure 7.4). Secondly, the pulsars were grouped in three categories: young, normal, and millisecond pulsars. The average value of the spin period and the distance of each pulsar group were reported in Table7.1. Besides, the expected phase shifts of a 10 TeV photon caused by the linear and quadratic LIV cases are reported in the Table, too. The energy scale was selected as Planck Energy (1.22×10^{19} GeV).

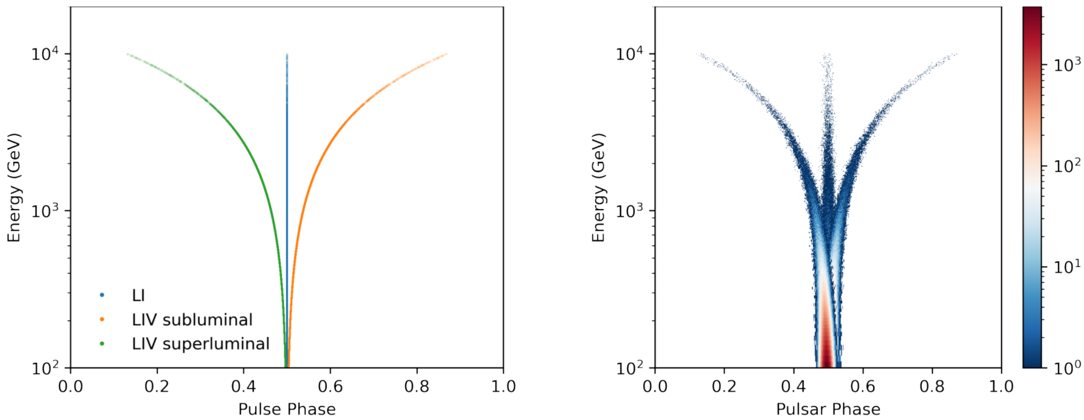

FIGURE 7.2: The deformation on the pulse shape by the LIV linear case at energy scale, $E_{QG_1} = 2.4 \times 10^{17}$. Pulse shape and deformation can be seen on the right side, where the color map refers to the number of event distribution. On the left, the effect can be seen on a line produced by 1.000.000 events, which does not have a certain width. Both plots show the middle pulse or line LI case. The line/pulse on the right-hand side shows the subliminal case, and the line/pulse on the left-hand side shows the superluminal case where the linear phase shifts injected accordingly.

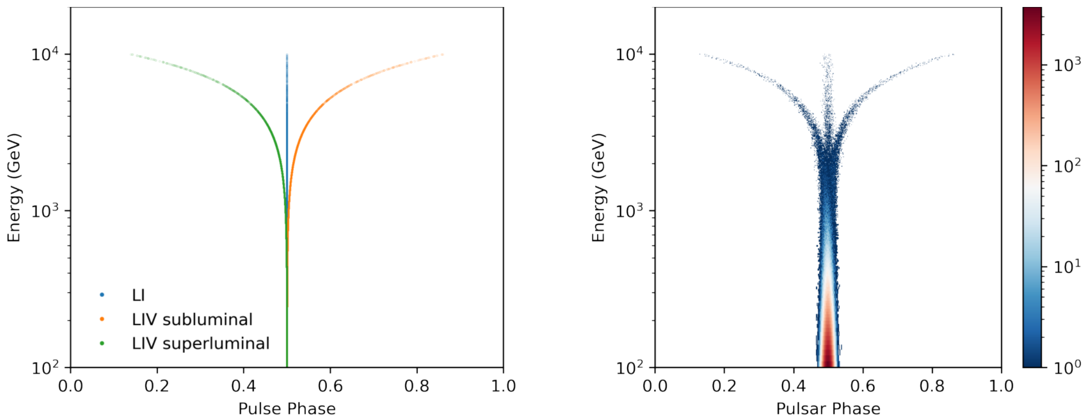

FIGURE 7.3: The deformation on the pulse shape by the LIV quadratic case at energy scale, $E_{QG_2} = 6.1 \times 10^{10}$. The procedure is the same as Figure 7.2 that applied for the quadratic case.

Pulsar Group	Age (years)	Spin (seconds)	Distance (kpc)	$\triangle\phi_1$ for 10 TeV (s)	$\triangle\phi_2$ for 10 TeV (s)
Young	10^4	0.06	4.8	0.7×10^{-2}	0.8×10^{-17}
Normal	10^8	0.8	5.3	0.6×10^{-3}	0.7×10^{-18}
Millisecond	10^9	0.004	2.9	0.6×10^{-1}	0.8×10^{-16}

TABLE 7.1: The averaged values of age, spin period, and distance of the pulsars are shown in Figure 7.4. The Expected phase shifts of a 10 TeV photon at the energy scale of Plank Energy (1.22×10^{19} GeV) for the linear and quadratic LIV cases were reported.

As shown in Table 7.1, LIV-induced phase shifts of the millisecond pulsar group

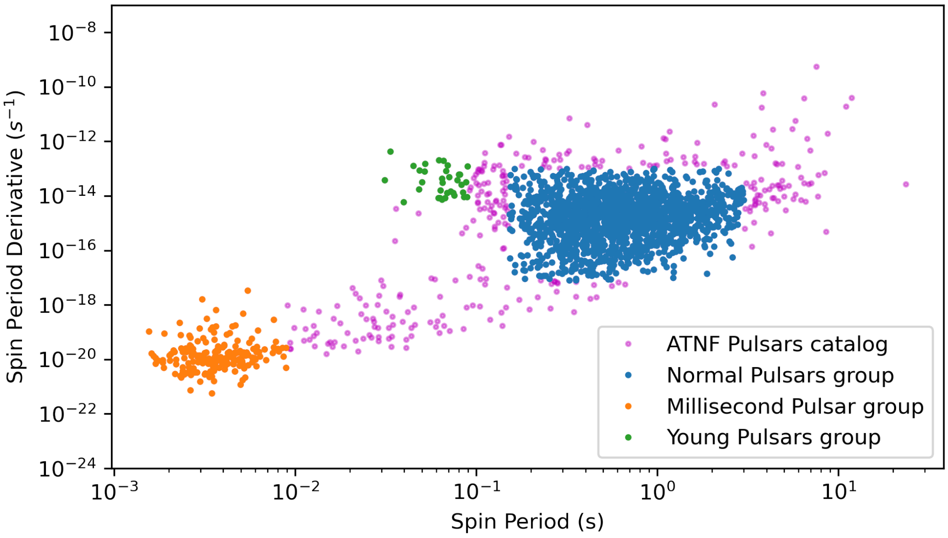

FIGURE 7.4: P-$\dot{P}$ diagram of pulsars extracted from the ATNF catalog ((Manchester et al., 2005) and the information were extracted from https://www.atnf.csiro.au/research/pulsar/psrcat/). The pink dots show 2167 radio pulsars with known spin, spin derivative, and distance parameters. A custom grouping method was applied to the pulsars for separating the young (green), normal (blue), and millisecond (orange) pulsars. Young pulsars were selected with spin periods lower than 0.09 s and spin derivative higher than 5×10^{-15}. Normal pulsars were selected with spin periods between 0.15-3 s, and spin derivative between 10^{-13} to 8×10^{-18}. Lastly, millisecond pulsars were selected with spin periods lower than 0.009 s and spin derivative lower than 9×10^{-18}.

have the highest shifts and are followed by the young pulsars and the normal pulsars. The discovery of millisecond pulsars at VHE can improve the LIV limits and the highest energy emission searches from the currently known VHE pulsars.

7.2 Previous Limits on LIV with Crab Pulsar with the MAGIC Telescopes

The Crab Pulsar is still the most promising candidate for the MAGIC telescopes for the LIV studies. The latest results obtained with the Crab Pulsar MAGIC observations are published in (M. L. Ahnen et al., 2017), which made the pulsars competitive again among the AGNs and GRBs.

In that study, two different methods had been used: the comparison method and the Maximum Likelihood Method. The later one had been able to make a more precise limit estimation than the peak comparison method.

7.2.1 The Peak Comparison Method

For the Peak comparison method, the events are divided into two energy groups, and it was checked whether there was any shift in the P2 peak point of the Crab

Pulsar between the higher and lower energy. The peak comparison method investigates shifts in the peak of the pulsars at different energies. Since the excess events at VHE are statistically low due to the high background events, this method is generally applied by dividing the events into two energy groups and comparing their peak locations.

The predicted average phase delay for the Crab Pulsar between photons of mean energies E_l(lower energy) and E_h (higher energy) due to the LIV (M. L. Ahnen et al., 2017):

$$\Delta\phi = \frac{d_{Crab}}{cP_{Crab}} \cdot \xi_n \frac{n+1}{2} \frac{E_h^n - E_l^n}{E_{QG_n}^n} \tag{7.7}$$

where ξ can be ± 1. d_{Crab} is the distance and P_{Crab} spin period of the Crab Pulsar. n refers to the order. The derived limits of E_{QG} becomes:

$$E_{QG_n} \geq (\xi_n \frac{n+1}{2} \frac{d_{Crab}}{cP_{Crab}} \frac{E_h^n - E_l^n}{\Delta\phi})^{1/n} \tag{7.8}$$

The Crab Pulsar events were divided into three different groups: the highest emission range was selected as 600-1200 GeV for comparing the high energy profile with low energy profiles. Two different low energy profiles were selected, 55-100 GeV and 400-600 GeV. Lowering the energy threshold is better for the comparison, but for Crab Pulsar, photons above 400 GeV could be driven with a different emission mechanism (ICS). For this reason, two different comparisons had been made (see Figure 7.5). The obtained limits can be found in Table 7.2

Nuisance Parameter	**Result (55-100 GeV)**	**Result (400-600 GeV)**	**Result (600-1200 GeV)**	**Result (400-1200 GeV)**
Gaussian Pulse Shape				
$\widehat{\phi_{P2}}$	0.398±0.001	0.403±0.006	0.404±0.005	0.403±0.004
$\widehat{\sigma_{P2}}$	0.011±0.001	0.018±0.007	0.011±0.005	0.015±0.005
χ^2/NDF	1.15	0.75	0.90	1.06
Lorentzian Pulse Shape				
$\widehat{\phi_{P2}}$	0.399±0.001	0.401±0.005	0.403±0.006	0.402±0.004
$\widehat{\gamma_{P2}}$	0.010±0.002	0.02±0.01	0.012±0.008	0.014±0.007
χ^2/NDF	1.14	0.73	0.89	0.97

TABLE 7.2: Obtained fit values from the Peak Comparison Method (M. L. Ahnen et al., 2017). The uncertainties are statistical only. ϕ_{P2} denotes Gaussian or Lorentzian shaped pulse mean for different energy profiles. σ_{P2} denotes the Gaussian sigma and γ_{P2} the Lorentzian half-width at half-maximum.

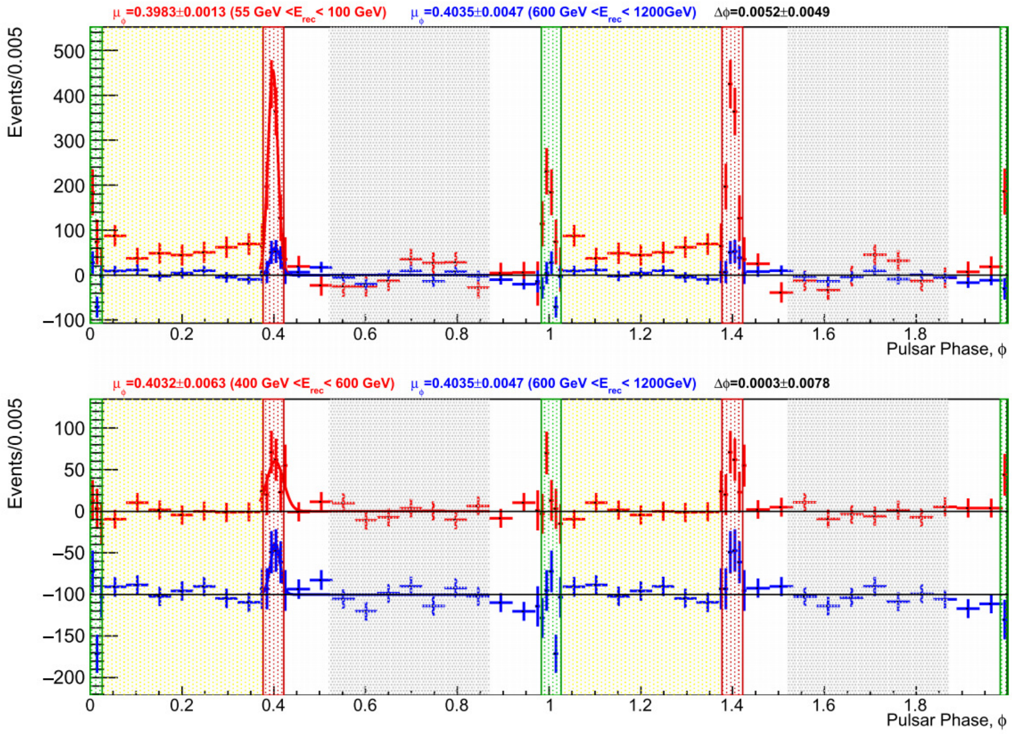

FIGURE 7.5: Phaseograms of the Peak Comparison method (M. L. Ahnen et al., 2017). The upper plot shows the comparison of events between 55-100 GeV (blue profile) and 600-1200 GeV (red profile), while the lower one shows 400-600 GeV (blue profile) and 600-1200 GeV (red profile). The red column shows the P2 region, the green shows the P1, and the yellow shows the bridge emission. The comparison method was applied to the P2. The peak positions were reported on the top of each phaseogram for each profile, as well as the estimated phase shifts. (see the results at Table 7.2)

Case	E_{QG_1} (GeV)		E_{QG_1} (GeV)	
	55-100 GeV versus 600-1200 GeV	400-600 GeV versus 600-1200 GeV	55-100 GeV versus 600-1200 GeV	400-600 GeV versus 600-1200 GeV
$\xi = +1$	2.5 $\times 10^{17}$	1.1 $\times 10^{17}$	1.8 $\times 10^{10}$	1.4 $\times 10^{10}$
$\xi = -1$	6.7 $\times 10^{17}$	1.1 $\times 10^{17}$	2.9 $\times 10^{10}$	1.5 $\times 10^{10}$

TABLE 7.3: Obtained 95%CL limits from the Peak Comparison Method (M. L. Ahnen et al., 2017) for comparison of different energy profiles shown in Figure 7.5 and Table7.2

7.2.2 Maximum Likelihood Method

The second and most sensitive method reported in (M. L. Ahnen et al., 2017) is the Maximum Likelihood Method (MLM). Using this method for testing the LIV limits of astrophysical objects was first proposed by Martıénez and Errando, 2009. By using the formalism described in (Vasileiou et al., 2013) (see Chapter 2), they derived the phase-shift and defined LIV intensities in Equation 7.1, 7.2, 7.3, 7.4, 7.5.

Profile likelihood ratio method (Murphy and Vaart, 2000) was used to define the test statistics D_n. The test statistic D_n for λ_n of the Crab pulsar data set:

$$D_n(\lambda_n|\mathbf{X}) = -2ln(\frac{\mathcal{L}(\lambda_n;\widehat{\widehat{v}}(\lambda_n)|\mathbf{X})}{\mathcal{L}(\widehat{\lambda_n};\widehat{v}(\lambda_n)|\mathbf{X}))}) \tag{7.9}$$

where $\mathbf{X}$ = $\{E_i', \phi_i', k_i\}$ was the Crab Pulsar dataset, and v nuisance parameters. E_i' refers to the reconstructed energy of each event i, and ϕ_i' its reconstructed phase, k_i is the observation period (see Table 7.4. Single hatted parameters $\left\{\widehat{\lambda_n}, \widehat{v}\right\}$, maximize the likelihood, while double-hatted parameters $\widehat{\widehat{v}}$ were maximizing $\mathcal{L}$ under the assumption of λ_n.

The likelihood $\mathcal{L}$ was formalized as an extended likelihood(Barlow, 1990):

$$\begin{aligned}\mathcal{L}(\lambda_n;\mathbf{v}|\mathbf{X}) &= \mathcal{L}(\lambda_n; f, \alpha, \phi_{P2}, \sigma_{P2}| \left\{\{E_i', \phi_i'\}_{i=0}^{N_k}\right\}_{i=0}^{N_s}) \\ &= P(\mathbf{v}) \cdot \prod_{k=0}^{N_s} exp(-g_k(\lambda_n;\mathbf{v}) - b_k \cdot \frac{1+\tau}{\tau}) \cdot \prod_{m=0}^{N_k^{OFF}} b_k \\ &\cdot \prod_{i=0}^{N_k^{ON}} (g_k(\lambda_n;\mathbf{v}) + \frac{b_k}{\tau}) \cdot P_k(E_i', \phi_i'|\lambda_n;\mathbf{v})\end{aligned} \tag{7.10}$$

where N_s denoted the number of observation periods (19 observation periods, see Table 7.4). N_k^{ON} and N_k^{OFF} denoted the number of events in the P2 ON-pulse (ϕ' [0.3558,0.4495]), and the OFF-pulse(ϕ' [0.52,0.87]) regions respectively. For each observation period k, the expected values of ON and OFF were g_k and b_k. They used the events with estimated energies E' ϵ [0.4,7] TeV. τ was the ratio of phase width of the OFF, divided by the one of the ON region. P(v) was the possible probability density function (PDF) for the nuisance parameters.

The PDF of event i was expressed as a combination of PDFs for signal (a pulsar event: $S_k(E_i', \phi_i'|\lambda_n; v)$, or the (interpolated) spectral energy distribution of the background: $h_k(E_i')$ for the k-th data subsample, respectively:

$$P_k(E_i', \phi_i'|\lambda_n;\mathbf{v}) = \frac{\frac{b_k}{\tau} \cdot h_k(E_i') + g_k(\lambda_n;\mathbf{v} \cdot S_k(E_i', \phi_i'|\lambda_n;\mathbf{v})}{g_k(\lambda_n;\mathbf{v}) + \frac{b_k}{\tau}} \tag{7.11}$$

The normalization constants of S_k, h_k, g_k, and b_k, depended on nuisance parameters and on λ_n. The signal PDF $S_k(E_i', \phi_i'|\lambda_n; v)$, was written as:

$$S_k(E_i', \phi_i'|\lambda_n;\mathbf{v}) = \frac{\Delta t_k \int_0^\infty R_k(E|E_i') \cdot \Gamma_{P2}(E, f, \alpha) \cdot F_{P2}(\phi_i', E|\lambda_n; \phi_{P2}, \sigma_{P2}) dE}{g_k(\lambda_n;\mathbf{v})} \tag{7.12}$$

where Δt_k was the effective observation time for each k-th data subsample. R_k was the product of the effective collection area(calculated with the MC simulations) to obtain true energy E of a photon from the estimated energy E′. The P2 pulsar spectrum Γ_{P2} was chosen as reported in (Ansoldi et al., 2016):

$$\Gamma_{P2}(E) = f \cdot (\frac{E}{E_{dec}})^{-\alpha} \cdot exp(-E/E_b) TeV^{-1} cm^{-2} s^{-1} \tag{7.13}$$

The pulsar phaseogram model F_{P2} was computed as:

$$F_{P2}(\phi_i', E|\phi_{P2}, \sigma_{P2}) = \int_0^\infty \frac{1}{2\pi\sigma_{res}\sigma_{P2}'} \cdot exp\left[-\frac{(\phi_i - \phi_{P2} - \Delta\phi(E|\lambda_n))^2}{2(\sigma_{P2}')^2} - \frac{(\phi_i' - \phi)^2}{2\sigma_{res}^2}\right] d\phi$$
$$= \frac{1}{\sqrt{2\pi}\sigma_{P2}} \cdot exp\left[-\frac{(\phi_i' - \phi_{P2} - \Delta\phi(E|\lambda_n))^2}{2\sigma_{P2}^2}\right]$$

where σ_{P2} was the observed width of P2. This width was constrained the intrinsic changes of the pulse width and the instrumental phase resolution. Lorentzian pulse shape was favored in the paper, and $\Delta\phi$ denoted the hypothetical phase delay produced by LIV, Equation 7.1.

For this analysis, the most challenging part is modeling the pulse profile. In the paper, it has been reported that theσ_{P2} widens as the energy increases, which was unexpected due to the reported significant pulse shrinking in (Aleksić et al., 2011b) (Aleksić et al., 2012). Therefore the following three pulse evolution models were tested.

- **Pulse Evolution Model 1:** No change in the pulse width :

$$\sigma_{P2} = \sigma_{P2,0} \tag{7.14}$$

- **Pulse Evolution Model 2:** Linearly changing pulse width with the logarithm of energy (similar to (Aleksić et al., 2012)) :

$$\sigma_{P2} = \sigma_{P2,0} - \frac{d\sigma_{P2}}{dlog(E)} \cdot log_{10}(\frac{E}{E_{min}}) \tag{7.15}$$

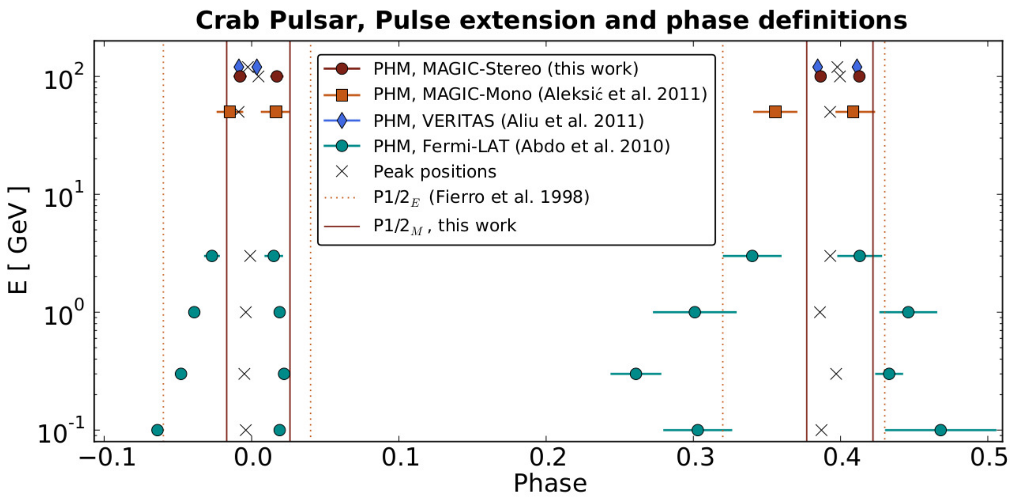

FIGURE 7.6: Crab Pulsar peak positions and peak widths reported in (Aleksić et al., 2012). The pulse width decrease with respect to energy increase is observable comparing the MAGIC and VERITAS results with the Fermi-LAT Results.

- **Pulse Evolution Model 3:** Abrupt transition of both pulse position and pulse width at a fixed (true) energy E_t. Pulse evolution model 3 was favored and E_t was reported as 285 GeV.

when E<E_t:

$$\sigma_{P2} = \sigma_{P2,1} \tag{7.16}$$

$$\phi_{P2} = \phi_{P2} \tag{7.17}$$

when E>E_t:

$$\sigma_{P2} = \sigma_{P2,2} \tag{7.18}$$

$$\phi_{P2} = \phi_{P2} + \Delta\phi_{P2} \tag{7.19}$$

Data Set	Observation Cycles	Zenith Angle Range (deg.)	Effective On-time (hr)	Telescope System	Observation Configuration
I	M.01.02	5-35	31	mono	Wobble
II	M.01.02	5-35	66	mono	on
III	ST.01.02	5-35	40	Stereo	Wobble
IV	ST.01.02	35-50	16	Stereo	Wobble
V	ST.01.02	50-62	5	Stereo	Wobble
VI	ST.01.02	5-35	34	Stereo	on
VII	ST.02.01	5-35	4	Stereo	Wobble
VIII	ST.02.01	35-50	2	Stereo	Wobble
IX	ST.02.02	5-35	5	Stereo	Wobble
X	ST.02.02	35-50	8	Stereo	Wobble
XI	ST.03.01	5-35	22	Stereo	Wobble
XII	ST.03.01	35-50	5	Stereo	Wobble
XIII	ST.03.01	50-70	12	Stereo	Wobble
XIV	ST.03.02	5-35	22	Stereo	Wobble
XV	ST.03.02	35-50	5	Stereo	Wobble
XVI	ST.03.02	50-70	9	Stereo	Wobble
XVII	ST.03.03	5-35	26	Stereo	Wobble
XVIII	ST.03.03	35-50	6	Stereo	Wobble
XIX	ST.03.03	50-70	8	Stereo	Wobble

TABLE 7.4: Summary of the used Crab Pulsar Data Samples (M. L. Ahnen et al., 2017). This data set was the same set used for reporting the highest emission from the Crab Pulsar (Ansoldi et al., 2016). The observation periods refer to the different MC periods due to different observation configurations, zenith angle ranges, changes in the telescope due to different environmental or hardware-related changes.

Figure 7.7 shows the results of the analysis that was applied with using E'_{min} = 400 GeV and E'_{min} = 100 GeV . Additionally, all pulse evolution models were tested with E'_{min} = 100 GeV and the nuisance parameters shown in Table 7.5. Results of lower E'_{min} were expected to give better results due to higher number of events; however, it was the other way around. The E'_{min} = 100 GeV likelihood was reported as worsened results with skewed and showing features between λ_2=20 and λ_2=40. Due to the fact that likelihood improves with E'_{min} = 400 GeV, the limits were obtained from that likelihood. 95% CL was reported as D=2.76 for the Lorentzian shaped pulse profile in the paper, that the obtained limits are shown in Table 7.7 and the systematic effects are shown in Table 7.6.

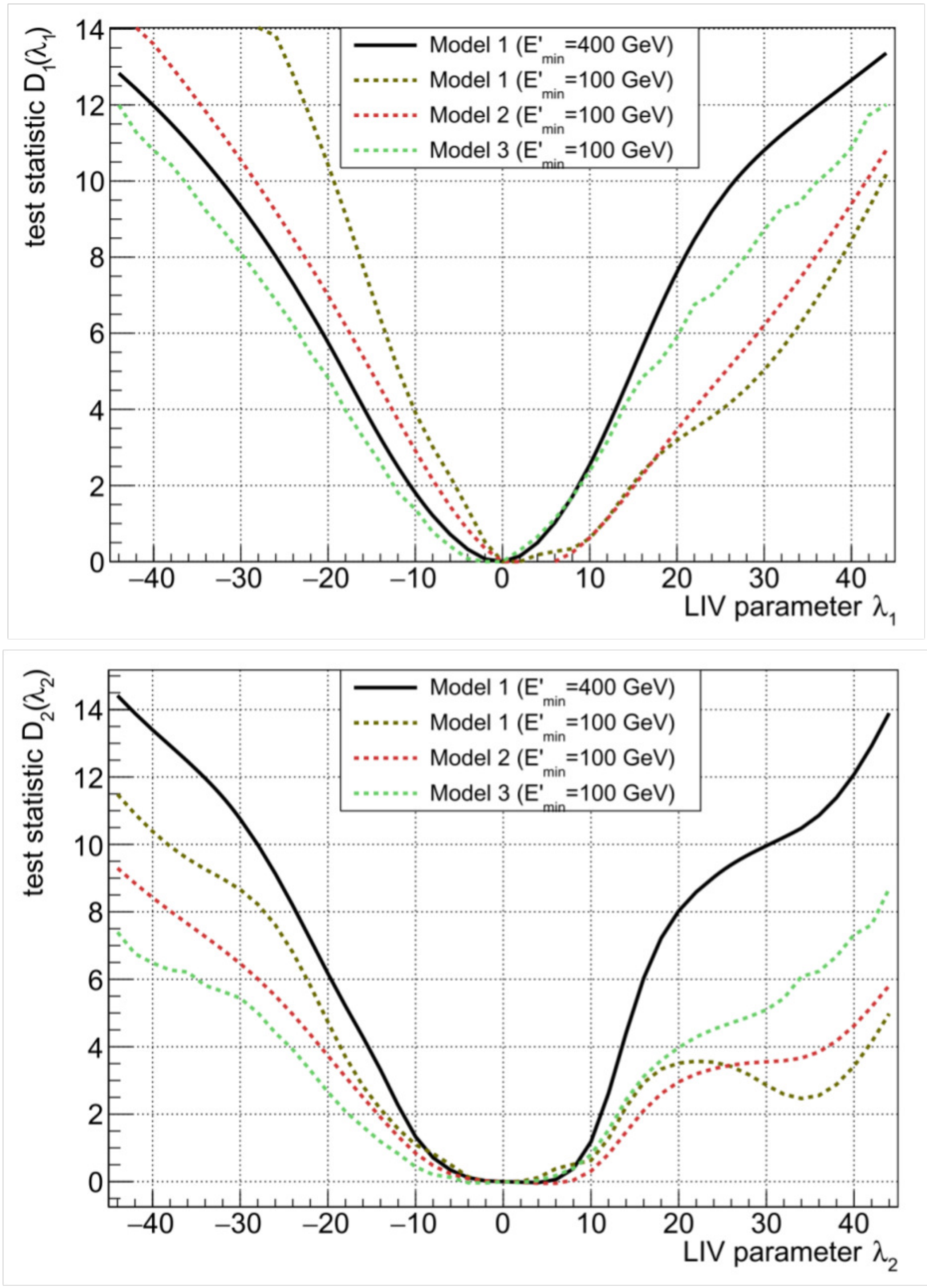

FIGURE 7.7: Test Statistics for the linear λ_1 and the quadratic λ_2 cases reported in (M. L. Ahnen et al., 2017). The obtained limits are shown in Table 7.7.

Nuisance Parameter	**Result (E′min=400 GeV)**	**Result (E′min = 100 GeV)**
Pulse Evolution Model 1		
$\widehat{f}$	6.3 ± 0.7	6.2 ± 0.6
$\widehat{\alpha}$	2.81 ± 0.07	2.95 ± 0.07
$\widehat{\phi_{P2}}$	0.403 ± 0.003	0.401 ± 0.001
$\widehat{\sigma_{P2}}$	0.015 ± 0.03	0.011 ± 0.002
Pulse Evolution Model 2		
$\widehat{f}$	6.3 ± 0.7	5.9 ± 0.5
$\widehat{\alpha}$	2.81 ± 0.07	2.92 ± 0.07
$\widehat{\phi_{P2}}$	0.403 ± 0.004	0.401 ± 0.001
$\widehat{\sigma_{P2}}$	0.015 ± 0.03	0.009 ± 0.002
$\widehat{d\sigma_{P2}/dlog(E)}$	0.00 ± 0.01	-0.006 ± 0.004
Pulse Evolution Model 3		
$\widehat{f}$	-	5.9 ± 0.6
$\widehat{\alpha}$	-	2.95 (fixed)
$\widehat{\phi_{P2}}$	-	0.4005 ± 0.0011
$\widehat{\Delta\phi_{P2}}$	-	0.004 ± 0.003
$\widehat{\sigma_{P2,1}}$	-	0.0089 ± 0.0009
$\widehat{\sigma_{P2,2}}$	-	0.015 ± 0.003
E_t (GeV)	-	285 ± 32

TABLE 7.5: Nuisance Parameters obtained in (M. L. Ahnen et al., 2017).

Systematic Effect	**Size(E_{QG_1})**	**Size(E_{QG_2})**
Background estimation	<10%	<15%
Absolute energy and flux scale	<7%	<5%
Different pulse shapes	<6%	0
Cutoff in energy spectrum	<30%	<30%
Contribution from the bridge	<5%	<5%
Distance Crab Pulsar	<25%	<12%
Total	< 42%	<36%

TABLE 7.6: Summary of the Systematic Uncertainties studied in (M. L. Ahnen et al., 2017).

Case	E_{QG_1} **(GeV)**	E_{QG_2} **(GeV)**
ζ=+1	5.5×10^{17}	5.9×10^{10}
ζ=-1	4.5×10^{17}	5.3×10^{10}

TABLE 7.7: 95% CL limits from the Profile Likelihood Method (M. L. Ahnen et al., 2017).

7.3 Limits on LIV with 2009-2019 Crab Pulsar MAGIC Observations

For this thesis, we have used the same C++ code as in (M. L. Ahnen et al., 2017), written by Markus Gaug. The data set (Table 7.8) that we used is the same Crab Pulsar data shown in Chapter 6. We have excluded the 100 hours of mono data due to poorer energy resolution compared to stereo data (see (Aleksić et al., 2016)). We have debugged an energy bug in the 2009-2014 stereo data and added 124 hours of new data taken in 2014-2019.

Data Set	Observation Cycles	Zenith Angle Range (deg.)	Effective On-time (hr)	Telescope System	Observation Configuration
I	ST.01.02	5-35	40	Stereo	Wobble
II	ST.01.02	35-50	16	Stereo	Wobble
III	ST.01.02	50-62	5	Stereo	Wobble
IV	ST.01.02	5-35	34	Stereo	on
V	ST.02.01	5-35	4	Stereo	Wobble
VI	ST.02.01	35-50	2	Stereo	Wobble
VII	ST.02.02	5-35	5	Stereo	Wobble
VIII	ST.02.02	35-50	8	Stereo	Wobble
IX	ST.03.01	5-35	22	Stereo	Wobble
X	ST.03.01	35-50	5	Stereo	Wobble
XI	ST.03.01	50-70	12	Stereo	Wobble
XII	ST.03.02	5-35	22	Stereo	Wobble
XIII	ST.03.02	35-50	5	Stereo	Wobble
XIV	ST.03.02	50-70	9	Stereo	Wobble
XV	ST.03.03	5-35	26	Stereo	Wobble
XVI	ST.03.03	35-50	6	Stereo	Wobble
XVII	ST.03.03	50-70	8	Stereo	Wobble
XVIII	ST.03.06	5-35	31	Stereo	Wobble
XIX	ST.03.06	35-50	4	Stereo	Wobble
XX	ST.03.06	50-70	21	Stereo	Wobble
XXI	ST.03.07&.09	5-35	21	Stereo	Wobble
XXII	ST.03.07&.09	35-50	11	Stereo	Wobble
XXIII	ST.03.07&.09	50-70	5	Stereo	Wobble
XXIV	ST.03.11	5-35	8	Stereo	Wobble
XXV	ST.03.11	35-50	7	Stereo	Wobble
XXVI	ST.03.11	50-70	1	Stereo	Wobble
XXVII	ST.03.12	5-35	9	Stereo	Wobble
XXVIII	ST.03.12	35-50	5	Stereo	Wobble
XXIX	ST.03.12	50-70	2	Stereo	Wobble

TABLE 7.8: Summary of the Crab Pulsar Data Samples Used in this work. The observation periods refer to the different MC periods due to different observation configurations, zenith angle ranges, changes in the telescope due to different environmental or hardware-related changes.

We used E'_{min} = 200 GeV (see Figure 7.8) with again taking into consideration that lowering the E'_{min} can improve the analysis. Previous analysis (MAGIC Collaboration et al., 2017) estimated a transition in 285 GeV, with taking into account the energy bug (see Chapter6 that was causing overestimation of the energy, we safely lowered the minimum energy to 200 GeV with taking into account the pulse model 2. The effective area and the background distributions used for these analysis can be found in Figure 7.9 and 7.10).

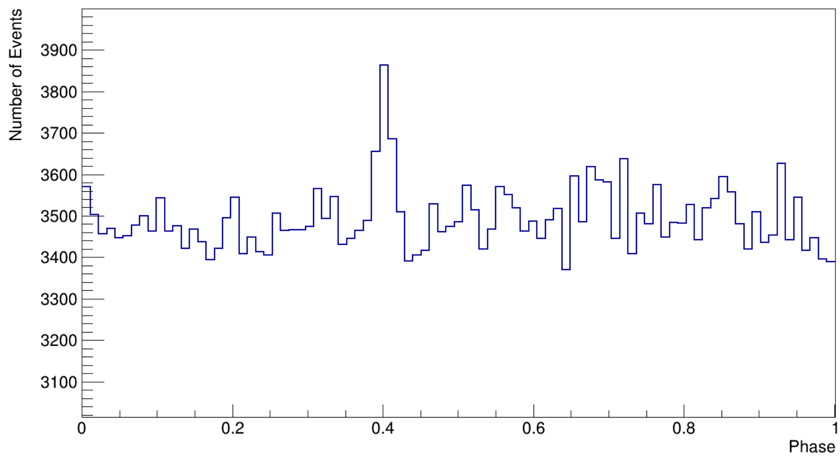

FIGURE 7.8: Phaseogram of the Crab Pulsar used for LIV analysis. The energy ranges from 200 GeV up to 7 TeV.

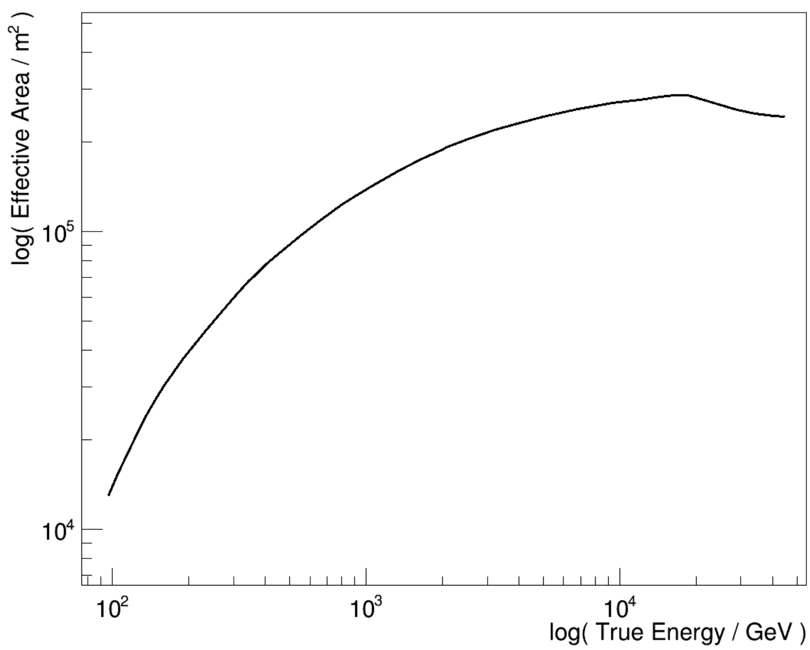

FIGURE 7.9: Effective Area of this study

The likelihood analysis results are shown in Figure 7.11 for the EQG_1 and in Figure 7.12 for the EQG_2 including the systematics reported in (M. L. Ahnen et al., 2017) (see Table 7.6). We observed similar skewed behavior for the likelihoods at higher λ values similar to the reported ones in (M. L. Ahnen et al., 2017) for low energy threshold analyses. These fluctuations were possibly due to problems precisely estimating nuisance parameters such as the peak position and width at

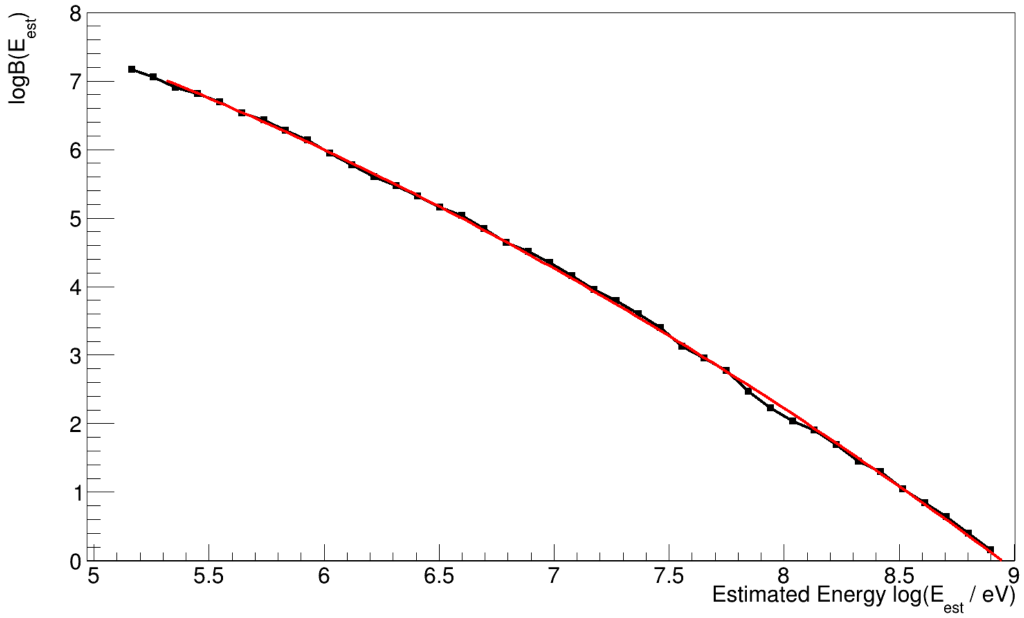

FIGURE 7.10: Background spectral distribution of this study 7.8.

higher energies. The nuisance parameters are reported in Table 7.9. However, the fluctuations are well above the 95% CL.

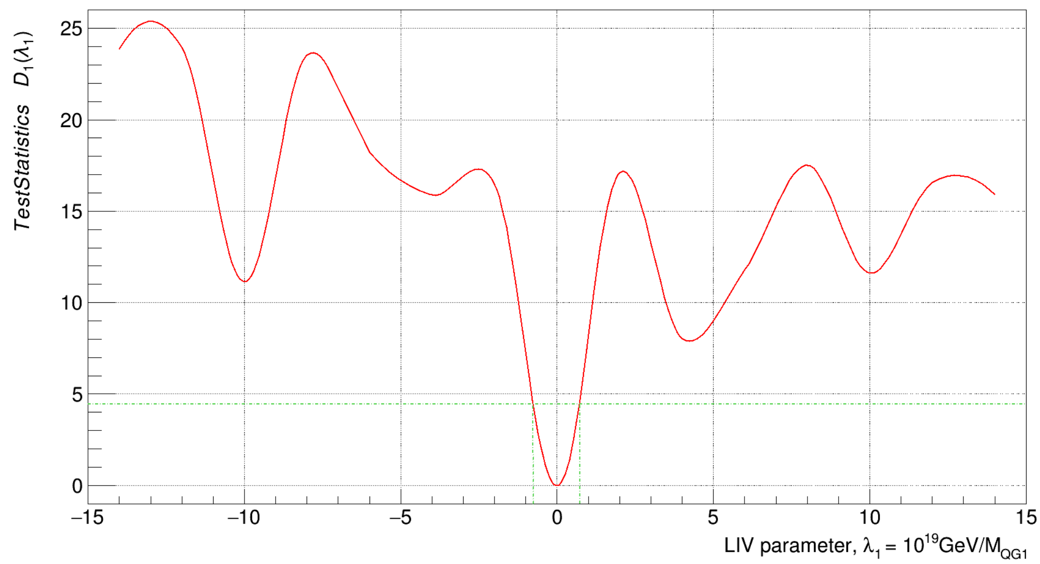

FIGURE 7.11: Test statistics results (-2δln(L)) for the linear λ_1 case for E'_{min} = 200 GeV. 95% CL *lambda* values (shown with green dashed lines) were calculated by using $\Delta D_1 = 4.45$ value reported in (MAGIC Collaboration et al., 2017). The corresponding M_{QG1} for the superluminal and subluminal scenarios are 1.3 and 1.4 (x 10^{19}) without the systematic uncertainies. For taking into account the uncertainities, the corresonding %95 CL λ value is increased by %42. The resulting M_{QG1} values are 0.93 and 0.95 (x 10^{19}), respectively.

The limits derived from this study give the best limit for the quadratic case

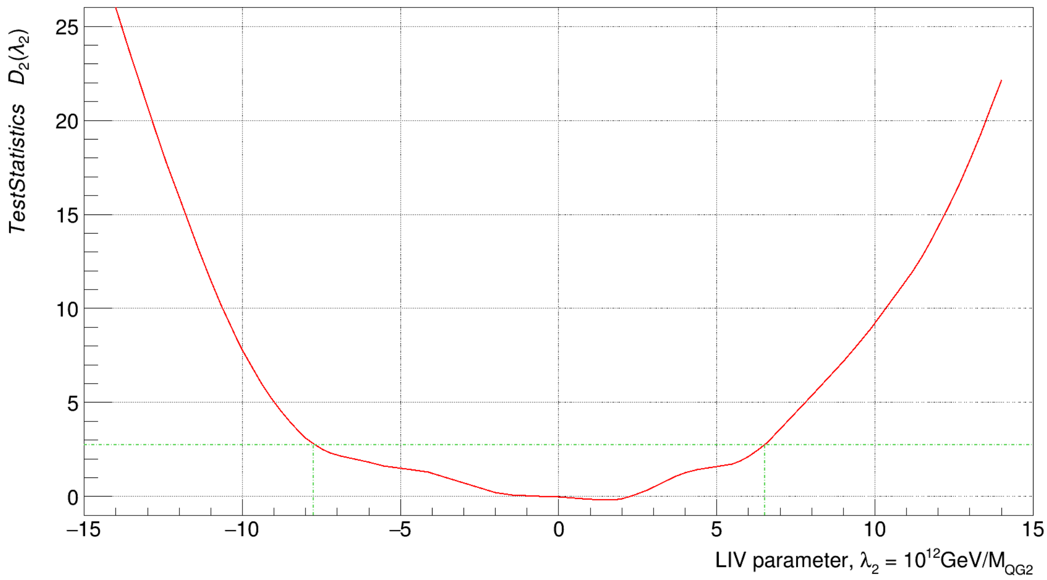

FIGURE 7.12: Test statistics results (-2δln(L)) for the quadratic λ_2 case for E'_{min} = 200 GeV. 95% CL *lambda* values (shown with green dashed lines) were calculated by using $\Delta D_2 = 2.76$ value reported in (MAGIC Collaboration et al., 2017). The corresponding M_{QG2} for the superluminal and subluminal scenarios are 12.9 and 15.3 (x 10^{10}) without the systematic uncertainties. For taking into account the uncertainities, the corresonding %95 CL λ value is increased by %36. The resulting M_{QG2} values are 9.5 and 11.3 (x 10^{10}), respectively.

Nuisance Parameter	**Result, Linear Case (E'min=200 GeV)**	**Result, Quadratic Case (E'min = 200 GeV)**
Pulse Evolution Model 2		
$\widehat{f}$	6.1 ± 0.3	5.9 ± 0.5
$\widehat{\alpha}$	3.1 ± 0.05	3.04 ± 0.07
$\widehat{\phi_{P2}}$	0.403 ± 0.004	0.403 ± 0.001
$\widehat{\sigma_{P2}}$	0.006 ± 0.000	0.006 ± 0.000
$d\sigma_{P2}\widehat{/dlog}(E)$	0.017 ± 0.000	0.017 ± 0.000

TABLE 7.9: Nuisance Parameters obtained in this study

among the GRBs and AGNs for maximum likelihood method single source time delay studies (see Table 7.10). Besides, the second-best limit was derived for the linear cases after the GRB090510 MLM limits (Vasileiou et al., 2013). The results show improvement around a factor of 2 compared to the previous MAGIC Crab Pulsar limits (M. L. Ahnen et al., 2017) for the quadratic case. Moreover, they have improved over a factor of 15 for the linear cases.

Case	E_{QG_1} 10^{19} **(GeV)**	E_{QG_2} 10^{12} **(GeV)**	**Source**
ξ=-1	**0.93**	**0.095**	**Crab Pulsar [This Work]**
	13.	0.094	GRB090510 [Vasileiou'13]
	0.036	0.085	Mrk 501 [H.E.S.S'19]
	0.055	0.059	Crab Pulsar [MAGIC'17]
	0.55	0.056	GRB190114C [MAGIC'20]
	0.021	0.026	Mrk 501 [MAGIC'08]
ξ=+1	**0.95**	**0.11**	**Crab Pulsar [This Work]**
	6.3	0.086	GRB090510 [Vasileiou'13]
	0.026	0.073	Mrk 501 [H.E.S.S'19]
	0.58	0.063	GRB190114C [MAGIC'20]
	0.045	0.053	Crab Pulsar [MAGIC'17]

TABLE 7.10: Table of recent LIV limits obtained with MLM for time delay studies for single sources. The shown limits are derived with 95% CL. The results are listed according to the descending order for the quadratic case.

Chapter 8

Conclusions

The improvement of the ground-based gamma-ray telescope systems leads to the detection of the new pulsars and extending the observed energy range of the known pulsars. So far only four pulsars have been detected at VHE regime, namely the Crab Pulsar, Vela Pulsar, Geminga pulsar and PSR B1706–44. All these pulsars are either young or middle-aged pulsars. In order to understand the nature of these objects, detecting older pulsars plays a crucial role. The best candidates for observing VHE emission from older pulsars are the millisecond pulsars.

In this study, VHE emission was searched from the millisecond pulsar PSR J0218 + 4232 using MAGIC data taken between 2018-2019. Pulsars are faint and in general low energy sources; therefore, reducing the energy threshold is essential for pulsar searches. Hints of HE emission up to 10 GeV were already reported by the Fermi-LAT for this source. With these motivations, we used special trigger and analysis tools optimized for low (<100 GeV) energies, which led to the detection of the Geminga Pulsar by MAGIC.

PSR J0218+4232 is almost an aligned rotator; therefore, it has broad on-pulse emission. The standard pulsar background subtraction method uses the off-pulse phase as background. But due to the broad on-pulse phase and the possibility that some gamma-ray emission was present also in the off-pulse phase, we applied a non-standard pulsar background subtraction technique. We collected the background events from three source-free reflected regions in the FoV, which helped us increase the number of events for the background estimation.

As a result of this analysis, no VHE emission was detected, and upper limits were set for the flux levels. This non-detection can be due to Klein-Nishina effects which leads to suppression of SSC for the millisecond pulsars and makes it harder to observe VHE emission (Alice K. Harding, 2021). The MAGIC results obtained in this study have been published in (Acciari et al., 2021). Further study on the PSRJ0218+4232 with the projected CTA facility will give better results, thanks to the lower energy threshold and better sensitivity that will be achieved.

An intermediate BLLac object 3C66A and a close-by radio galaxy 3C66B were serendipitously present in the FoV of the PSR J0218+4232. During the millisecond pulsar search, we also analyzed the 3C66A/B region. Due to the fact that the observation target was PSR J0218+4232, the 3C66A/B region was located at different distances to the center of the FoV for each wobble pointing position. Therefore we used non-standard and more complicated off-axis analysis methods to estimate the fluxes precisely.

As a result of the analysis, we detected both low-state quiescent emission during almost all days and a high-state flare emission for one night. In both cases, the emission detected by MAGIC was closer to 3C66A than 3C66B. Considering also the previous reports on the 3C66A activity, both in its low and its high state, by VERITAS and MAGIC, and taking into account that there are no other reports of VHE emission from 3C66B after the mono observation results by MAGIC-I, the emission we detected in this region was most probably originated from 3C66A. A dedicated study for disentangling these two close-by sources would be helpful to clarify the source of the emission, which is out of the scope and focus of this thesis.

In addition, ten years of MAGIC Stereo observations of the Crab Pulsar are studied. 2009-2014 data was already used in the latest VHE search from Crab Pulsar up to TeV energies (Ansoldi et al., 2016). For this study, we fixed a bug in the energy reconstruction algorithm. Moreover, the 20014-2019 data were analyzed, and all the data were combined. Although we observed a decrease in the gamma-ray excess at the highest energies compared to the published results (which overestimated it due to the energy reconstruction bug), our results show spectra and phaseograms generally compatible with previous MAGIC publications.

We used this ten years of Crab Pulsar stereo data set for constraining the LIV through a Maximum Likelihood Method (MLM) by using the code written for the previous analysis (M. L. Ahnen et al., 2017). The best LIV limits for the quadratic case subluminal (0.11x 10^{12} GeV) and superluminal (0.95x 10^{12} GeV) scenarios have been obtained among the single-source MLM time-delay studies. Furthermore, the second-best limit is obtained for the linear case subluminal (0.95x 10^{19} GeV) and superluminal(0.93x 10^{12} GeV) scenarios after the GRB090510 limits (**Vasileu**). These limits include the systematic errors reported in (M. L. Ahnen et al., 2017), which are %42 for the linear and %36 for the quadratic cases, respectively. Advancements in the estimation of the distance and the cut-off energy can enhance the limits.

The upper limits raised around a factor of 2 compared to the previous MAGIC Crab Pulsar limits (M. L. Ahnen et al., 2017) for the quadratic case. Moreover, they have increased over a factor of 15 for the linear case. These improvements are probably due to the following reasons. Firstly, replacing the single-telescope (monoscopic) data included in the previous study with stereo data helped to increase the energy resolution. Secondly, fixing the bug for the energy estimation in the previously used data set helped improve the results. Finally, lowering the minimum energy threshold to 200 GeV has contributed to an increase in excess events and narrower pulse width.

These results show that pulsars are as competitive as the GRBs and the AGNs for improving the LIV limits, although they are galactic sources. Adding more observational stereoscopic data to the MAGIC Crab Pulsar analysis can improve this study. Furthermore, discovering new pulsars, especially the millisecond pulsars, at VHE can be significant for the LIV studies.

Apart from the pulsar analysis presented in this study, the author contributed to the research and development tests of Barcelona Raman LIDAR, pathfinder of CTA, which will be a crucial tool also for future pulsar observations by CTA telescopes.

Bibliography

Abbott, B. P. et al. (2017). "GW170817: Observation of Gravitational Waves from a Binary Neutron Star Inspiral". In: Phys. Rev. Lett. 119.16, 161101 (10), p. 161101. DOI: 10.1103/PhysRevLett.119.161101. arXiv: 1710.05832 [gr-qc].

Abdo, A. A. et al. (2011). "Multi-wavelength Observations of the Flaring Gamma-ray Blazar 3C 66A in 2008 October". In: ApJ 726.1, 43 (1), p. 43. DOI: 10.1088/0004-637X/726/1/43. arXiv: 1011.1053 [astro-ph.HE].

Abdo, A. A. et al. (2013). "The Second Fermi Large Area Telescope Catalog of Gamma-Ray Pulsars". In: ApJS 208.2, 17 (10), p. 17. DOI: 10.1088/0067-0049/208/2/17. arXiv: 1305.4385 [astro-ph.HE].

Acciari, V. A. et al. (2021). "Search for Very High-Energy Emission from the millisecond pulsar PSR J0218+4232". In: arXiv e-prints, arXiv:2108.11373 (8), arXiv:2108.11373. arXiv: 2108.11373 [astro-ph.HE].

Aharonian, F. A., S. V. Bogovalov, and D. Khangulyan (2012a). "Abrupt acceleration of a 'cold' ultrarelativistic wind from the Crab pulsar". In: Nature 482.7386 (2), pp. 507–509. DOI: 10.1038/nature10793.

— (2012b). "Abrupt acceleration of a 'cold' ultrarelativistic wind from the Crab pulsar". In: Nature 482.7386 (2), pp. 507–509. DOI: 10.1038/nature10793.

Albert, J. et al. (Apr. 2008a). "Implementation of the Random Forest method for the Imaging Atmospheric Cherenkov Telescope MAGIC". In: Nuclear Instruments and Methods in Physics Research A 588.3, pp. 424–432. DOI: 10.1016/j.nima.2007.11.068. arXiv: 0709.3719 [astro-ph].

Albert, J. et al. (2008b). "VHE Gamma-Ray Observation of the Crab Nebula and its Pulsar with the MAGIC Telescope". In: ApJ 674.2 (2), pp. 1037–1055. DOI: 10.1086/525270. arXiv: 0705.3244 [astro-ph].

Aleksić, J. et al. (2011a). "Observations of the Blazar 3C 66A with the Magic Telescopes in Stereoscopic Mode". In: ApJ 726.2, 58 (1), p. 58. DOI: 10.1088/0004-637X/726/2/58. arXiv: 1010.0550 [astro-ph.HE].

Aleksić, J. et al. (2011b). "Observations of the Crab Pulsar between 25 and 100 GeV with the MAGIC I Telescope". In: ApJ 742.1, 43 (11), p. 43. DOI: 10.1088/0004-637X/742/1/43. arXiv: 1108.5391 [astro-ph.HE].

Aleksić, J. et al. (2012). "Phase-resolved energy spectra of the Crab pulsar in the range of 50-400 GeV measured with the MAGIC telescopes". In: A&A 540, A69 (4), A69. DOI: 10.1051/0004-6361/201118166. arXiv: 1109.6124 [astro-ph.HE].

Aleksić, J. et al. (2014). "Detection of bridge emission above 50 GeV from the Crab pulsar with the MAGIC telescopes". In: A&A 565, L12 (5), p. L12. DOI: 10.1051/0004-6361/201423664. arXiv: 1402.4219 [astro-ph.HE].

Aleksić, J. et al. (2016). "The major upgrade of the MAGIC telescopes, Part II: A performance study using observations of the Crab Nebula". In: Astroparticle Physics 72 (1), pp. 76–94.

DOI: 10.1016/j.astropartphys.2015.02.005.
arXiv: 1409.5594 [astro-ph.IM].

Aleksic, Jelena (2015).
"Dark Matter Searches in Dwarf Spheroidal Galaxy Segue 1 with MAGIC". In: Optimized Dark Matter Searches in Deep Observations of Segue 1 with MAGIC, pp. 109–167. DOI: 10.1007/978-3-319-23123-5_5.

Alexandreas, D. et al. (1995). "Status report on CLUE". In: Nuclear Instruments and Methods in Physics Research A 360 (2), pp. 385–389. DOI: 10.1016/0168-9002(94)01622-4.

Aliu, E. et al. (2008). "Observation of Pulsed γ-Rays Above 25 GeV from the Crab Pulsar with MAGIC". In: Science 322.5905 (11), p. 1221. DOI: 10.1126/science.1164718. arXiv: 0809.2998 [astro-ph].

Alpar, M. A. et al. (1982). "A new class of radio pulsars". In: Nature 300.5894 (12), pp. 728–730. DOI: 10.1038/300728a0.

Amelino-Camelia, Giovanni and Lee Smolin (2009). "Prospects for constraining quantum gravity dispersion with near term observations". In: Phys. Rev. D 80 (Oct), p. 084017. DOI: 10.1103/PhysRevD.80.084017. URL: https://link.aps.org/doi/10.1103/PhysRevD.80.084017.

Anderhub, H. et al. (2010). "Search for Very High Energy Gamma-ray Emission from Pulsar-Pulsar Wind Nebula Systems with the MAGIC Telescope". In: ApJ 710.1 (2), pp. 828–835. DOI: 10.1088/0004-637X/710/1/828.

Ansoldi, S. et al. (2016).
"Teraelectronvolt pulsed emission from the Crab Pulsar detected by MAGIC". In: A&A 585, A133 (1), A133. DOI: 10.1051/0004-6361/201526853. arXiv: 1510.07048 [astro-ph.HE].

Arons, J. and E. T. Scharlemann (1979). "Pair formation above pulsar polar caps: structure of the low altitude acceleration zone." In: ApJ 231 (8), pp. 854–879. DOI: 10.1086/157250.

Atwood, W. B. et al. (2009).
"The Large Area Telescope on the Fermi Gamma-Ray Space Telescope Mission". In: ApJ 697.2 (6), pp. 1071–1102. DOI: 10.1088/0004-637X/697/2/1071. arXiv: 0902.1089 [astro-ph.IM].

Auger, P. et al. (1939). "Extensive Cosmic-Ray Showers". In: Reviews of Modern Physics 11.3-4 (7), pp. 288–291. DOI: 10.1103/RevModPhys.11.288.

Baade, W. and F. Zwicky (1934). "Cosmic Rays from Super-novae". In: Proceedings of the National Academy of Science 20.5 (5), pp. 259–263. DOI: 10.1073/pnas.20.5.259.

Backer, D. C. et al. (1982). "A millisecond pulsar". In: Nature 300.5893 (12), pp. 615–618. DOI: 10.1038/300615a0.

Ballester, Otger et al. (2019).
"Raman LIDARs for the atmospheric calibration along the line-of-sight of CTA". In: arXiv e-prints, arXiv:1909.09342 (9), arXiv:1909.09342. arXiv: 1909.09342 [astro-ph.IM].

Baring, Matthew G. (2004).
"High-energy emission from pulsars: the polar cap scenario". In: Advances in Space Research 33.4 (1), pp. 552–560. DOI: 10.1016/j.asr.2003.08.020. arXiv: astro-ph/0308296 [astro-ph].

Barlow, Roger (1990). "Extended maximum likelihood". In: Nuclear Instruments and Methods in Physics Research A 297.3 (12), pp. 496–506. DOI: 10.1016/0168-9002(90)91334-8.

Barr, E. D. et al. (2013).
"Pulsar searches of Fermi unassociated sources with the Effelsberg telescope". In: MNRAS 429.2 (2), pp. 1633–1642. DOI: 10.1093/mnras/sts449. arXiv: 1301.0359 [astro-ph.HE].

Beckmann, V. and C. Shrader (2012). "The AGN phenomenon: open issues". In: Proceedings of "An INTEGRAL view of the high-energy sky (the first 10 years)", p. 69. arXiv: 1302.1397 [astro-ph.HE].

Behrendt, Andreas et al. (2002).
"Combined Raman lidar for the measurement of atmospheric temperature, water vapor, particle extinction coefficient, and particle backscatter coefficient". In: Appl. Opt. 41.36 (12), pp. 7657–7666. DOI: 10.1364/AO.41.007657.

Bernlöhr, Konrad (2000).
"Impact of atmospheric parameters on the atmospheric Cherenkov technique*". In: Astroparticle Physics 12.4 (1), pp. 255–268. DOI: 10.1016/S0927-6505(99)00093-6. arXiv: astro-ph/9908093 [astro-ph].

Bhattacharyya, B. et al. (2013). "GMRT Discovery of PSR J1544+4937: An Eclipsing Black-widow Pulsar Identified with a Fermi-LAT Source". In: ApJ 773.1, L12 (8), p. L12. DOI: 10.1088/2041-8205/773/1/L12. arXiv: 1304.7101 [astro-ph.HE].

Bignami, G. F. et al. (1975). "The COS-B experiment for gamma-ray astronomy." In: Space Science Instrumentation 1 (8), pp. 245–268.

Bisnovatyi-Kogan, G. S. and B. V. Komberg (1974).
"Pulsars and close binary systems". In: Soviet Ast. 18 (10), p. 217.

Blackett, P. M. S. (1948). "A possible contribution to the night sky from the Cerenkov radiation emitted by cosmic rays". In: The Emission Spectra of the Night Sky and Aurorae, p. 34.

Brambilla, Gabriele et al. (2018). "Electron-Positron Pair Flow and Current Composition in the Pulsar Magnetosphere". In: ApJ 858.2, 81 (5), p. 81. DOI: 10.3847/1538-4357/aab3e1. arXiv: 1710.03536 [astro-ph.HE].

Bretz, T. et al. (2009). "The drive system of the major atmospheric gamma-ray imaging Cherenkov telescope". In: Astroparticle Physics 31.2 (3), pp. 92–101. DOI: 10.1016/j.astropartphys.2008.12.001. arXiv: 0810.4593 [astro-ph].

Burgess, Cliff P et al. (2002).
"Loop-generated bounds on changes to the graviton dispersion relation". In: Journal of High Energy Physics 2002.03 (mar), pp. 043–043. DOI: 10.1088/1126-6708/2002/03/043. URL: https://doi.org/10.1088/1126-6708/2002/03/043.

Čerenkov, P. A. (1937). "Visible Radiation Produced by Electrons Moving in a Medium with Velocities Exceeding that of Light". In: Physical Review 52.4 (8), pp. 378–379. DOI: 10.1103/PhysRev.52.378.

Cerutti, Benoıˆt and Andrei M. Beloborodov (2017).
"Electrodynamics of Pulsar Magnetospheres". In: Space Sci. Rev. 207.1-4 (7), pp. 111–136. DOI: 10.1007/s11214-016-0315-7. arXiv: 1611.04331 [astro-ph.HE].

Chandrasekhar, S. (1931). "The highly collapsed configurations of a stellar mass". In: MNRAS 91 (3), pp. 456–466. DOI: 10.1093/mnras/91.5.456.

Chen, Alexander Y. and Andrei M. Beloborodov (2014).
"Electrodynamics of Axisymmetric Pulsar Magnetosphere with Electron-Positron Discharge: A Numerical Experiment". In: ApJ 795.1, L22 (11), p. L22. DOI: 10.1088/2041-8205/795/1/L22. arXiv: 1406.7834 [astro-ph.HE].

Cheng, K. S., C. Ho, and M. Ruderman (1986). "Energetic Radiation from Rapidly Spinning Pulsars. I. Outer Magnetosphere Gaps". In: ApJ 300 (1), p. 500. DOI: 10.1086/163829.

Contopoulos, Ioannis, Demosthenes Kazanas, and Christian Fendt (1999). "The Axisymmetric Pulsar Magnetosphere". In: ApJ 511.1 (1), pp. 351–358. DOI: 10.1086/306652. arXiv: astro-ph/9903049 [astro-ph].

Coroniti, F. V. (1990). "Magnetically Striped Relativistic Magnetohydrodynamic Winds: The Crab Nebula Revisited". In: ApJ 349 (2), p. 538. DOI: 10.1086/168340.

Daniel, M. K. and CTA Consortium (2015). "The Atmospheric Monitoring Strategy for the Cherenkov Telescope Array". In: Journal of Physics Conference Series. Vol. 595. Journal of Physics Conference Series, p. 012009. DOI: 10.1088/1742-6596/595/1/012009. arXiv: 1501.00826 [astro-ph.IM].

Daugherty, J. K. and A. K. Harding (1982). "Electromagnetic cascades in pulsars." In: ApJ 252 (1), pp. 337–347. DOI: 10.1086/159561.

Dazzi, F. et al. (2015). "Performance studies of the new stereoscopic Sum-Trigger-II of MAGIC after one year of operation". In: arXiv e-prints, arXiv:1508.05255 (8), arXiv:1508.05255. arXiv: 1508.05255 [astro-ph.IM].

Dazzi, F. et al. (2021). "The Stereoscopic Analog Trigger of the MAGIC Telescopes". In: IEEE Transactions on Nuclear Science, pp. 1–1. DOI: 10.1109/TNS.2021.3079262.

Deppo, Vania Da et al. (2012). "Preliminary optical design of a polychromator for a Raman LIDAR for atmospheric calibration of the Cherenkov Telescope Array". In: Optical Systems Design 2012. Ed. by Laurent Mazuray et al. Vol. 8550. International Society for Optics and Photonics. SPIE, pp. 537–543. DOI: 10.1117/12.979789. URL: https://doi.org/10.1117/12.979789.

Deshpande, Avinash A. and Joanna M. Rankin (1999). "Pulsar Magnetospheric Emission Mapping: Images and Implications of Polar CAP Weather". In: ApJ 524.2 (10), pp. 1008–1013. DOI: 10.1086/307862. arXiv: astro-ph/9909398 [astro-ph].

Desvignes, G. et al. (2016). "High-precision timing of 42 millisecond pulsars with the European Pulsar Timing Array". In: MNRAS 458.3 (5), pp. 3341–3380. DOI: 10.1093/mnras/stw483. arXiv: 1602.08511 [astro-ph.HE].

Deutsch, Arnim J. (1955). "The electromagnetic field of an idealized star in rigid rotation in vacuo". In: Annales d'Astrophysique 18 (1), p. 1.

Djannati-Ataı¨, A. et al. (2017). "Probing Vela pulsar down to 20 GeV with H.E.S.S. II observations". In: 6th International Symposium on High Energy Gamma-Ray Astronomy. Vol. 1792. American Institute of Physics Conference Series, p. 040028. DOI: 10.1063/1.4968932.

Doering, M. et al. (2001). "Measurement of the Cherenkov light spectrum and of the polarization with the HEGRA-IACT-system". In: arXiv e-prints, astro-ph/0107149 (7), astro–ph/0107149. arXiv: astro-ph/0107149 [astro-ph].

Domıénguez, A. et al. (2011). "Extragalactic background light inferred from AEGIS galaxy-SED-type fractions". In: MNRAS 410.4 (2), pp. 2556–2578. DOI: 10.1111/j.1365-2966.2010.17631.x. arXiv: 1007.1459 [astro-ph.CO].

Douglas, Michael R. and Nikita A. Nekrasov (2001). "Noncommutative field theory". In: Rev. Mod. Phys. 73 (Nov), pp. 977–1029. DOI: 10.1103/RevModPhys.73.977. URL: https://link.aps.org/doi/10.1103/RevModPhys.73.977.

Du, Y. J., G. J. Qiao, and D. Chen (2013). "Radio and Gamma-Ray Pulsed Emission from Millisecond Pulsars". In: ApJ 763.1, 29 (1), p. 29. DOI: 10.1088/0004-637X/763/1/29. arXiv: 1211.5208 [astro-ph.HE].

Du, Y. J., G. J. Qiao, and W. Wang (2012). "Radio-to-TeV Phase-resolved Emission from the Crab Pulsar: The Annular Gap Model". In: ApJ 748.2, 84 (4), p. 84. DOI: 10.1088/0004-637X/748/2/84. arXiv: 1202.1096 [astro-ph.HE].

Du, Y. J. et al. (2011). "Gamma-ray Emission from the Vela Pulsar Modeled with the Annular Gap and the Core Gap". In: ApJ 731.1, 2 (4), p. 2. DOI: 10.1088/0004-637X/731/1/2. arXiv: 1102.2476 [astro-ph.HE].

Dyks, J. and B. Rudak (2003). "Two-Pole Caustic Model for High-Energy Light Curves of Pulsars". In: ApJ 598.2 (12), pp. 1201–1206. DOI: 10.1086/379052. arXiv: astro-ph/0303006 [astro-ph].

Eizmendi Valles, Miguel Ignacio (2011). "Raman LIDAR Link Budget and Components". PhD thesis. [Barcelona]: Universitat Autònoma de Barcelona. URL: http://hdl.handle.net/2099.1/12959.

Fichtel, C. E. et al. (1993). "Results from the Energetic Gamma-Ray Experiment Telescope (EGRET) on the Compton Observatory". In: Advances in Space Research 13.12 (12), pp. 637–646. DOI: 10.1016/0273-1177(93)90175-B.

Fidalgo, D.C. (2019). Revealing the Most Energetic Light from Pulsars and Their Nebulae. Springer Theses. Springer International Publishing. ISBN: 9783030241940. URL: https://books.google.es/books?id=wkGjDwAAQBAJ.

Fruck, Christian et al. (2014). "A novel LIDAR-based Atmospheric Calibration Method for Improving the Data Analysis of MAGIC". In: arXiv e-prints, arXiv:1403.3591 (3), arXiv:1403.3591. arXiv: 1403.3591 [astro-ph.IM].

Galindo Fernández, Daniel (2018). Study of the extreme gamma-ray emission from Supernova Remnants. URL: http://hdl.handle.net/2445/125664.

Gambini, Rodolfo and Jorge Pullin (1999). "Nonstandard optics from quantum space-time". In: Phys. Rev. D 59 (May), p. 124021. DOI: 10.1103/PhysRevD.59.124021. URL: https://link.aps.org/doi/10.1103/PhysRevD.59.124021.

Gaug, Markus (2006). "Calibration of the MAGIC Telescope and Observation of Gamma Ray Bursts". PhD thesis. [Barcelona]: Universitat Autònoma de Barcelona. URL: http://www.tdx.cat/TDX-1122106-155837.

Gaug, Markus et al. (2019). "The IFAE/UAB Raman LIDAR for the CTA-North". In: European Physical Journal Web of Conferences. Vol. 197. European Physical Journal Web of Conferences, p. 02005. DOI: 10.1051/epjconf/201919702005.

Goldreich, Peter and William H. Julian (1969). "Pulsar Electrodynamics". In: ApJ 157 (8), p. 869. DOI: 10.1086/150119.

Hamed, N. Arkani et al. (2004). "Ghost Condensation and a Consistent IR Modification of Gravity". In: Journal of High Energy Physics 2004.05 (may), pp. 074–074. DOI: 10.1088/1126-6708/2004/05/074. URL: https://doi.org/10.1088/1126-6708/2004/05/074.

Harding, Alice K. (2013). "The neutron star zoo". In: Frontiers of Physics 8.6 (12), pp. 679–692. DOI: 10.1007/s11467-013-0285-0. arXiv: 1302.0869 [astro-ph.HE].

— (2021). "The Emission Physics of Millisecond Pulsars". In: arXiv e-prints, arXiv:2101.05751 (1), arXiv:2101.05751. arXiv: 2101.05751 [astro-ph.HE].

Harding, Alice K. and Constantinos Kalapotharakos (2015). "SYNCHROTRON SELF-COMPTON EMISSION FROM THE CRAB AND OTHER PULSARS". In: The Astrophysical Journal 811.1 (sep), p. 63. DOI: 10.1088/0004-637x/811/1/63. URL: https://doi.org/10.1088%2F0004-637x%2F811%2F1%2F63.

Harding, Alice K. et al. (2008). "High-Altitude Emission from Pulsar Slot Gaps: The Crab Pulsar". In: ApJ 680.2 (6), pp. 1378–1393. DOI: 10.1086/588037. arXiv: 0803.0699 [astro-ph].

Hess, V. F. (1912). "Über Beobachtungen der durchdringenden Strahlung bei sieben Freiballonfahrten". In: Physikalische Zeitschrift 13, pp. 1084–1091.

Hewish, A. et al. (1968). "Observation of a Rapidly Pulsating Radio Source". In: Nature 217.5130 (2), pp. 709–713. DOI: 10.1038/217709a0.

Hillas, A. M. (1985). "Cerenkov Light Images of EAS Produced by Primary Gamma Rays and by Nuclei". In: 19th International Cosmic Ray Conference (ICRC19), Volume 3. Vol. 3. International Cosmic Ray Conference, p. 445.

Hirotani, Kouichi (2008). "Outer-Gap versus Slot-Gap Models for Pulsar High-Energy Emissions: The Case of the Crab Pulsar". In: ApJ 688.1 (11), p. L25. DOI: 10.1086/595000. arXiv: 0810.0865 [astro-ph].

— (2011). "Pulsar Outer-gap Electrodynamics: Hardening of Spectral Shape in the Trailing Peak in the Gamma-Ray Light Curve". In: ApJ 733.2, L49 (6), p. L49. DOI: 10.1088/2041-8205/733/2/L49. arXiv: 1104.5357 [astro-ph.HE].

Hobbs, G. B., R. T. Edwards, and R. N. Manchester (2006). "TEMPO2, a new pulsar-timing package - I. An overview". In: MNRAS 369.2 (6), pp. 655–672. DOI: 10.1111/j.1365-2966.2006.10302.x. arXiv: astro-ph/0603381 [astro-ph].

Horava, Petr (2009). "Quantum gravity at a Lifshitz point". In: Phys. Rev. D 79 (Apr), p. 084008. DOI: 10.1103/PhysRevD.79.084008. URL: https://link.aps.org/doi/10.1103/PhysRevD.79.084008.

Hulse, R. A. and J. H. Taylor (1975). "Discovery of a pulsar in a binary system." In: ApJ 195 (1), pp. L51–L53. DOI: 10.1086/181708.

Kalapotharakos, Constantinos, Alice K. Harding, and Demosthenes Kazanas (2014). "Gamma-Ray Emission in Dissipative Pulsar Magnetospheres: From Theory to Fermi Observations". In: ApJ 793.2, 97 (10), p. 97. DOI: 10.1088/0004-637X/793/2/97. arXiv: 1310.3545 [astro-ph.HE].

Kalapotharakos, Constantinos et al. (2018). "Three-dimensional Kinetic Pulsar Magnetosphere Models: Connecting to Gamma-Ray Observations". In: ApJ 857.1, 44 (4), p. 44. DOI: 10.3847/1538-4357/aab550. arXiv: 1710.03170 [astro-ph.HE].

Kaplan, D. L. et al. (2012). "Discovery of the Optical/Ultraviolet/Gamma-Ray Counterpart to the Eclipsing Millisecond Pulsar J1816+4510". In: ApJ 753.2, 174 (7), p. 174. DOI: 10.1088/0004-637X/753/2/174. arXiv: 1205.3699 [astro-ph.HE].

Kirk, J. G., O. Skjæraasen, and Y. A. Gallant (2002). "Pulsed radiation from neutron star winds". In: A&A 388 (6), pp. L29–L32. DOI: 10.1051/0004-6361:20020599. arXiv: astro-ph/0204302 [astro-ph].

Klett, James D. (1981). "Stable analytical inversion solution for processing lidar returns". In: Appl. Opt. 20.2 (1), pp. 211–220. DOI: 10.1364/AO.20.000211.

Kostelecký, V. Alan and Stuart Samuel (1989). "Spontaneous breaking of Lorentz symmetry in string theory". In: Phys. Rev. D 39 (Jan), pp. 683–685. DOI: 10.1103/PhysRevD.39.683. URL: https://link.aps.org/doi/10.1103/PhysRevD.39.683.

Kraushaar, W. et al. (1965). "Explorer XI Experiment on Cosmic Gamma Rays." In: ApJ 141 (4), p. 845. DOI: 10.1086/148179.

Kuiper, L. et al. (2000). "The likely detection of pulsed high-energy gamma -ray emission from millisecond pulsar PSR J0218+4232". In: A&A 359 (7), pp. 615–626. arXiv: astro-ph/0005338 [astro-ph].

Large, M. I., A. E. Vaughan, and B. Y. Mills (1968). "A Pulsar Supernova Association?" In: Nature 220.5165 (10), pp. 340–341. DOI: 10.1038/220340a0.

Li, T. -P. and Y. -Q. Ma (1983). "Analysis methods for results in gamma-ray astronomy." In: ApJ 272 (9), pp. 317–324. DOI: 10.1086/161295.

Longair, Malcolm S. (1992). High energy astrophysics. Vol.1: Particles, photons and their detection.

Lopez Oramas, A. et al. (2013). "The IFAE/UAB and LUPM Raman LIDARs for Cherenkov Telescope Array Observatory". In: International Cosmic Ray Conference. Vol. 33. International Cosmic Ray Conference, p. 2831. arXiv: 1307.5092 [astro-ph.IM].

López Oramas, Alicia (2014). "Multi-year campaign of the gamma-ray binary LSI+61 303 and search for VHE emission from gamma-ray binary candidates with the MAGIC telescopes". PhD thesis. [Barcelona]: Universitat Autònoma de Barcelona. URL: https://ddd.uab.cat/record/127519.

Lorenz, E. and R. Wagner (2012). "Very-high energy gamma-ray astronomy. A 23-year success story in high-energy astroparticle physics". In: European Physical Journal H 37.3 (8), pp. 459–513. DOI: 10.1140/epjh/e2012-30016-x. arXiv: 1207.6003 [physics.hist-ph].

Lorenz, Eckart (2004). "Status of the 17 m MAGIC telescope". In: New Astronomy Reviews 48.5. 2nd VERITAS Symposium on the Astrophysics of Extragalactic Sources, pp. 339–344. ISSN: 1387-6473. DOI: https://doi.org/10.1016/j.newar.2003.12.059. URL: https://www.sciencedirect.com/science/article/pii/S1387647303003579.

Lorimer, Duncan R. (2005). "Binary and Millisecond Pulsars". In: Living Reviews in Relativity 8.1, 7 (11), p. 7. DOI: 10.12942/lrr-2005-7. arXiv: astro-ph/0511258 [astro-ph].

Lyutikov, Maxim (2013). "Inverse Compton model of pulsar high-energy emission". In: MNRAS 431.3 (5), pp. 2580–2589. DOI: 10.1093/mnras/stt351. arXiv: 1208.5329 [astro-ph.HE].

Lyutikov, Maxim, Nepomuk Otte, and Andrew McCann (2012). "The Very High Energy Emission from Pulsars: A Case for Inverse Compton Scattering". In: ApJ 754.1, 33 (7), p. 33. DOI: 10.1088/0004-637X/754/1/33. arXiv: 1108.3824 [astro-ph.HE].

M. L. Ahnen, and et al. (2017). In: 232.1 (sep), p. 9. DOI: 10.3847/1538-4365/aa8404. URL: https://doi.org/10.3847/1538-4365/aa8404.

MAGIC Collaboration et al. (2017). "Constraining Lorentz Invariance Violation Using the Crab Pulsar Emission Observed up to TeV Energies by MAGIC". In: ApJS 232.1, 9 (9), p. 9. DOI: 10.3847/1538-4365/aa8404. arXiv: 1709.00346 [astro-ph.HE].

MAGIC Collaboration et al. (2020). "Detection of the Geminga pulsar with MAGIC hints at a power-law tail emission beyond 15 GeV". In: A&A 643, L14 (11), p. L14. DOI: 10.1051/0004-6361/202039131. arXiv: 2011.10412 [astro-ph.HE].

Magueijo, João and Lee Smolin (2002). "Lorentz Invariance with an Invariant Energy Scale". In: Phys. Rev. Lett. 88 (Apr), p. 190403. DOI: 10.1103/PhysRevLett.88.190403. URL: https://link.aps.org/doi/10.1103/PhysRevLett.88.190403.

Manchester, R. N. et al. (2005). "The Australia Telescope National Facility Pulsar Catalogue". In: AJ 129.4 (4), pp. 1993–2006. DOI: 10.1086/428488. arXiv: astro-ph/0412641 [astro-ph].

Martıénez-Huerta, Humberto, Rodrigo Guedes Lang, and Vitor de Souza (2020). "Lorentz Invariance Violation Tests in Astroparticle Physics". In: Symmetry 12.8 (7), p. 1232. DOI: 10.3390/sym12081232.

Martıénez, Manel and Manel Errando (2009). "A new approach to study energy-dependent arrival delays on photons from astrophysical sources". In: Astroparticle Physics 31.3 (4), pp. 226–232. DOI: 10.1016/j.astropartphys.2009.01.005. arXiv: 0803.2120 [astro-ph].

Matt, Sean and Ralph E. Pudritz (2005). "Accretion-powered Stellar Winds as a Solution to the Stellar Angular Momentum Problem". In: ApJ 632.2 (10), pp. L135–L138. DOI: 10.1086/498066. arXiv: astro-ph/0510060 [astro-ph].

Michel, F. Curtis (1973). "Rotating Magnetospheres: an Exact 3-D Solution". In: ApJ 180 (3), p. L133. DOI: 10.1086/181169.

Mignani, R. P. et al. (Feb. 2017). "Evidence for vacuum birefringence from the first optical-polarimetry measurement of the isolated neutron star RX J1856.5-3754". In: MNRAS 465.1, pp. 492–500. DOI: 10.1093/mnras/stw2798. arXiv: 1610.08323 [astro-ph.HE].

Miller, M. C. et al. (2019). "PSR J0030+0451 Mass and Radius from NICER Data and Implications for the Properties of Neutron Star Matter". In: ApJ 887.1, L24 (12), p. L24. DOI: 10.3847/2041-8213/ab50c5. arXiv: 1912.05705 [astro-ph.HE].

Millikan, R. A. and G. H. Cameron (1928). "New Results on Cosmic Rays". In: Nature 121.3036 (1), pp. 19–26. DOI: 10.1038/121019a0.

Mirabel, I. F. (2012). "Gamma-Ray Binaries Revealed". In: Science 335.6065 (1), p. 175. DOI: 10.1126/science.1215895. arXiv: 1201.3317 [astro-ph.HE].

Mochol, I. and J. Petri (2015). "Very high energy emission as a probe of relativistic magnetic reconnection in pulsar winds." In: MNRAS 449 (4), pp. L51–L55. DOI: 10.1093/mnrasl/slv018. arXiv: 1501.07123 [astro-ph.HE].

Murphy, S. A. and A. W. Van Der Vaart (2000). "On Profile Likelihood". In: Journal of the American Statistical Association 95.450, pp. 449–465. DOI: 10.1080/01621459.2000.10474219. eprint: https://www.tandfonline.com/doi/pdf/10.1080/01621459.2000.10474219. URL: https://www.tandfonline.com/doi/abs/10.1080/01621459.2000.10474219.

Muslimov, Alex G. and Alice K. Harding (2004a). "High-Altitude Particle Acceleration and Radiation in Pulsar Slot Gaps". In: ApJ 606.2 (5), pp. 1143–1153. DOI: 10.1086/383079. arXiv: astro-ph/0402462 [astro-ph].

— (2004b). "Particle Acceleration in Pair-starved Pulsars". In: ApJ 617.1 (12), pp. 471–479. DOI: 10.1086/425227. arXiv: astro-ph/0408377 [astro-ph].

Navarro, Jose et al. (1995). "A Very Luminous Binary Millisecond Pulsar". In: ApJ 455 (12), p. L55. DOI: 10.1086/309816.

Oppenheimer, J. R. and G. M. Volkoff (1939). "On Massive Neutron Cores". In: Physical Review 55.4 (2), pp. 374–381. DOI: 10.1103/PhysRev.55.374.

Otero-Santos, J. et al. (2020). "Quasi-periodic behaviour in the optical and γ-ray light curves of blazars 3C 66A and B2 1633+38". In: MNRAS 492.4 (3), pp. 5524–5539. DOI: 10.1093/mnras/staa134. arXiv: 2001.06014 [astro-ph.HE].

Oya, Igor (2010). "Observations of Active Galactic Nuclei with the MAGIC Telescope." PhD thesis. [Madrid]: Universidad Complutense de Madrid.

Özel, Feryal and Paulo Freire (2016). "Masses, Radii, and the Equation of State of Neutron Stars". In: ARA&A 54 (9), pp. 401–440. DOI: 10.1146/annurev-astro-081915-023322. arXiv: 1603.02698 [astro-ph.HE].

Özel, Feryal et al. (2010). "The Massive Pulsar PSR J1614-2230: Linking Quantum Chromodynamics, Gamma-ray Bursts, and Gravitational Wave Astronomy". In: ApJ 724.2 (12), pp. L199–L202. DOI: 10.1088/2041-8205/724/2/L199. arXiv: 1010.5790 [astro-ph.HE].

Pacini, F. (1968). "Rotating Neutron Stars, Pulsars and Supernova Remnants". In: Nature 219.5150 (7), pp. 145–146. DOI: 10.1038/219145a0.

Patruno, Alessandro (2021). Millisecond Pulsar Catalogue. URL: https://apatruno.wordpress.com/about/millisecond-pulsar-catalogue/ (visited on 09/22/2021).

Pétri, Jérôme (2012). "High-energy emission from the pulsar striped wind: a synchrotron model for gamma-ray pulsars". In: MNRAS 424.3 (8), pp. 2023–2027. DOI: 10.1111/j.1365-2966.2012.21350.x. arXiv: 1205.5101 [astro-ph.HE].

Philippov, Alexander A. and Anatoly Spitkovsky (2014). "Ab Initio Pulsar Magnetosphere: Three-dimensional Particle-in-cell Simulations of Axisymmetric Pulsars". In: ApJ 785.2, L33 (4), p. L33. DOI: 10.1088/2041-8205/785/2/L33. arXiv: 1312.4970 [astro-ph.HE].

Piironen, P. and E. W. Eloranta (1994). "Demonstration of a high-spectral-resolution lidar based on an iodine absorption filter". In: Opt. Lett. 19.3 (Feb), pp. 234–236.

DOI: 10.1364/OL.19.000234.
URL: http://ol.osa.org/abstract.cfm?URI=ol-19-3-234.

Pletsch, H. J. et al. (2012). "Binary Millisecond Pulsar Discovery via Gamma-Ray Pulsations". In: Science 338.6112 (12), p. 1314. DOI: 10.1126/science.1229054. arXiv: 1211.1385 [astro-ph.HE].

Qiao, G. J. et al. (2004). "The Inner Annular Gap for Pulsar Radiation: γ-Ray and Radio Emission". In: ApJ 606.1 (5), pp. L49–L52. DOI: 10.1086/421048. arXiv: astro-ph/0403398 [astro-ph].

Qiao, Guo-Jun et al. (2007). "An Annular Gap Acceleration Model for γ-ray Emission of Pulsars". In: Chinese J. Astron. Astrophys. 7 (8), pp. 496–502. DOI: 10.1088/1009-9271/7/4/04. arXiv: 0704.3801 [astro-ph].

Radhakrishnan, V. and G. Srinivasan (1982). "On the origin of the recently discovered ultra-rapid pulsar". In: Current Science 51 (12), pp. 1096–1099.

Riley, T. E. et al. (2019). "A NICER View of PSR J0030+0451: Millisecond Pulsar Parameter Estimation". In: ApJ 887.1, L21 (12), p. L21. DOI: 10.3847/2041-8213/ab481c. arXiv: 1912.05702 [astro-ph.HE].

Rolke, Wolfgang A. and Angel M. López (2001). "Confidence intervals and upper bounds for small signals in the presence of background noise". In: Nuclear Instruments and Methods in Physics Research A 458.3 (2), pp. 745–758. DOI: 10.1016/S0168-9002(00)00935-9. arXiv: hep-ph/0005187 [hep-ph].

Rovelli, Carlo (2004). Quantum Gravity.

Ruderman, M. A. and P. G. Sutherland (1975). "Theory of pulsars: polar gaps, sparks, and coherent microwave radiation." In: ApJ 196 (2), pp. 51–72. DOI: 10.1086/153393.

Saz Parkinson, P. et al. (2017). "On the highest energy emission from millisecond pulsars". In: Proceedings of the 7th International Fermi Symposium, p. 8. arXiv: 1712.06808 [astro-ph.HE].

Schutte, Willem D. and Jan W. H. Swanepoel (2016). "SOPIE: an R package for the non-parametric estimation of the off-pulse interval of a pulsar light curve". In: MNRAS 461.1 (9), pp. 627–640. DOI: 10.1093/mnras/stw1335.

Schwarzschild, K. (1916). "On the Gravitational Field of a Mass Point According to Einstein's Theory". In: Abh. Konigl. Preuss. Akad. Wissenschaften Jahre 1906,92, Berlin,1907 1916 (1), pp. 189–196.

Sitarek, Julian et al. (2013). "Analysis techniques and performance of the Domino Ring Sampler version 4 based readout for the MAGIC telescopes". In: Nuclear Instruments and Methods in Physics Research A 723 (9), pp. 109–120. DOI: 10.1016/j.nima.2013.05.014. arXiv: 1305.1007 [astro-ph.IM].

Srinivasan, G. (2010). "Recycled pulsars". In: New A Rev. 54.3-6 (3), pp. 93–100. DOI: 10.1016/j.newar.2010.09.026.

Staelin, David H. and Edward C. Reifenstein (1968). "Pulsating Radio Sources near the Crab Nebula". In: Science 162.3861, pp. 1481–1483. ISSN: 0036-8075. DOI: 10.1126/science.162.3861.1481.

eprint: https://science.sciencemag.org/content/162/3861/1481.full.pdf. URL: https://science.sciencemag.org/content/162/3861/1481.

Tang, Anisia P. S. et al. (2008). "A Revisit of the Phase-resolved X-Ray and Gamma-Ray Spectra of the Crab Pulsar". In: ApJ 676.1 (3), pp. 562–572. DOI: 10.1086/527029. arXiv: 0711.2719 [astro-ph].

Thompson, D. J. et al. (1974). "SAS-2 Observations of the High-Energy Gamma Radiation from the VELA Region". In: ApJ 190 (6), p. L51. DOI: 10.1086/181502.

Thompson, D. J. et al. (1977). "Final SAS-2 gamma-ray results on sources in the galactic anticenter region." In: ApJ 213 (4), pp. 252–262. DOI: 10.1086/155152.

Torres-Zafra, Juanita et al. (2018). "Redshift determination of the BL Lac object 3C 66A by the detection of its host galaxy cluster at z = 0.340". In: MNRAS 474.3 (3), pp. 3162–3172. DOI: 10.1093/mnras/stx2561. arXiv: 1710.04309 [astro-ph.GA].

Trimble, Virginia (1968). "Motions and Structure of the Filamentary Envelope of the Crab Nebula". In: AJ 73 (9), p. 535. DOI: 10.1086/110658.

Vasileiou, V. et al. (2013). "Constraints on Lorentz invariance violation from Fermi-Large Area Telescope observations of gamma-ray bursts". In: Phys. Rev. D 87 (Jun), p. 122001. DOI: 10.1103/PhysRevD.87.122001. URL: https://link.aps.org/doi/10.1103/PhysRevD.87.122001.

VERITAS Collaboration et al. (2011). "Detection of Pulsed Gamma Rays Above 100 GeV from the Crab Pulsar". In: Science 334.6052 (10), p. 69. DOI: 10.1126/science.1208192. arXiv: 1108.3797 [astro-ph.HE].

Watts, A. et al. (2015). "Probing the neutron star interior and the Equation of State of cold dense matter with the SKA". In: Advancing Astrophysics with the Square Kilometre Array (AASKA14), p. 43. arXiv: 1501.00042 [astro-ph.SR].

Watts, Anna L. (2019). "Constraining the neutron star equation of state using pulse profile modeling". In: Xiamen-CUSTIPEN Workshop. Vol. 2127. American Institute of Physics Conference Series, p. 020008. DOI: 10.1063/1.5117798. arXiv: 1904.07012 [astro-ph.HE].

Weber, F., R. Negreiros, and P. Rosenfield (2007). "Neutron Star Interiors and the Equation of State of Superdense Matter". In: arXiv: Astrophysics 892, pp. 515–517.

Wijnands, Rudy and Michiel van der Klis (1998). "A millisecond pulsar in an X-ray binary system". In: Nature 394.6691 (7), pp. 344–346. DOI: 10.1038/28557.

Wróbel, M.S. (2016). "Non-invasive blood glucose monitoring with Raman spectroscopy: prospects for device miniaturization". In: IOP Conference Series: Materials Science and Engineering 104 (jan), p. 012036. DOI: 10.1088/1757-899x/104/1/012036. URL: https://doi.org/10.1088/1757-899x/104/1/012036.

Zanin, Roberta et al. (2013). "MARS, The MAGIC Analysis and Reconstruction Software". In: International Cosmic Ray Conference. Vol. 33. International Cosmic Ray Conference, p. 2937.

Ziólkowski, J. (1997). "Recycled pulsars". In: Ital. Phys. Soc. Conf. Ser. 57: Frontier Objects in Astrophysics and Particle Physics. Ed. by F. Giovannelli and G. Mannocchi, p. 301.